

A micromorphically regularized Cam-clay model for capturing size-dependent anisotropy of geomaterials

Eric C. Bryant · WaiChing Sun

Received: May 6, 2019/ Accepted: date

Abstract We introduce a regularized anisotropic modified Cam-clay (MCC) model which captures the size-dependent anisotropic elastoplastic responses for clay, mudstone, shales, and sedimentary rock. By homogenizing the multiscale anisotropic effects induced by clay particle aggregate, clusters, peds, micro-fabric, and mineral contact across length scales, we introduce two distinctive anisotropic mechanisms for the MCC model at the material point and mesoscale levels. We first employ a mapping that links the anisotropic stress state to a fictitious isotropic principal stress-space to introduce anisotropy at the material point scale. Then, the mesoscale anisotropy is introduced via an anisotropic regularization mechanism. This anisotropic regularization mechanism is triggered by introducing gradient-dependence of the internal variables through a penalty method such that the resultant gradient-enhanced plastic flow may exhibit anisotropic responses non-coaxial to the stress gradient of the yield function. The influence of the size-dependent anisotropy on the formation of the shear band and the macroscopic responses of the effective media are analyzed in 2D and 3D numerical examples.

Keywords gradient critical state plasticity, micromorphic regularization, size-dependent anisotropy

1 Introduction

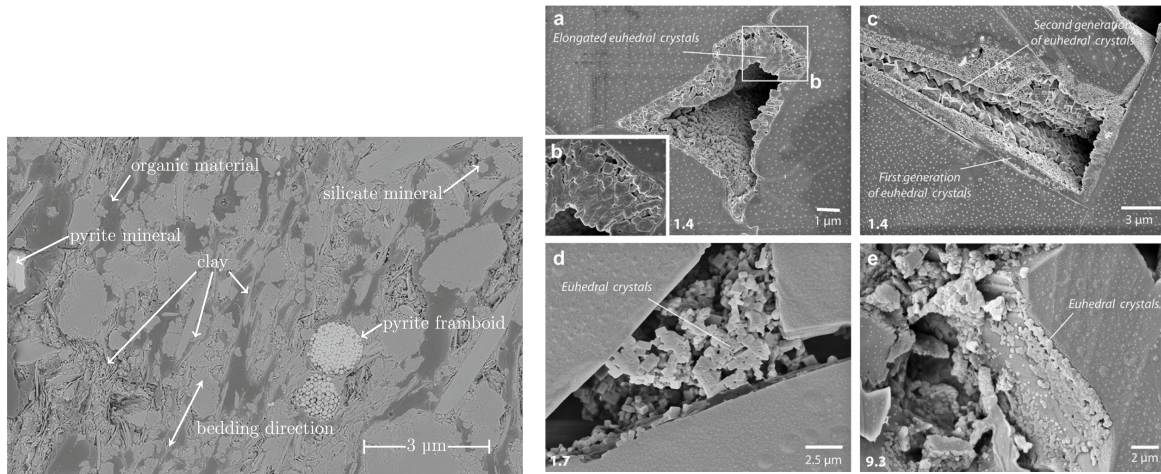
Clay, mudstone and shales are materials that exhibit different anisotropic response across different length scales. This scale-dependent anisotropy originates from the fabric and microstructures of clay platelet and other fragments of minerals such as quartz and calcite. At the nanoscale, clay particles may aggregate together in sub-microscopic fabric units, which is often referred as domains. These domains then form clusters, which in return form peds that are large enough to be visible. Together with other features, such as joints and fissures, the peds then form a microfabric system that is inherently anisotropic. As shown in Fig. 1 (cf. Desbois et al. [2012] and Bennett et al. [2015b]), the anisotropy of clay and crystalline rock is often not just manifested by a single morphological feature (e.g. bedding orientation, inclusion of different materials). Instead, the anisotropy of the material response is the consequence of multiple microstructural mechanisms that may differ for effective media of different sampling sizes [Collins and McGown, 1974].

Furthermore, size effects are also related to the statistical distribution in the severity of flaws. For instance, Weibull's theory predicts that the stress that triggered fracture is proportional to the $V^{1/\beta}$ where V is the volume of the specimen and β is a material constant [Weibull, 1951]. On the other hand, experimental observations of size dependence in geological materials have been reported in uniaxial compression and in Brazilian tests [Na et al., 2017, Paterson and Wong, 2005]. In general, these tests often lead to the conclusion that shear strength consistently decreases with increasing dimensions. However, it is important to note that the size-dependent effect is often more profound when a sharp stress gradient presents due to

Corresponding author: WaiChing Sun

Assistant Professor, Department of Civil Engineering and Engineering Mechanics, Columbia University, 614 SW Mudd, Mail Code: 4709, New York, NY 10027 Tel.: 212-854-3143, Fax: 212-854-6267, E-mail: wsun@columbia.edu

37 the loading conditions (e.g., punch and indentation tests). This size dependence might also be suppressed
 38 when the confining pressure increases [Habib et al., 1966], but is of great importance in the brittle regime.



(a) Shale with organic and clay mixture identified as the matrix, characterized however by inorganic and dense organic inclusion, with matrix identification and from Bennett et al. [2015b].

(b) Rock salt heterogeneity with spatial scale decreasing from (a) to (d), showing distribution of gas and brine inclusions at the course scale, compared to brine contained within pores at the fine scale, from Desbois et al. [2012]

Fig. 1: Rock material heterogeneity at the micrometer scale, showing two different materials of significant engineering interest, both characterized by size-dependence of the anisotropy.

39 The major contribution of this work is the introduction of non-coaxial micromorphic regularization for
 40 the anisotropic MCC model. This treatment enables us to represent the distinct anisotropic characteristics
 41 at the particle and aggregate scales, via two mathematical treatments – (1) by introducing mapping tensor
 42 at the constitutive laws following Semnani et al. [2016] and (2) by introducing anisotropic micromorphic
 43 regularization via a penalty or relaxation functional following Forest [2016], Forest et al. [2018], Miehe et al.
 44 [2016]. The introduction of the map greatly simplifies the implementation of anisotropic constitutive laws,
 45 as demonstrated in previous works such as Semnani et al. [2016] and Bennett et al. [accepted]. Meanwhile,
 46 we introduce the anisotropic regularization by a variational model in which an Euler-Lagrange equation
 47 leads to the incremental update of the local constitutive law and two sets of Helmholtz equations that regu-
 48 larize the plastic flow and circumvent pathological mesh dependence. Rather than directly introducing
 49 gradient term to the plastic flow, we introduce coupling energy functionals that penalize the difference
 50 between the local internal variables and the global projected internal variables updated by the Helmholtz
 51 equations. This treatment enables us to bypass the identification of the plastic zone and the projection of
 52 the local internal variables typically required for gradient plasticity models [Stankiewicz and Pamin, 2006].
 53 By leveraging the non-coaxiality of the local transversely isotropic plane and the diffusivity tensor in the
 54 Helmholtz equations, the new model is able to exhibit plastic flow of different direction than the stress
 55 gradient of the isotropically-regularized yield function, without introducing any plastic potential func-
 56 tion, differently than the yield function or direction changes commonly employed in generalized plasticity
 57 models [Zienkiewicz et al., 1999]. To the best of our knowledge, this work is the first micromorphically
 58 regularized Cam-clay model, and is designed to capture the size-dependent anisotropy in geological ma-
 59 terials.

60 As pointed out in previous work such as Scovazzi et al. [2016], Sun [2015], Sun et al. [2013, 2014], Wang
 61 and Sun [2016, 2018], isochoric plastic flow occurring at the critical state may cause significant numerical
 62 challenges due to volumetric locking and potential low or zero energy modes sometimes attributed to the
 63 failure of geomaterials [Krischok and Linder, 2016, Sun, 2013, Sun and Andrade, 2011, Wang and Sun,
 64 2016]. While the micromorphic regularization is already known to be an effective localization limiter, its

effect on relaxing the volumetric locking has not yet been examined in detail. Our numerical examples have provided observations and numerical evidence to fill this knowledge gap. Finally, our numerical examples also indicate that the multiscale anisotropic model is capable of capturing the key morphological characteristic of the deformation band in anisotropic materials.

The organization of the rest of the paper is as follows. We first introduce the key elements of the anisotropic MCC model, including the usage of a mapping tensor for the local constitutive law and the gradient-based diffusive penalty stored work functional that provides a non-coaxial regularization for the post-bifurcation responses. Following this, the details of the implementation of the return mapping algorithm are discussed. Numerical examples are given and a brief summary of key results are presented in the conclusion.

As for notations and symbols, bold-faced letters denote tensors; the symbol \cdot denotes a single contraction of adjacent indices of two tensors (e.g., $\mathbf{a} \cdot \mathbf{b} = a_i b_i$ or $\mathbf{c} \cdot \mathbf{d} = c_{ij} d_{jk}$); the symbol $\cdot\cdot$ denotes a double contraction of adjacent indices of tensor of rank two or higher (e.g., $\mathbf{C}^e : \boldsymbol{\epsilon}^e = C_{ijkl}^e \epsilon_{kl}^e$); the symbol \otimes denotes a juxtaposition of two vectors (e.g., $\mathbf{a} \otimes \mathbf{b} = a_i b_j$) or two symmetric second order tensors (e.g., $(\boldsymbol{\alpha} \otimes \boldsymbol{\beta})_{ijkl} = \alpha_{ij} \beta_{kl}$). Moreover, $(\boldsymbol{\alpha} \oplus \boldsymbol{\beta})_{ijkl} = \alpha_{jl} \beta_{ik}$ and $(\boldsymbol{\alpha} \ominus \boldsymbol{\beta})_{ijkl} = \alpha_{il} \beta_{jk}$. We also define identity tensors $(\mathbf{1})_{ij} = \delta_{ij}$ and $(\mathbf{I})_{ijkl} = (\delta_{ik} \delta_{jl} + \delta_{il} \delta_{kj})/2$, where δ_{ij} is the Kronecker delta.

Nomenclature

Field variables

\mathbf{u}	= displacement field
$\tilde{\boldsymbol{\epsilon}}_v^p$	= projected volumetric plastic strain field
$\tilde{\boldsymbol{\lambda}}$	= projected equivalent plastic strain field

Local and internal variables

\mathbf{n}	= plastic strain direction
p	= pressure
q	= deviatoric stress invariant
$\boldsymbol{\epsilon}$	= strain
$\boldsymbol{\epsilon}^e$	= elastic strain
$\boldsymbol{\epsilon}^p$	= plastic strain
$\boldsymbol{\epsilon}_v^p$	= volumetric plastic strain
λ	= equivalent plastic strain, the time integration of the incremental plastic multiplier
$\boldsymbol{\sigma}$	= stress
σ_p	= pressure-like plastic internal variable
σ_q	= deviatoric stress invariant-like plastic internal variable

Elastic parameters

\mathbf{C}^e	= elastic tangent described by elastic material parameters E , E_l , μ_l , ν , ν_l , and the microstructural direction via the Walpole algebra
E	= Young's modulus in the isotropic plane described by χ
E_1	= symmetric element of the Walpole algebra
E_2	= symmetric element of the Walpole algebra

E_3	= element of the Walpole algebra
E_4	= element of the Walpole algebra
E_l	= Young's modulus in the isotropic plane's normal direction described by $\boldsymbol{\phi}$
F	= symmetric element of the Walpole algebra
G	= symmetric element of the Walpole algebra
\mathbf{l}	= microstructural direction unit vector
$\boldsymbol{\phi}$	= microstructural tensorial out-of-plane direction
$\boldsymbol{\chi}$	= microstructural tensorial in-plane direction
μ_l	= shear modulus characterizing in-plane shear stress due to shear strain in the microstructural direction
ν	= Poisson ratio characterizing transverse in-plane contraction due to tension applied in the perpendicular direction within the plane of isotropy
ν_l	= Poisson ratio characterizing transverse in-plane contraction due to tension applied in the microstructural direction

Plastic parameters

C_c	= compressibility index
C_r	= re-compressibility index
M	= slope of the critical state line
p_c	= preconsolidation pressure
$\mathbf{P}^{p \text{ dev}}$	= deviatoric plastic map, described by coefficients a^{dev} , β^{dev} , γ^{dev} , and the mi-

142	crostructural direction via the symmetric	168	k_λ	= relaxation stiffness for the discrepancy
143	Walpole subalgebra	169		between local and projected equivalent
144	$\mathbb{P}^{\text{P vol}}$	170		plastic strain
145	= volumetric plastic map, described by	171	K_v	= regularization stiffness for the projected
146	coefficients α^{vol} , β^{vol} , γ^{dev} , and the mi-	172		volumetric plastic strain
147	crostructural direction via the symmetric	173	K_λ	= regularization stiffness for the projected
148	Walpole subalgebra	174		equivalent plastic strain
148	α^{dev}	175	ϕ_v	= diffusion tensor coefficient for the pro-
149	= deviatoric plastic map coefficient	176		jected volumetric plastic strain
150	α^{vol}	176		
150	= volumetric plastic map coefficient	177	ϕ_v	= tensorial out-of-plane direction used to
151	β^{dev}	178		construct the diffusivity tensor for the pro-
151	= deviatoric plastic map coefficient	179		jected equivalent plastic strain
152	β^{vol}	180	ϕ_λ	= diffusion tensor coefficient for the pro-
152	= volumetric plastic map coefficient	181		jected equivalent plastic strain
153	γ^{dev}	182	ϕ_λ	= tensorial out-of-plane direction used to
153	= deviatoric plastic map coefficient	183		construct the diffusivity tensor for the pro-
154	γ^{vol}	184		jected equivalent plastic strain
154	= volumetric plastic map coefficient	185	χ_v	= volumetric diffusion tensor coefficient
154	Micromorphic parameters	186	χ_v	= volumetric tensorial in-plane direction,
155	l_v	187		described by volumetric diffusion direc-
156	= length scale for projected volumetric	188		tion
157	plastic strain	189	χ_λ	= diffusion tensor coefficient for the pro-
157	l_v	190		jected equivalent plastic strain
158	= unit vector used to construct the	191	χ_λ	= tensorial in-plane direction used to con-
159	anisotropic diffusivity tensor of the pro-	192		struct the diffusivity tensor for the pro-
160	jected volumetric plastic strain	193		jected equivalent plastic strain
160	l_λ			
161	= length scale for projected equivalent			
162	plastic strain			
162	l_λ			
163	= unit vector used to construct the			
164	anisotropic diffusivity tensor of the pro-			
165	jected equivalent plastic strain			
165	k_v			
166	= penalty stiffness for the discrepancy be-			
167	tween local and projected volumetric plas-			
167	tic strain			

194 2 Micromorphic anisotropic MCC model

195 In this section, we introduce the formulation of the micromorphic anisotropic MCC model capturing the
 196 size-dependent anisotropy of the plastic response. For simplicity, the anisotropically elastic response of the
 197 material is assumed to be linear. Then, we incorporate a non-coaxial anisotropic micromorphic regular-
 198 ization into the anisotropic MCC framework previously introduced in [Crook et al. \[2002\]](#) and codified in
 199 [Semnani et al. \[2016\]](#). While both the anisotropic mapping and the anisotropic regularization both lead to
 200 transversely isotropic responses, they influence the plastic deformation differently. Local anisotropy intro-
 201 duced through the map may provides the response. of a homogenized effective medium. In contrast, the
 202 anisotropic regularization provides a mechanism that introduces size-dependent anisotropy, wherein the
 203 anisotropic response is sensitive to the physical length scale of the material for a given orientation. Since
 204 these two anisotropic mechanisms are not necessarily co-axial, incorporating both can provide more flexi-
 205 bility to capture of the material responses of the microstructure composed of fabric, platelet, and minerals
 206 that span multiple length scales. The following assumptions are made throughout this paper.

- 207 – The deformation remains infinitesimal such that the infinitesimal strain measure applies, i.e. $\epsilon =$
 208 $(\nabla \mathbf{u} + \nabla \mathbf{u}^T)/2 = \nabla_s \mathbf{u}$, where \mathbf{u} is the displacement field.
- 209 – The deformation process occurs while maintaining the isothermal condition such that the heat transfer
 210 can be neglected.
- 211 – The inertial force is negligible and hence the material is under a quasi-static condition.

In the geometrically linear regime, the additive strain decomposition of the infinitesimal elastic and plastic strains is valid, i.e.

$$\epsilon = \epsilon^e + \epsilon^p, \quad (1)$$

212 where superscripting e and p designates elastic and plastic parts of the strain, respectively. The stored work
213 is partitioned into the elastic strain energy and the stored plastic work, i.e.

$$W(\boldsymbol{\epsilon}^e, \boldsymbol{\alpha}, \tilde{\boldsymbol{\alpha}}) = W^e(\boldsymbol{\epsilon}^e) + W^P(\boldsymbol{\alpha}, \tilde{\boldsymbol{\alpha}}), \quad (2)$$

where $\boldsymbol{\alpha}$ is a collection of strain-like internal variables computed from the plastic strain $\boldsymbol{\epsilon}^P$. In contrast, $\tilde{\boldsymbol{\alpha}}$ is a collection of field variables related to the internal variables by relaxation functionals in the stored plastic work W^P [Aldakheel and Miehe, 2017, Forest, 2009]. The total stored plastic work W^P is partitioned as

$$W^P(\boldsymbol{\alpha}, \tilde{\boldsymbol{\alpha}}) = W_{\boldsymbol{\alpha}}^P(\boldsymbol{\alpha}) + W_{\tilde{\boldsymbol{\alpha}}}^P(\boldsymbol{\alpha}, \tilde{\boldsymbol{\alpha}}), \quad (3)$$

214 where $\boldsymbol{\alpha} = \{\lambda, \boldsymbol{\epsilon}_v^P\}$ is the set of history-dependent variables subjected to gradient regularization via a re-
215 laxation energy functional that penalizes the discrepancy of $\boldsymbol{\alpha}$ and the set of corresponding field variables
216 constrained by the Helmholtz equation, i.e. $\tilde{\boldsymbol{\alpha}} = \{\tilde{\lambda}, \tilde{\boldsymbol{\epsilon}}_v^P\}$. In this work, we introduce regularization both on
217 the plastic multiplier λ and on the volumetric plastic strain $\boldsymbol{\epsilon}_v^P$. This strategy is more complex, more costly
218 and requires more elaborated calibration effects to identify material parameters than the alternative where
219 only one internal variable is regularized in Aldakheel and Miehe [2017], Forest [2009]. However, introduc-
220 ing the gradient regularization for both the plastic multiplier λ and the volumetric plastic strain $\boldsymbol{\epsilon}_v^P$ also
221 provides some benefits in capturing the critical state under which the plastic strain becomes isochoric [Ab-
222 boud and Scovazzi, 2018, Schofield and Wroth, 1968, Sun et al., 2013, Wood, 1990]. In particular, the second
223 Helmholtz equation for the regularized field variable $\tilde{\boldsymbol{\epsilon}}_v^P$ may penalize the sharp gradient of the local vol-
224 umetric plastic strain by introducing a cost to generate such a sharp gradient. In principle, this technique
225 can also be applied in an element-by-element manner through introducing an assumed strain formulation
226 (Krischok and Linder [2016]), reduced integration with hourglass control (e.g. Reese et al. [2017]) or non-
227 local averaging on a patch [Cheng et al., 2016]. Preliminary studies presented in our numerical examples
228 indicates that introducing the Helmholtz equation for the local volumetric plastic strain is sufficient to cir-
229 cumvent the volumetric locking with a more intuitive physical underpinning. Further analysis is certainly
230 required to determine the optimal approach to capture the isochoric plastic flow at the critical state, but
231 such an analysis is out of the scope of current study.

232 Note that this indirect approach enables the field variables within $\tilde{\boldsymbol{\alpha}}$ to be defined not just inside the
233 plastic zone but on the entire body \mathcal{B} with boundary $\partial\mathcal{B}$ as:

$$\tilde{\lambda} : \mathcal{B} \rightarrow \mathbb{R}^+ \cup \{0\} \mid \hat{\boldsymbol{n}} \cdot \boldsymbol{\omega}_\lambda \cdot \nabla \tilde{\lambda} = 0 \text{ on } \partial\mathcal{B}, \quad \tilde{\boldsymbol{\epsilon}}_v^P : \mathcal{B} \rightarrow \mathbb{R} \mid \hat{\boldsymbol{n}} \cdot \boldsymbol{\omega}_v \cdot \nabla \tilde{\boldsymbol{\epsilon}}_v^P = 0 \text{ on } \partial\mathcal{B}, \quad (4)$$

234 where $\hat{\boldsymbol{n}}$ is the boundary unit outward normal, and $\boldsymbol{\omega}_\lambda$ and $\boldsymbol{\omega}_v$ are second-order micromorphic diffusivity
235 tensors. These tensors and the specific form of $W_{\tilde{\boldsymbol{\alpha}}}^P(\boldsymbol{\alpha}, \tilde{\boldsymbol{\alpha}})$ are discussed in Section 2.3.

236 2.1 Anisotropic elasticity

237 We employ a linear elasticity model such that the strain energy and elastic strain are related via

$$W^e = \frac{1}{2} \boldsymbol{\epsilon}^e : \boldsymbol{C}^e : \boldsymbol{\epsilon}^e, \quad (5)$$

238 where \boldsymbol{C}^e is an super-symmetric fourth-order tensor expressing transverse isotropy of the elastic material
239 response (for terminology cf. Itskov [2000], and for discussion of related Kelvin-notated matrix equivalents
240 exhibiting symmetry such at the solid elastic tangent, see Appendix A).

241 As such by Eq. (5), we discard in this work: nonlinearity of the material's elastic volumetric response,
242 such that the pressure is semilogarithmic in the trace of the elastic strain during elastic unloading or re-
243 bounding; and, any potential coupling of the effective shear moduli to changes in the elastic bulk modu-
244 lus with confining stress. In fact, elastic nonlinearity has previously been written in a strain energy func-
245 tional amenable to a variational treatment, e.g. see Eq. (3.4-6) in Borja and Tamagnini [1998], given that our
246 model's local minimization is already over the elastic strain (per later Section 2.5).

247 To introduce anisotropy of the elastic response corresponding to the orientation of the isotropic plane's
248 normal, this elastic stiffness tensor \boldsymbol{C}^e is expressed as a function of a second-order microstructural tensor,
249 a dyadic tensor denoted as $\boldsymbol{\phi} = \boldsymbol{l} \otimes \boldsymbol{l}$, where the microstructural direction \boldsymbol{l} is an unit vector normal to the

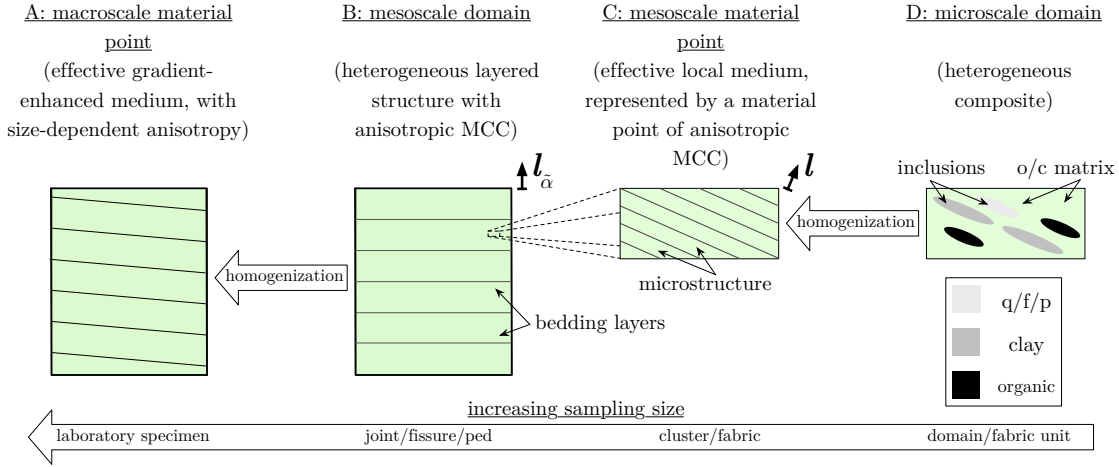


Fig. 2: Schematic of mesoscale and microscale-homogenized material effective media, where l is the microstructural direction whereas $l_{\tilde{\alpha}}$ is the direction characterizing the anisotropic micromorphic regularization of a plastic internal variable α , via the projected internal variable $\tilde{\alpha}$, governed by energy functionals as detailed in Section 2.3, with inhomogeneous microscale identification and constituent categorization after Bennett et al. [2015b]; q/f/p means inorganic quartz, feldspar, or pyrite, and o/c matrix indicates organic and clay matrix.

250 plane of isotropy, for $l \cdot l = 1$. For instance, l would be approximately vertical for many in-situ shale rock
 251 layers. The transversely isotropic elastic stiffness tensor is then represented via direction l (cf. Walpole
 252 [1984]):

$$C^e = c_1 E_1 + c_2 E_2 + c_3 (E_3 + E_4) + c_5 F + c_6 G, \quad (6)$$

253 where c_1 through c_6 are elastic moduli and E_1 through G are fourth-order tensors, related to the elastic
 254 input parameters, see Appendix B.

255 In this work, we introduce a gradient-dependent constitutive law for geomaterials (e.g. clay, mudstone,
 256 shales and salt) that may exhibit size-dependent anisotropy due to the complex microstructures. As shown
 257 in the example illustrated in Fig. 2, a macroscopic representative elementary volume (e.g. A in Fig. 2)
 258 may be formed by mesoscale layers that introduce anisotropy at the macroscopic scale (e.g. the homogenization
 259 from B to A in Fig. 2). However, the composite materials that form each layer may also contain microscopic
 260 fabrics or domain units (e.g. D in Fig. 2) that introduce an mesoscale anisotropy originating from the mi-
 261 croscale composite (e.g. the homogenization from D to C in Fig. 2) but distinctive from those anisotropic
 262 effects introduced by the orientation of the homogenized layers (e.g. B in Fig. 2). As such, if we introduce
 263 a transversely isotropic effective medium at the scale comparable to the mesoscale layers, then the Euler
 264 angles between the effective principal directions corresponding to the homogenized principal strain and
 265 stress tensors of the effective medium may vary when different sizes of the representative elementary vol-
 266 ume are subjected to homogenization. This effect is referred as size-dependent anisotropy throughout this
 267 paper. To capture this size-dependent anisotropy, we therefore introduce an anisotropic regularization for a
 268 transversely isotropic local constitutive law and use the mismatches among the isotropy plane of the local
 269 constitutive law and the principal directions of the diffusivity tensors of the gradient terms to replicate the
 270 size-dependence of anisotropy across length scales.

271 2.2 Anisotropic local plasticity

272 This section describes the local contribution W_{α}^P of the total stored plastic work W^P , which is partitioned
 273 as $W^P(\alpha, \tilde{\alpha}) = W_{\alpha}^P(\alpha) + W_{\tilde{\alpha}}^P(\alpha, \tilde{\alpha})$. In particular, we will review the relation between the hardening law
 274 and the stored plastic work (cf. Section 2.2.1) and the flow rules introducing via the mapping technique (cf.
 275 Section 2.2.2).

276 2.2.1 Hardening law

277 The stored work of hardening W_c^P in the purely local stored plastic work W_α^P is computed using an exponential constitutive relation. This admits model parameters (e.g. C_d) resembling the expression of the
 278 classical hardening law for the isotropic MCC counterpart (cf. [Borja \[2013\]](#), [Roscoe and Schofield \[1963\]](#),
 279 [Schofield and Wroth \[1968\]](#)),
 280

$$p_c = p_{c0} \exp\left(\frac{\epsilon_v^P - \epsilon_v^P}{C_d}\right), \quad \dot{\epsilon}_v^P = \mathbf{b}_v : \dot{\epsilon}^P, \quad (7)$$

281 where $p_{c0} < 0$ is the reference pressure, and $C_d > 0$ is a material parameter related to the difference be-
 282 tween the plastic and elastic compressibility of the materials. In the special case where (1) the bulk modulus
 283 of the material is $K = -p/C_r$ (which is not the case described in Section 2.1) and (2) the gradient regulariza-
 284 tion effect is vanished, then the bilogarithmic compressibility law $C_d = C_c - C_r$ introduced in [Hashiguchi
 285 and Ueno \[1977\]](#) and [Butterfield \[1979\]](#) is recovered over a finite load increment. In other words, the param-
 286 eter C_d can be obtained from an one-dimensional compression (oedometer) test. However, special caution
 287 must be paid to ensure that the plastic deformation of the specimen remains *homogeneous* (such that the
 288 Laplacian/diffusion terms of the Helmholtz equations vanish) along the normal compression line and the
 289 hysteresis loops.

Note that in this content, $\dot{\epsilon}_v^P = \mathbf{b}_v : \dot{\epsilon}^P$ is not the increment of the volumetric plastic strain in the physical space but a strain measure in the fictitious space. Symmetric second-order tensor \mathbf{b}_v is conventionally $\mathbf{1}$, such that ϵ_v^P is the volumetric plastic strain. For our small-strain kinematic assumption, this implies to a semilogarithmic relation between $-p_c$ and ϵ_v during plastic deformation, cf. Eqs. (3.14-19) in [Borja and Tamagnini \[1998\]](#). Integrating p_c to find the stored work

$$W_c^P - W_{c0}^P = \int_{\epsilon_v^P}^{\epsilon_v^P} p_c d\epsilon_v^P = p_{c0} C_d \left[1 - \exp\left(\frac{\epsilon_v^P - \epsilon_v^P}{C_d}\right) \right], \quad (8)$$

290 where subscripting 0 indicates the reference state. In our numerical examples, we consider the idealized
 291 case in which the preconsolidation pressure p_{c0} is non-trivial but $\epsilon_v^P = 0$ and p_{c0} as indicated in Ap-
 292 pendix D. For applications in the field scale, a more elaborated calibration is needed to establish the equi-
 293 librium state at the beginning of the simulations, as the residual stress and the body force may lead to a
 294 deformed initial configuration [[Potts et al., 2001](#)].

295 2.2.2 Flow rule in mapped space

296 In our proposed constitutive framework, anisotropy of the responses originates from two sources, the
 297 anisotropy from the local constitutive law and the counterpart from anisotropic micromorphic regulariza-
 298 tion. As to the local plastic anisotropy, we employ an eigen-space mapping strategy. The key idea of this
 299 eigen-space mapping idea is to create a mapping in between the physical space and an fictitious isotropic
 300 space, such that anisotropic constitutive response in the physical space can be obtained by mapping a
 301 isotropic constitutive response obtained from an isotropic plasticity model to the physical space. This strat-
 302 egy has applied as a stress-space mapping in different isotropic yield functions to introduce anisotropy,
 303 such as [Hashagen and de Borst \[2001\]](#) for the Hoffman yield function, [Crook et al. \[2002\]](#) and [Semnani
 304 et al. \[2016\]](#) for the MCC yield function, [Versino and Bennett \[2018\]](#) for the Von Mises yield function and
 305 [Bennett et al. \[accepted\]](#) for the Drucker-Prager yield function.

The upshot of this approach is that one may, in theory, create anisotropic constitutive laws from a template of isotropic constitutive law by introducing a linear and one-to-one mapping between the real configuration of the material and the fictitious isotropic configuration, by either stress-space or, as here, strain-space mapping tensors. The anisotropic plasticity mapping can be represented by a super-symmetric fourth-order tensor. This tensor is also built using \mathbf{I} as, cf. [Semnani et al. \[2016\]](#):

$$\mathbf{P}^P = \beta \mathbf{P}_1^P + (\alpha + \beta - 2\gamma) \mathbf{P}_2^P + 2(\gamma - \beta) \mathbf{P}_3^P, \quad (9)$$

where α , β , and γ are plastic anisotropy input parameters, and \mathbf{P}_1^{P} through \mathbf{P}_3^{P} are super-symmetric fourth-order tensors, see Appendix C. Input material parameters are selected such that \mathbf{P}^{P} is invertible and, on that note, $\mathbf{P}^{\text{P}}(\alpha, \beta, \gamma) = \mathbf{I}$ for $\alpha = \beta = \gamma = 1$. Their plastic map defines the mean pressure and deviatoric stress in the mapped fictitious isotropic stress-space,

$$p^* = \mathbf{a}_p : \boldsymbol{\sigma}, \quad q^* = \sqrt{\frac{1}{2} \boldsymbol{\sigma} : \mathbf{A}_q : \boldsymbol{\sigma}}, \quad (10)$$

306 where

$$\mathbf{a}_p = \frac{1}{3} \mathbf{P}^{\text{P vol}} : \mathbf{1}, \quad \mathbf{A}_q = 3 \mathbf{P}^{\text{P dev}} : \mathbf{P}^{\text{dev}} : \mathbf{P}^{\text{P dev}}, \quad \mathbf{P}^{\text{dev}} = \mathbf{I} - \mathbf{P}^{\text{vol}}, \quad \mathbf{P}^{\text{vol}} = \frac{1}{3} \mathbf{1} \otimes \mathbf{1},$$

307 for distinct mappings $\mathbf{P}^{\text{P dev}}(\alpha^{\text{dev}}, \beta^{\text{dev}}, \gamma^{\text{dev}}) \neq \mathbf{P}^{\text{P vol}}(\alpha^{\text{vol}}, \beta^{\text{vol}}, \gamma^{\text{vol}})$. Superscripting 'dev' and 'vol' re-
308 lates to independent deviatoric and volumetric maps, respectively. Absent superscript *, p and q are com-
309 puted using \mathbf{I} as the plastic mapping tensor. Fourth-order projection tensors \mathbf{P}^{dev} and \mathbf{P}^{vol} are idempotent
310 and orthogonal, cf. [Itskov \[2000\]](#) or Section 2.6 in [Simo \[1998\]](#).

Following the treatment in [Ortiz and Pandolfi \[2004\]](#), we consider the plastic deformation obey the same associative flow rule and that a variational structure exists such that the plastic flow rule is the primitive postulate of the theory, and latterly the elastic domain-describing yield criterion is the derived rule, also cf. [Weinberg et al. \[2006\]](#). While [Ortiz and Pandolfi \[2004\]](#) has demonstrated that such a framework is convenient for extending the isotropic MCC model into the finite deformation regime and enforcing material-frame indifference, our derivation in the subsequent sections indicates that this variational framework also simplify the extension of the MCC to incorporate a gradient-dependent flow rule. For the local anisotropic MCC plasticity, the flow rule is

$$\dot{\boldsymbol{\epsilon}}^{\text{P}} = \dot{\lambda} \mathbf{n} \mid \dot{\lambda} \geq 0, \quad (11)$$

311 where the local equivalent plastic strain's rate $\dot{\lambda}$ is non-negative, \mathbf{n} the second-order tensorial direction of
312 plastic flow is not traceless, and $(\dot{\cdot})$ indicates the time derivative of (\cdot) . If yielding, plastic strain direction
313 \mathbf{n} satisfies the kinematic constraint

$$\mathbf{n} : \mathbf{B}_\lambda : \mathbf{n} = 1, \quad \mathbf{B}_\lambda = \frac{3}{M^2} \mathbf{P}^{\text{P vol} - 1} : \mathbf{P}^{\text{vol}} : \mathbf{P}^{\text{P vol} - 1} + \frac{2}{3} \mathbf{P}^{\text{P dev} - 1} : \mathbf{P}^{\text{dev}} : \mathbf{P}^{\text{P dev} - 1}, \quad (12)$$

314 where $M > 0$ is a dimensionless physical constant, later shown to be the slope of the critical state line,
315 in Section 2.5.1 and 2.5.2. Our convention is that the symmetric fourth-order tensor $\mathbf{A}_{(\cdot)}$ maps stress $\boldsymbol{\sigma}$
316 from the real stress to fictitious isotropic stress-space, whereas $\mathbf{B}_{(\cdot)}$ maps kinematics-related tensorial in-
317 ternal variables, which convention is intended to be in-line with the general quadratic model for plasticity
318 presented in Section 2.5.1 of [Simo and Hughes \[1998\]](#).

319 The rate $\dot{\lambda}$ is positive for change in the local equivalent plastic strain,

$$\dot{\lambda} = \sqrt{\dot{\boldsymbol{\epsilon}}^{\text{P}} : \mathbf{B}_\lambda : \dot{\boldsymbol{\epsilon}}^{\text{P}}} \geq 0.$$

320 Note that $\dot{\lambda}$ is degree one homogeneous in $\dot{\boldsymbol{\epsilon}}^{\text{P}}$, because $(\partial \dot{\lambda} / \partial \dot{\boldsymbol{\epsilon}}^{\text{P}}) : \dot{\boldsymbol{\epsilon}}^{\text{P}} = \dot{\lambda}$. Furthermore, $\dot{\lambda} \in \mathbb{R}$ as $\dot{\boldsymbol{\epsilon}}^{\text{P}} : \mathbf{B}_\lambda :$
321 $\dot{\boldsymbol{\epsilon}}^{\text{P}} \geq 0$ for all $\dot{\boldsymbol{\epsilon}}^{\text{P}}$.

322 2.3 Anisotropic plastic regularization for non-coaxial plastic flow

323 The energy functional W^{P} in Eq. (3) contains two types of energy functionals, i.e. [[Aldakheel and Miehe,](#)
324 [2017, Forest, 2009](#)],

$$W_{\tilde{\boldsymbol{\alpha}}}^{\text{P}}(\boldsymbol{\alpha}, \tilde{\boldsymbol{\alpha}}) = \underbrace{\frac{k_\lambda}{2} (\tilde{\lambda} - \lambda)^2 + \frac{k_v}{2} (\tilde{\boldsymbol{\epsilon}}_v^{\text{P}} - \boldsymbol{\epsilon}_v^{\text{P}})^2}_{\text{penalty functionals}} + \underbrace{\frac{K_\lambda l_\lambda^2}{2} \nabla \tilde{\lambda} \cdot \boldsymbol{\omega}_\lambda \cdot \nabla \tilde{\lambda} + \frac{K_v l_v^2}{2} \nabla \tilde{\boldsymbol{\epsilon}}_v^{\text{P}} \cdot \boldsymbol{\omega}_v \cdot \nabla \tilde{\boldsymbol{\epsilon}}_v^{\text{P}}}_{\text{anisotropic regularization functionals}}, \quad (13)$$

325 where $\boldsymbol{\alpha} = \{\lambda, \boldsymbol{\epsilon}_v^{\text{P}}\}$ and $\tilde{\boldsymbol{\alpha}} = \{\tilde{\lambda}, \tilde{\boldsymbol{\epsilon}}_v^{\text{P}}\}$, k_λ and k_v are stiffness parameters, and penalize difference between
326 local internal variables and field values of $\tilde{\lambda}$ and $\tilde{\boldsymbol{\epsilon}}_v^{\text{P}}$. $K_\lambda > 0$ and $K_v > 0$ are moduli which have the same

unit as a stiffness, and $l_\lambda > 0$ and $l_v > 0$ are length scale parameters corresponding to the regularized variables $\tilde{\lambda}$ and $\tilde{\epsilon}_v^p$ respectively.

The first type of energy functionals are the relaxation functionals that penalize the difference between local internal variables and field variables measured by the L_2 norm. The second type of energy functionals are weighted inner products of the gradient of the corresponding field variables that introduce the gradient dependence and the non-coaxiality of the plastic flow. The Euler-Lagrange equation of these two types of energy functional lead to two modified Helmholtz equations of which the corresponding Galerkin form is solved via the finite element method in this work. Notice that the second-order positive-definite diffusivity tensors ω_λ and ω_v , are weighting functions in the weighted inner product. They are used to introduce anisotropy on the gradient-dependence of the field variables $\tilde{\lambda}$ and $\tilde{\epsilon}_v^p$. Since both ω_λ and ω_v are not isotropic tensors, a bias is therefore introduced in the regularization such that the gradient dependencies are stronger in the the principal directions corresponding to the largest eigenvalues of ω_λ and ω_v than those corresponding to smaller eigenvalues. In other words, the plastic flow direction of each material point is therefore not only depending on the stress gradient of the yield function at the material point but also depends on the directionally biased influence of the constitutive responses of the neighbors characterized by ω_λ and ω_v . Consequently, the resultant gradient-enhanced plasticity model is associative, but the plastic flow direction is not coaxial to the stress gradient of the conventional MCC yield function due to the anisotropic regularization.

Note that the anisotropy introduced by the anisotropic diffusivity tensors ω_λ and ω_v are of different natures than those introduced at the local constitutive laws. In particular, the anisotropic effect introduced via the anisotropic diffusivity tensors exhibits scale effects. Furthermore, since the principal directions of the anisotropic diffusivity tensors are independent of the mapping operators used to introduce anisotropy into the local constitutive law, the Euler angles between the isotropic plane of the local plasticity model and the principal directions of tensors ω_λ and ω_v can be leveraged to generate a fuller anisotropic constitutive responses for complex materials for which the anisotropic responses are originated from multiple geometrical attributes across length scales (e.g. joints, layers, fabrics, slip systems, lattice).

Remark 1. To simplify the material identification procedure, analogously to the parameter selection in Miede et al. [2013] or Aldakheel [2017], we associate the volumetric term with the volumetric stiffness constant,

$$K_\lambda \sim a_\lambda = a_v, \quad K_v \sim a_v = \frac{1}{3} \mathbf{1} : \mathbf{C}^e : \mathbf{1}, \quad (14)$$

where our notation appropriates that of Walpole [1984]. Within the Walpole notation for elastic isotropy, $a = \mathbf{1} : \mathbf{C}^e : \mathbf{1}/3$, where the bulk modulus $K = a/3$. Calibration of the regularization might alternatively include inverse problems, against strain gradients obtained from triaxial tests [Wang et al., 2016]. That said, our 2D and 3D numerical examples consistently converge through strain softening.

Note that, for a given set of fixed length scale parameters, l_λ and l_v , the discrepancy between the local and the projected internal variables, and the spatial distribution of the projected internal variables are affected by the ratios K_λ/k_λ and K_v/k_v . If these ratios are low, then the discrepancy between the local and the field variables is lower but the field variables may exhibit sharper spatial gradients. If these ratios are high, then the sharp gradient of the projected internal variables may not be admissible, but the discrepancy between the local and field variables could be larger.

Now consider the tensor ω_λ (or ω_v) that describes microstructural attributes aligned with the unit vector l_λ for $l_\lambda \cdot l_\lambda = 1$.

Hence, one may express the tensor ω_λ as a function of the tensors $\phi_\lambda = l_\lambda \otimes l_\lambda$ and $\chi_\lambda = \mathbf{1} - l_\lambda \otimes l_\lambda$. Due to the orthogonality and idempotence of ϕ_λ and χ_λ , in the combined formalism of Clayton and Knap [2015], Teichtmeister et al. [2017], and Bryant and Sun [2018], the definition of this mapping relates

$$\omega_\lambda = (\mathbf{p}_\lambda \otimes \mathbf{p}_\lambda) : \mathbf{1} = \mathbf{1} + \phi_\lambda \phi_\lambda + \chi_\lambda \chi_\lambda, \quad \mathbf{p}_\lambda = \phi_\lambda \sqrt{1 + \phi_\lambda} + \chi_\lambda \sqrt{1 + \chi_\lambda}, \quad (15)$$

where coefficients ϕ_λ and χ_λ are dimensionless, as is tensor ω_λ . Coefficients $\phi_\lambda \geq -1$ and $\chi_\lambda \geq -1$, such that ω_λ is positive semidefinite. Physically, $\phi_\lambda \gg 0$ penalizes field variable diffusion on planes normal to l_λ , whereas $\chi_\lambda \gg 0$ penalizes damage diffusion on planes not normal to normal vector l_λ . For $\phi_\lambda = \chi_\lambda = 0$, $\mathbf{p}_\lambda = \mathbf{1}$ such that the mapping reduces to isotropy. $\phi_\lambda \neq \chi_\lambda$ indicates ω_λ is a tensor with one unique and one repeated eigenvalue. These statements apply equally to ω_v .

373 2.4 Incremental stored plastic work

374 Our objective is to an incremental form of the stored work functionals, such that the incremental constitu-
 375 tive update can be associated with the Euler-Lagrange equation of a discrete functional (seenext section).
 376 In particular, we employ a backward-implicit Euler method to integrate plastic work. Consider a finite set
 377 consisting of discrete snapshots of time instants $\{t_0, \dots, t_n, t_{n+1}\}$, for n the time step, with the data at prior
 378 time t_1, t_2, \dots, t_n given. At the new time t_{n+1} , the elastoplastic strain terms are

$$\epsilon_{n+1} = \epsilon_{n+1}^e + \epsilon_{n+1}^p, \quad (\cdot)_{n+1} = (\cdot)_n + \Delta(\cdot)|_n^{n+1}. \quad (16)$$

The local stored plastic work has been defined in the mapped-isotropic strain-space by [Ortiz and Pandolfi \[2004\]](#), as

$$W_{\alpha n+1}^p - W_{\alpha n}^p = \underbrace{\frac{1}{2} \left[W_c^p(\epsilon_{v n+1}^p) - W_c^p(\epsilon_{v n}^p) \right]}_{\text{matched coefficients } 1/2 \text{ and } M/2 \text{ return MCC yield criterion}} - \overbrace{\frac{M}{2} (\lambda_{n+1} - \lambda_n) \left[\partial_{\epsilon_v^p} W_c^p(\epsilon_{v n+1}^p) \right]}^{\text{ensure } p_{c n+1} \leq 0}. \quad (17)$$

Note the Lagrange multiplier term $M(\lambda_{n+1} - \lambda_n)p_{c n+1}/2 = -\Delta\lambda\sigma_{q n+1}$ enforces non-positivity of the preconsolidation pressure $p_{c n+1}$. The limits of the partial derivatives

$$\frac{\partial W_{\alpha n+1}^p}{\partial \Delta\lambda} = \frac{M}{2} \partial_{\epsilon_v^p} W_c^p = \sigma_{q n+1}, \quad \frac{\partial W_{\alpha n+1}^p}{\partial \epsilon_v^p} = \frac{1}{2} \partial_{\epsilon_v^p} W_c^p - \frac{M}{2} \Delta\lambda \partial_{\epsilon_v^p}^2 W_c^p = \sigma_{p n+1}, \quad (18)$$

are

$$\lim_{\Delta\lambda \rightarrow 0} \sigma_{q n+1} = \lim_{\Delta\lambda \rightarrow 0} \left(\frac{\partial W_{\alpha n+1}^p}{\partial \Delta\lambda} \right) = -\frac{M}{2} p_{c n+1}, \quad \lim_{\Delta\lambda \rightarrow 0} \sigma_{p n+1} = \lim_{\Delta\lambda \rightarrow 0} \left(\frac{\partial W_{\alpha n+1}^p}{\partial \epsilon_v^p} \right) = \frac{1}{2} p_{c n+1}. \quad (19)$$

379 These results are later used to estimate the connection between the two-invariant yield surface and the
 380 incremental energy functional, following the treatments in [Ortiz and Stainier \[1999\]](#) and [Ortiz and Pandolfi
 381 \[2004\]](#) in Section 2.5.2.

Remark 2. Albeit not considered in this study, anisotropy-adapted viscoplastic regularization is similarly intuitive. One possible way to incorporate viscoplasticity in a variational framework is via appending to the local stored incremental plastic work a term similar to,

$$\frac{\eta_\lambda}{2\Delta t} (\lambda_{n+1} - \lambda_n)^2 + \frac{\eta_v}{2\Delta t} (\epsilon_{v n+1}^p - \epsilon_{v n}^p)^2,$$

382 where η_λ and η_v are material parameters and $\Delta t = t_{n+1} - t_n$ is the time increment (cf. [Ortiz and Pandolfi
 383 \[2004\]](#), [Ortiz and Stainier \[1999\]](#)).

384 2.5 Variational constitutive update with anisotropic micromorphic regularization

385 We derive an discrete energy functional whose Euler-Lagrange equation leads to the governing equation of
 386 the local constitutive law and the Helmholtz equations that regularize the boundary value problem. Mean-
 387 while Following Eq. (3.3-13) in [Yang et al. \[2006\]](#) e.g., we suppose the mechanical equilibrium equation's
 388 numerical solution is staggered w.r.t. solution of the regularizing Helmholtz equations. This staggering is
 389 in-line with solution of the mechanically-coupled scalar diffusion equations in [Armero and Simo \[1992\]](#),
 390 for instance.

391 Furthermore, we employ the variational principle to obtain the Helmholtz equations for $\tilde{\lambda}$ and $\tilde{\epsilon}_v^p$ from
 392 the corresponding energy functional. Following the variational update for regularized viscoplastic mod-
 393 els (e.g. [Aldakheel \[2017\]](#)), the local constitutive update and the corresponding equations that govern the
 394 micromorphic regularization can be obtained from one discrete incremental energy functional. From this
 395 single incremental energy functional, we may derive the discrete Euler-Lagrange equation, a system of

396 nonlinear equations that constitute both the local constitutive update and the the micromorphic field equa-
 397 tions [Aldakheel and Miehe, 2017].

398 This system of equations is solved via an operator-split scheme. The local constitutive updates are
 399 solved in a semi-implicit manner, in the sense that the incremental constitutive laws that updates the local
 400 internal variables and the stress are updated via a Newton solver while the incremental solutions of the
 401 Helmholtz equations are fixed. Meanwhile, when the incremental solutions of the Helmholtz equations
 402 are updated, the internal variables are frozen. Further discussions about the operator-split scheme can be
 403 found in Aldakheel and Miehe [2017], Choo and Sun [2017], Miehe et al. [2010, 2015], Sun [2015], Wheeler
 404 et al. [2014]. In this work, the Cauchy stress is integrated incrementally via a return mapping algorithm.
 405 As result, we have,

$$\epsilon_{n+1}^e = \epsilon_{n+1}^{e \text{ tr}} - \Delta \epsilon^P, \quad \epsilon_{n+1}^{e \text{ tr}} = \epsilon_{n+1} - \epsilon_n^P, \quad (20)$$

406 where $\epsilon_{n+1}^{e \text{ tr}}$ is the trial elastic strain. The strain and hence elastic trial strain are fixed while solving the local
 407 optimization problem, as we employ a standard return mapping algorithm. Thus

$$\frac{\partial \epsilon_{n+1}^P}{\partial \Delta \epsilon^P} = - \left. \frac{\partial \epsilon_{n+1}^e}{\partial \Delta \epsilon^P} \right|_{\epsilon_{n+1}^{e \text{ tr}}} = \mathbf{I}, \quad \left. \frac{\partial \epsilon_{n+1}}{\partial \Delta \epsilon^P} \right|_{\Delta \epsilon} = \mathbf{0},$$

during the constitutive update, the algorithm by which we obtain $\sigma_{n+1} = \mathbf{C}^e : \epsilon_{n+1}^e$. Then, the identity
 ϵ_{n+1}^e in Eq. (20) defines the local minimization problem in the elastic strains. This implies the generalized
 coordinates

$$\zeta_{n+1} = \{\epsilon_{n+1}^e, \tilde{\lambda}_{n+1}, \tilde{\epsilon}_{v \ n+1}^P\}, \quad (21)$$

where Eq. (13) is used. For a given strain at an incremental step ϵ_{n+1} , the constitutive updates is associated
 with the Euler-Lagrange equation of the constrained optimization problem which reads,

$$\tilde{\zeta}_{n+1} = \arg \min_{\zeta_{n+1}} W(\zeta_{n+1}). \quad (22)$$

408 subjected to the following constraint,

$$\Delta \lambda = \sqrt{\Delta \epsilon_{n+1}^P : \mathbf{B}_\lambda : \Delta \epsilon_{n+1}^P} \geq 0, \quad \Delta \epsilon_{v \ n+1}^P = \mathbf{b}_v : \Delta \epsilon_{n+1}^P. \quad (23)$$

Note that the inequality in (23) is satisfied if \mathbf{B}_λ is positive semi-definite (or positive definite). The mi-
 cromorphic field equation that governs the relations between the global and local internal variables are
 obtained from the stationary conditions of Eq. (22) with respect to the global internal variables $\tilde{\lambda}_{n+1}$ and
 $\tilde{\epsilon}_{v \ n+1}^P$, i.e.,

$$\frac{\delta W(\zeta_{n+1})}{\delta \tilde{\lambda}_{n+1}} = k_\lambda (\tilde{\lambda}_{n+1} - \lambda_{n+1}) - K_\lambda l_\lambda^2 \nabla \cdot (\omega_\lambda \cdot \nabla \tilde{\lambda}_{n+1}) = 0, \text{ in } \mathcal{B}, \quad (24)$$

$$\frac{\delta W(\zeta_{n+1})}{\delta \tilde{\epsilon}_{v \ n+1}^P} = k_v (\tilde{\epsilon}_{v \ n+1}^P - \epsilon_{v \ n+1}^P) - K_v l_v^2 \nabla \cdot (\omega_v \cdot \nabla \tilde{\epsilon}_{v \ n+1}^P) = 0, \text{ in } \mathcal{B}, \quad (25)$$

where the trivial boundary conditions, e.g. $\hat{\mathbf{n}} \cdot \omega_\lambda \cdot \nabla \tilde{\lambda}_{n+1} = 0$ on $\partial \mathcal{B}$, are applied. On the other hand, the
 system of equations for the local constitutive updates can be obtained incrementally from the first variation
 of $W(\zeta_{n+1})$ with respect to the elastic strain ϵ_{n+1}^e (see Appendix C.1 for the detailed derivation), i.e.,

$$\begin{aligned} \frac{\delta W(\zeta_{n+1})}{\delta \epsilon_{n+1}^e} &= \overbrace{\sigma_{n+1} - \sigma_{q \ n+1} \frac{\partial \Delta \lambda}{\partial \Delta \epsilon^P}}^{\text{purely local terms}} - \sigma_{p \ n+1} \mathbf{b}_v \\ &\quad + \overbrace{k_\lambda (\tilde{\lambda}_{n+1} - \lambda_{n+1}) \frac{\partial \Delta \lambda}{\partial \Delta \epsilon^P} + k_v (\tilde{\epsilon}_{v \ n+1}^P - \epsilon_{v \ n+1}^P) \mathbf{b}_v}_{\text{micromorphic terms}} = \mathbf{0}, \end{aligned} \quad (26)$$

409 where we used the definitions of σ_{n+1} , $\partial W_{\alpha \ n+1}^P / \partial \Delta \lambda$, and $\partial W_{\alpha \ n+1}^P / \partial \epsilon_{v \ n+1}^P$.

410 *Remark 3.* Direct substitution of law Eq. (7) curtails hardening force-related expressions otherwise prolif-
 411 erating in local-to-global variational updates, cf. e.g. [Aldakheel \[2017\]](#). Similarly per Section 2.4, viscoplas-
 412 ticity incorporates by a quadratic function of the plastic strain increment. Thus the regularized constitutive
 413 update devolves to minimization Eq. (22).

414 2.5.1 Yield criterion

415 In the Euler-Lagrange Eq. (26), substitute $\partial\Delta\lambda/\partial\Delta\epsilon^P = \mathbf{B}_\lambda : \mathbf{n}_{n+1}$ such that

$$\mathbf{0} = \boldsymbol{\sigma}_{n+1} - \sigma_{q\ n+1} \mathbf{B}_\lambda : \mathbf{n}_{n+1} - \sigma_{p\ n+1} \mathbf{b}_v + k_\lambda (\tilde{\lambda}_{n+1} - \lambda_{n+1}) \mathbf{B}_\lambda : \mathbf{n}_{n+1} + k_v (\tilde{\epsilon}_v^P - \epsilon_v^P) \mathbf{b}_v. \quad (27)$$

416 Interiority within the elastic domain can be determined as follows. Rearranging the Euler-Lagrange equa-
 417 tion to solve for \mathbf{n}_{n+1} . At the trail state $\epsilon_{n+1}^e = \epsilon_{n+1}^{e\ tr}$, the tensorial flow direction evaluates as

$$\mathbf{n}_{n+1}^{tr} = \frac{1}{\sigma_{q\ n+1}^{tr} - k_\lambda (\tilde{\lambda}_{n+1} - \lambda_{n+1}^{tr})} \mathbf{B}_\lambda^{-1} : \left[\boldsymbol{\sigma}_{n+1}^{tr} - \sigma_{p\ n+1}^{tr} \mathbf{b}_v + k_v (\tilde{\epsilon}_v^P - \epsilon_v^{P\ tr}) \mathbf{b}_v \right]. \quad (28)$$

If within the elastic domain, by the kinematic constraint on the tensorial direction in Eq. (12), the yield criterion can be written as

$$\varphi(\mathbf{n}_{n+1}^{tr}) = \mathbf{n}_{n+1}^{tr} : \mathbf{B}_\lambda : \mathbf{n}_{n+1}^{tr} - 1 \leq 0, \quad (29)$$

418 expressed quadratically in \mathbf{n}_{n+1}^{tr} to recover the yield criterion in quadratic terms of the mapped stress
 419 invariants (next section). Note that Eq. (27), Eq. (28), and Eq. (29) combine to completely describe the varia-
 420 tional update applied in Section 4.1. Followingly, change in the field variables $\tilde{\lambda}$ and $\tilde{\epsilon}_v^P$ not just regularizes
 421 but can also trigger the onset of local yielding.

422 2.5.2 Mapped two-invariant yield criterion

Now we establish the connection between our derivation based on the variational principle and the formu-
 lation in [Semnani et al. \[2016\]](#). The superscript tr is dropped for brevity. First, assume that $\mathbf{b}_v = \mathbf{P}^{\text{vol}-1} : \mathbf{1}$.
 Then, we eliminate the gradient dependence of the plastic flow by setting $k_\lambda = k_v = 0$. By substituting the
 definition of \mathbf{n}_{n+1} in (28) into the yield function and simplifying the expression, we obtain,

$$\frac{\sigma_{q\ n+1}^2}{M^2} \varphi_{n+1} = \left(p_{n+1}^* - \sigma_{p\ n+1} \right)^2 + \frac{1}{M^2} \left(q_{n+1}^{*2} - \sigma_{q\ n+1}^2 \right) \leq 0. \quad (30)$$

Applying the relations in Eq. (19), Eq. 30 can be rewritten as,

$$\boxed{\lim_{\Delta\lambda \rightarrow 0} \left(\frac{\sigma_{q\ n+1}^2}{M^2} \varphi_{n+1} \right) = p_{n+1}^* \left(p_{n+1}^* - p_{c\ n+1} \right) + \frac{q_{n+1}^{*2}}{M^2} \leq 0,} \quad (31)$$

423 at time step t_{n+1} , i.e. a necessary condition for the stress to be admissible. As a result, our model may
 424 be reduced to the anisotropic yield function in [Semnani et al. \[2016\]](#) when the gradient regularization
 425 vanishes. It can also be reduced to the classical modified Cam-clay model (cf. Eq. (6.18) in [Borja \[2013\]](#)
 426 when the mapping becomes identity).

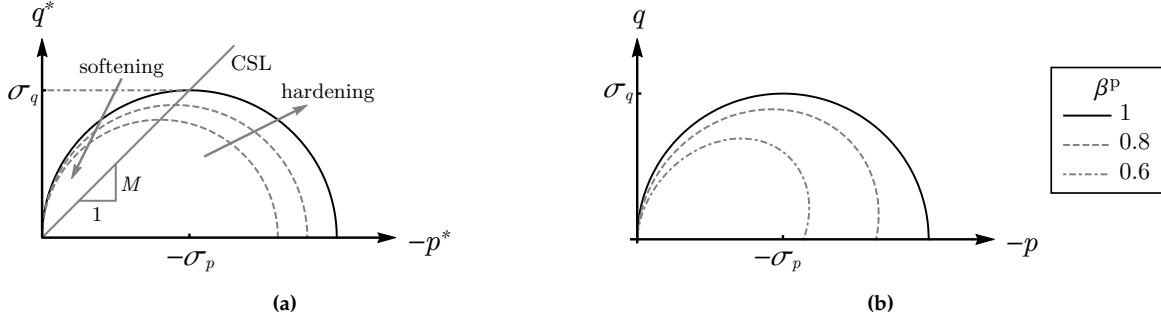


Fig. 3: Geometric interpretation of the mapped two-invariant yield criterion, Eq. (30): (a) introducing M as the slope of the critical state line (CSL) in the starred scalar space, after Ortiz and Pandolfi [2004], and with softening and hardening trends after Borja [2013]; and, (b) unmapped two-invariant yield criterion parameterized by the mapping coefficient, varying $\beta^{\text{dev}} = \beta^{\text{vol}}$ at fixed $\alpha^{\text{dev}} = \alpha^{\text{vol}} = \gamma^{\text{dev}} = \gamma^{\text{vol}} = 1$, after Semnani et al. [2016].

3 Balance and evolution equations

We solve the balance of linear equilibrium equation, i.e.

$$\nabla \cdot \boldsymbol{\sigma} + \rho \mathbf{g} = \mathbf{0}, \quad (32)$$

where $\boldsymbol{\sigma}$ is the Cauchy stress, ρ the density, and \mathbf{g} the gravitational acceleration vector. We employ a hyperelastic energy functional such that the stress $\boldsymbol{\sigma} = \partial W^e / \partial \boldsymbol{\epsilon}^e$. Hence, the local internal variables λ and $\boldsymbol{\epsilon}_v^p$ are updated incrementally once the solution of the nonlinear static equilibrium equation is obtained via an implicit solver, with the same local-to-global hierarchy described in Weinberg et al. [2006], regarding the variational constitutive update.

However, to introduce nonlocality in the constitutive law, we supply an additional set of governing equations to evolve the field variables $\tilde{\lambda}$ and $\tilde{\boldsymbol{\epsilon}}_v^p$. Both evolution equations are characterized variationally via introduction of diffusive functionals in Eq. (13), which depends on the spatial gradients of $\tilde{\lambda}$ and $\tilde{\boldsymbol{\epsilon}}_v^p$. In practice, we solve an equivalent nondimensionalized system (cf. Forest [2009]) with Laplacian coefficients of the regularization equation

$$\tilde{l}_\lambda = l_\lambda \sqrt{K_\lambda / k_\lambda}, \quad \tilde{l}_v = l_v \sqrt{K_v / k_v}. \quad (33)$$

Thus, each field variable accords with some Helmholtz equation, e.g.

$$\tilde{\alpha} - \tilde{l}^2 \nabla \cdot (\boldsymbol{\omega} \cdot \nabla \tilde{\alpha}) = \alpha, \quad (34)$$

for $\tilde{\alpha}$ a field variable, α the corresponding internal variable, \tilde{l} a length, and $\boldsymbol{\omega}$ a dimensionless second-order tensor. The only imposed boundary condition for the Helmholtz equations is the trivial Neumann boundary condition.

This technique is referred to as micromorphic regularization in Forest [2009] and Miehe et al. [2013]. The nondimensionalizations $\sqrt{K_\lambda / k_\lambda}$ and $\sqrt{K_v / k_v}$ help us to explain convergence towards mesh independence even during material softening. See the results section, and for explanatory analysis Aldakheel [2017].

4 Local-global constitutive updates

Due to the introduction of the micromorphic regularization, the constitutive update is obtained from a global-local split algorithm, such that: the global evolution equations updates the strain and the micromorphic field variables, while the local return mapping algorithm provides the incremental updates of the

445 elastic (and equivalently the plastic) strain, internal variables, and plastic flow direction [Aldakheel, 2017].
 446 The governing equations for the micromorphic regularization are obtained from the stationary condition
 447 of the energy functional listed in Eq. (22). The elastic strain ϵ_{n+1}^e is defined from the strain update in Eq.
 448 (20), and results from optimality of the local minimization problem.

449 4.1 Local system

450 The local incremental stress update is obtained by a conventional return mapping algorithm. For clarity,
 451 the algorithm is summarized in Alg. 1. As necessary, we map or reconstruct required symmetric tensors
 452 from their Kelvin-notated vector equivalents per Eq. (44), and super-symmetric fourth-order tensors per
 453 Eq. (45), Appendix A.

Algorithm 1 Local return-mapping

Require: From the global system, the strain increment $\Delta\epsilon$ as well as, for the micromorphic regularization,
 field variables $\tilde{\lambda}$ and $\tilde{\epsilon}_v^p$

- 1: A trial state is established
 - a. set $\epsilon_{n+1}^{e\ tr} = \epsilon_{n+1}^e + \Delta\epsilon$, $\lambda_{n+1}^{tr} = \lambda_n$, $\epsilon_{v\ n+1}^p = \epsilon_v^p$, $\sigma_{q\ n+1}^{tr} = \sigma_{0\ n}$, and $\sigma_{p\ n+1}^{tr} = p_{0\ n}$
 - b. evaluate n_{n+1}^{tr} per Eq. (28)
 - 2: **if** $\varphi(n_{n+1}^{tr}) \leq 0$ **then**
 - a. the deformation is elastic per Eq. (29), set internal variables $(\cdot)_{n+1} = (\cdot)_{n+1}^{tr}$
 - b. set $\sigma_{n+1} = \mathbf{C}^e : \epsilon_{n+1}^e$ and the solid tangent \mathbf{C}^e
 - 3: **else**
 - a. the deformation is inelastic, obtain the local system by parameterizing the Euler-Lagrange equation with $n(\Delta\epsilon_{n+1}^p)$, $\lambda(\Delta\epsilon_{n+1}^p)$, and $\epsilon_v^p(\Delta\epsilon_{n+1}^p)$ under dependence $\Delta\epsilon^p(\epsilon_{n+1}^e)$
 - b. at local system iteration $k = 0$, guess the initial solution per Eq. (37)
 - c. using Newton's method or a variant, iteratively solve the local nonlinear system for ϵ_{n+1}^e
 - d. set $\sigma_{n+1} = \mathbf{C}^e : \epsilon_{n+1}^e$ and the solid tangent \mathbf{C}_{n+1}^{ep} per Eq. (41)
 - 4: Return mapping completes
 - a. w.r.t the equilibrium equation, pass to the global system the stress σ_{n+1} and the solid tangent
 - b. for the micromorphic regularization, also pass the local variables λ_{n+1} and $\epsilon_{v\ n+1}^p$
-

454 Local nonlinearity is treated as follows. Define the local numerical system and residual in matrix-vector
 455 notation:

$$\left. \begin{aligned} \bar{\mathbf{x}}^k &= \left[\bar{\epsilon}_{n+1}^e \right]_{6 \times 1}^k \\ \bar{\mathbf{r}}^k &= \left[\mathbf{C}^e \bar{\epsilon}_{n+1}^e - \sigma_{q\ n+1} \mathbf{B}_\lambda \bar{\mathbf{n}}_{n+1} - \sigma_{p\ n+1} \bar{\mathbf{b}}_v \right. \\ &\quad \left. + k_\lambda (\tilde{\lambda}_{n+1} - \lambda_{n+1}) \mathbf{B}_\lambda \bar{\mathbf{n}}_{n+1} + k_v (\tilde{\epsilon}_{v\ n+1}^p - \epsilon_{v\ n+1}^p) \bar{\mathbf{b}}_v \right]_{6 \times 1}^k \end{aligned} \right\} \quad (35)$$

where k is the iteration, $\bar{\mathbf{x}}^k$ the Kelvin-notated vector equivalent of the local unknowns at k , $\bar{\mathbf{r}}^k$ the Kelvin-notated vector equivalent of the local residual at k , $\bar{\mathbf{b}}_v$ the Kelvin-notated vector equivalent of \mathbf{b}_v , and \mathbf{B}_λ the Kelvin-notated vector equivalent of \mathbf{B}_λ (for bold font and overline notation convention for Kelvin-notated equivalents, see Appendix A). The local tangent operator is then

$$\left. \frac{\partial \bar{\mathbf{r}}}{\partial \bar{\mathbf{x}}} \right|_{\bar{\epsilon}_{n+1}^{e\ tr}}^k = \left[\frac{\partial \bar{\mathbf{r}}}{\partial \bar{\epsilon}_{n+1}^e} \right]_{6 \times 6}^k, \quad (36)$$

as derived in Appendix C.1, where

$$\begin{aligned} \frac{\partial \bar{\mathbf{r}}}{\partial \bar{\boldsymbol{\epsilon}}_{n+1}^e} &= \mathbf{C}^e + \frac{\sigma_{q,n+1}}{\Delta \lambda} \left[\mathbf{B}_\lambda - (\mathbf{B}_\lambda \bar{\mathbf{n}}_{n+1}) (\mathbf{B}_\lambda \bar{\mathbf{n}}_{n+1})^\top \right] - \frac{M}{2} \partial_{\bar{\boldsymbol{\epsilon}}_v^e} p_{c,n+1} \left[(\mathbf{B}_\lambda \bar{\mathbf{n}}_{n+1}) \bar{\mathbf{b}}_v^\top + \bar{\mathbf{b}}_v (\mathbf{B}_\lambda \bar{\mathbf{n}}_{n+1})^\top \right] \\ &+ \frac{1}{2} \left(\partial_{\bar{\boldsymbol{\epsilon}}_v^e} p_{c,n+1} - M \Delta \lambda \partial_{\bar{\boldsymbol{\epsilon}}_v^e}^2 p_{c,n+1} \right) \bar{\mathbf{b}}_v \bar{\mathbf{b}}_v^\top - \frac{k_\lambda (\bar{\lambda}_{n+1} - \lambda_{n+1})}{\Delta \lambda} \left[\mathbf{B}_\lambda - (\mathbf{B}_\lambda \bar{\mathbf{n}}_{n+1}) (\mathbf{B}_\lambda \bar{\mathbf{n}}_{n+1})^\top \right] \\ &+ k_\lambda (\mathbf{B}_\lambda \bar{\mathbf{n}}_{n+1}) (\mathbf{B}_\lambda \bar{\mathbf{n}}_{n+1})^\top + k_v \bar{\mathbf{b}}_v \bar{\mathbf{b}}_v^\top, \end{aligned}$$

and

$$\bar{\mathbf{n}}_{n+1} = \frac{\mathbf{B}_\lambda \Delta \bar{\boldsymbol{\epsilon}}^P}{\Delta \lambda} = \frac{\mathbf{B}_\lambda \Delta \bar{\boldsymbol{\epsilon}}^P}{\sqrt{\Delta \bar{\boldsymbol{\epsilon}}^P \top \mathbf{B}_\lambda \Delta \bar{\boldsymbol{\epsilon}}^P + k_{\bar{\boldsymbol{\epsilon}}}}} \quad \text{for } \Delta \bar{\boldsymbol{\epsilon}}^P = \bar{\boldsymbol{\epsilon}}_{n+1}^{e \text{ tr}} - \bar{\boldsymbol{\epsilon}}_{n+1}^e \quad \text{with } \mathbf{B}_\lambda \bar{\mathbf{n}}_{n+1} = \mathbf{B}_\lambda^\top \bar{\mathbf{n}}_{n+1}.$$

Small parameter $k_{\bar{\boldsymbol{\epsilon}}}$ is taken as 1×10^{-15} .

Our local tangent matrix $(\partial \bar{\mathbf{r}} / \partial \bar{\boldsymbol{\epsilon}})^{k'}$'s symmetry redounds to the model design's variational consistency, the hallmark of which is the cascading dependence $p_c(\Delta \bar{\boldsymbol{\epsilon}}^P)$ and $\Delta \bar{\boldsymbol{\epsilon}}^P(\bar{\boldsymbol{\epsilon}}_{n+1}^e)$, in this the MCC context.

4.1.1 Trial state

Converging a local system requires passing an initial guess to Newton's method. Our guess, at iteration $k = 0$, approximates the elastic trial state:

$$\bar{\boldsymbol{\epsilon}}_{n+1}^{e \ k=0} = \left[\bar{\boldsymbol{\epsilon}}_{n+1}^{e \ \text{tr}} - \Delta \lambda \bar{\mathbf{n}}_{n+1}^{\text{tr}} \right]_{6 \times 1}^{k=0} \quad \text{for } \Delta \bar{\boldsymbol{\epsilon}}^P \ k=0 = \left[\Delta \lambda \bar{\mathbf{n}}_{n+1}^{\text{tr}} \right]_{6 \times 1}^{k=0}. \quad (37)$$

Thus at $k = 0$ we set $\bar{\boldsymbol{\epsilon}}_{n+1}^e \approx \bar{\boldsymbol{\epsilon}}_{n+1}^{e \ \text{tr}}$ and $\Delta \bar{\boldsymbol{\epsilon}}^P \approx \bar{\mathbf{0}}$, with $\Delta \lambda^{k=0}$ a small number taken as 1×10^{-10} .

4.1.2 Stored work update

In-line with the semilogarithmic relation, we use as derivatives

$$p_{c,n+1} = p_{c,n} \exp \left(\frac{\bar{\boldsymbol{\epsilon}}_{v,n+1}^e - \bar{\boldsymbol{\epsilon}}_{v,n+1}^{e \ \text{tr}}}{C_d} \right), \quad \partial_{\bar{\boldsymbol{\epsilon}}_v^e} p_{c,n+1} = -\frac{p_{c,n}}{C_d} \exp \left(\frac{\bar{\boldsymbol{\epsilon}}_{v,n+1}^e - \bar{\boldsymbol{\epsilon}}_{v,n+1}^{e \ \text{tr}}}{C_d} \right).$$

As such, the stored plastic work of consolidation's increments follow

$$W_{c,n+1}^P - W_{c,n}^P = p_{c,n} C_d \left[1 - \exp \left(\frac{\bar{\boldsymbol{\epsilon}}_{v,n+1}^e - \bar{\boldsymbol{\epsilon}}_{v,n+1}^{e \ \text{tr}}}{C_d} \right) \right] = C_d (p_{c,n} - p_{c,n+1}). \quad (38)$$

4.2 Consistent tangent operator (CTO)

A consistent tangent operator $\mathbf{C}_{n+1}^{\text{ep}} = \partial \bar{\boldsymbol{\sigma}}_{n+1} / \partial \bar{\boldsymbol{\epsilon}}_{n+1}$ is useful to converge the global system for the displacements, cf. Eq. (7.127-136) in de Souza Neto et al. [2008], also see the next section. The CTO is evaluated after convergence of the local system, when

$$\frac{\partial \bar{\boldsymbol{\epsilon}}_{n+1}^{e \ \text{tr}}}{\partial \bar{\boldsymbol{\epsilon}}_{n+1}^e} = \frac{\partial (\bar{\boldsymbol{\epsilon}}_n^{e \ \text{tr}} + \bar{\boldsymbol{\epsilon}}_{n+1} - \bar{\boldsymbol{\epsilon}}_n)}{\partial \bar{\boldsymbol{\epsilon}}_{n+1}^e} = \mathbf{I}, \quad \text{hence} \quad \frac{\partial \bar{\boldsymbol{\epsilon}}_{n+1}^{e \ \text{tr}}}{\partial \bar{\boldsymbol{\epsilon}}_{n+1}^e} = \frac{\partial \bar{\boldsymbol{\epsilon}}_{n+1}^{e \ \text{tr}}}{\partial \bar{\boldsymbol{\epsilon}}_{n+1}^e} : \frac{\partial \bar{\boldsymbol{\epsilon}}_{n+1}}{\partial \bar{\boldsymbol{\epsilon}}_{n+1}^e} = \frac{\partial \bar{\boldsymbol{\epsilon}}_{n+1}}{\partial \bar{\boldsymbol{\epsilon}}_{n+1}^e},$$

whereas

$$\left. \frac{\partial \Delta \bar{\boldsymbol{\epsilon}}^P}{\partial \bar{\boldsymbol{\epsilon}}_{n+1}^e} \right|_{\bar{\boldsymbol{\epsilon}}_{n+1}^e} = \left. \frac{\partial (\bar{\boldsymbol{\epsilon}}_{n+1}^{e \ \text{tr}} - \bar{\boldsymbol{\epsilon}}_{n+1}^e)}{\partial \bar{\boldsymbol{\epsilon}}_{n+1}^e} \right|_{\bar{\boldsymbol{\epsilon}}_{n+1}^e} = -\mathbf{I}, \quad \left. \frac{\partial \Delta \bar{\boldsymbol{\epsilon}}^P}{\partial \bar{\boldsymbol{\epsilon}}_{n+1}^{e \ \text{tr}}} \right|_{\bar{\boldsymbol{\epsilon}}_{n+1}^{e \ \text{tr}}} = \left. \frac{\partial (\bar{\boldsymbol{\epsilon}}_{n+1}^{e \ \text{tr}} - \bar{\boldsymbol{\epsilon}}_{n+1}^e)}{\partial \bar{\boldsymbol{\epsilon}}_{n+1}^{e \ \text{tr}}} \right|_{\bar{\boldsymbol{\epsilon}}_{n+1}^{e \ \text{tr}}} = \mathbf{I}.$$

469 As CTO is evaluated after convergence of the local system, we drop superscripts k and $n + 1$ and let $\bar{\mathbf{x}} = \bar{\boldsymbol{\epsilon}}^e$,
470 for the remainder of this section.

To identify the CTO, we rewrite the purely local Euler-Lagrange equation in residual form, as

$$\bar{\boldsymbol{\sigma}} - \bar{\mathbf{s}}(\Delta\bar{\boldsymbol{\epsilon}}^p) = \bar{\mathbf{0}} \quad (39)$$

471 where $\bar{\mathbf{s}}$ corresponds to the plastic back-stress as described in [Ortiz and Stainier \[1999\]](#), and is

$$\bar{\mathbf{s}}(\Delta\bar{\boldsymbol{\epsilon}}^p) = \sigma_q \frac{\mathbf{B}_\lambda \Delta\bar{\boldsymbol{\epsilon}}^p}{\sqrt{\Delta\bar{\boldsymbol{\epsilon}}^p \mathbf{T} \mathbf{B}_\lambda \Delta\bar{\boldsymbol{\epsilon}}^p}} + \sigma_p \bar{\mathbf{b}}_v \quad \text{and} \quad \Delta\bar{\boldsymbol{\epsilon}}^p = \bar{\boldsymbol{\epsilon}}^e \text{ tr} - \bar{\boldsymbol{\epsilon}}^e \quad \Rightarrow \quad \left. \frac{\partial \bar{\mathbf{r}}}{\partial \bar{\mathbf{x}}} \right|_{\bar{\boldsymbol{\epsilon}}^e \text{ tr}} = \mathbf{C}^e + \frac{\partial \bar{\mathbf{s}}}{\partial \Delta\bar{\boldsymbol{\epsilon}}^p},$$

472 assuming invertible $\partial \bar{\mathbf{r}} / \partial \bar{\mathbf{x}}$, the local system's tangent at the converged state from Eq. (36). Apply the identity
473 $\bar{\boldsymbol{\sigma}} = \mathbf{C}^e \bar{\boldsymbol{\epsilon}}^e$ and differentiate the Euler-Lagrange equation in residual form,

$$\frac{\partial}{\partial \bar{\boldsymbol{\epsilon}}^e} (\mathbf{C}^e \bar{\boldsymbol{\epsilon}}^e) - \frac{\partial \bar{\mathbf{s}}}{\partial \Delta\bar{\boldsymbol{\epsilon}}^p} \left(\left. \frac{\partial \Delta\bar{\boldsymbol{\epsilon}}^p}{\partial \bar{\boldsymbol{\epsilon}}^e} \right|_{\bar{\boldsymbol{\epsilon}}^e \text{ tr}} + \left. \frac{\partial \Delta\bar{\boldsymbol{\epsilon}}^p}{\partial \bar{\boldsymbol{\epsilon}}^e \text{ tr}} \right|_{\bar{\boldsymbol{\epsilon}}^e} \frac{\partial \bar{\boldsymbol{\epsilon}}^e \text{ tr}}{\partial \bar{\boldsymbol{\epsilon}}^e} \right) = \mathbf{C}^e - \frac{\partial \bar{\mathbf{s}}}{\partial \Delta\bar{\boldsymbol{\epsilon}}^p} \left(-\mathbf{I} + \mathbf{I} \frac{\partial \bar{\boldsymbol{\epsilon}}}{\partial \bar{\boldsymbol{\epsilon}}^e} \right) = \bar{\mathbf{0}}. \quad (40)$$

Rearranging for

$$\frac{\partial \bar{\boldsymbol{\epsilon}}}{\partial \bar{\boldsymbol{\epsilon}}^e} = \left(\frac{\partial \bar{\mathbf{s}}}{\partial \Delta\bar{\boldsymbol{\epsilon}}^p} \right)^{-1} \left(\mathbf{C}^e + \frac{\partial \bar{\mathbf{s}}}{\partial \Delta\bar{\boldsymbol{\epsilon}}^p} \right),$$

\mathbf{C}^{ep} is evaluated via the chain rule. Noting that $\mathbf{C}^{\text{ep}} = \partial \bar{\boldsymbol{\sigma}} / \partial \bar{\boldsymbol{\epsilon}} = \mathbf{C}^e (\partial \bar{\boldsymbol{\epsilon}}^e / \partial \bar{\boldsymbol{\epsilon}}) = \mathbf{C}^e (\partial \bar{\boldsymbol{\epsilon}} / \partial \bar{\boldsymbol{\epsilon}}^e)^{-1}$,

$$\mathbf{C}^{\text{ep}} = \left[\mathbf{C}^e \left(\frac{\partial \bar{\boldsymbol{\epsilon}}}{\partial \bar{\boldsymbol{\epsilon}}^e} \right)^{-1} \right]_{6 \times 6} = \left[\mathbf{C}^e \left(\left. \frac{\partial \bar{\mathbf{r}}}{\partial \bar{\mathbf{x}}} \right|_{\bar{\boldsymbol{\epsilon}}^e \text{ tr}} \right)^{-1} \left(\left. \frac{\partial \bar{\mathbf{r}}}{\partial \bar{\mathbf{x}}} \right|_{\bar{\boldsymbol{\epsilon}}^e \text{ tr}} - \mathbf{C}^e \right) \right]_{6 \times 6}, \quad (41)$$

474 where we have substituted to write \mathbf{C}^{ep} in \mathbf{C}^e , and $\partial \bar{\mathbf{r}} / \partial \bar{\mathbf{x}}$. As such, the consistent tangent computation
475 exclusively reuses the solid elastic tangent, \mathbf{C}^e , and the local tangent at the converged state, $\partial \bar{\mathbf{r}} / \partial \bar{\mathbf{x}}$. On
476 this point, contrast against [Semnani et al. \[2016\]](#). Consequently, our implementation is straightforward and
477 generic with respect to additional (e.g. micromorphic or viscoplastic) physics.

478 4.3 Spatial discretization

479 The stress $\boldsymbol{\sigma}$ and consistent tangent \mathbf{C}^{ep} evolved from solution of the quadrature point problem is used
480 to converge the global equilibrium equation for the displacements \mathbf{u} . Unless otherwise noted, the spatial
481 domain is discretized with standard low-order quadrilateral finite elements. The implementation of the
482 spatial discretization is done using the finite element library `deal.ii` [[Bangerth et al., 2007](#)], whereas the
483 implicit nonlinear PDE solver, including the assembly procedure of the residuals and the corresponding
484 tangents, and the Newton-Raphson scheme are modified from the software code base `geocentric` [[Choo
485 et al., 2016, White and Borja, 2008](#)].

486 5 Plastic flow near and at the anisotropic critical state

487 Consider Eq. (41). The local tangent is symmetric, and so is its inverse $(\partial \bar{\mathbf{r}} / \partial \bar{\mathbf{x}})^{-1}$. As such the product of
488 \mathbf{C}^e , $(\partial \bar{\mathbf{r}} / \partial \bar{\mathbf{x}})^{-1}$, and $\partial \bar{\mathbf{s}} / \partial \Delta\bar{\boldsymbol{\epsilon}}^p$ is also symmetric. Therefore \mathbf{C}^{ep} is defined by a maximum of 21 independent
489 components (being a symmetric six-by-six matrix). As such, the CTO tensor \mathbf{C}^{ep} exhibits not only the minor,
490 but also the major, symmetry – this fact traces from the symmetry of second derivatives. A characteristic
491 of variational constitutive updates, this is carefully noted in [Ortiz and Stainier \[1999\]](#) for instance.

492 Consequently the stability analysis simplifies. For detained exposition, see for example Eq. (2-15) in
493 [Borja \[2006\]](#). However in brief, consider two solutions given by

$$\text{solution (i) : } (\dot{\boldsymbol{\sigma}}, \dot{\mathbf{u}}), \quad \text{and} \quad \text{solution (ii) : } (\dot{\boldsymbol{\sigma}}^*, \dot{\mathbf{u}}^*).$$

Solution (i) is the local solution, and satisfies the mechanical equilibrium equation and boundary conditions in rate form. Presume solution (ii) also satisfies the equilibrium equation and boundary conditions in rate form. Observe our material is incrementally linear, being that:

$$\frac{\partial \mathbf{s}}{\partial \Delta \boldsymbol{\epsilon}^P} : \dot{\boldsymbol{\epsilon}}^P = \frac{\partial \mathbf{s}}{\partial \Delta \boldsymbol{\epsilon}^P} : (\dot{\boldsymbol{\epsilon}} - \dot{\boldsymbol{\epsilon}}^P) = \mathbf{C}^e : \dot{\boldsymbol{\epsilon}}^e.$$

494 where we use Eq. (1). The rate of stress is then linear in the rate of strain, per

$$\dot{\boldsymbol{\sigma}} = \mathbf{C}^e : \dot{\boldsymbol{\epsilon}}^e = \overbrace{\mathbf{C}^e : \left(\mathbf{C}^e + \frac{\partial \mathbf{s}}{\partial \Delta \boldsymbol{\epsilon}^P} \right)^{-1} : \frac{\partial \mathbf{s}}{\partial \Delta \boldsymbol{\epsilon}^P}}^{\mathbf{C}^{\text{ep}}} : \dot{\boldsymbol{\epsilon}}. \quad (42)$$

495 Hence operator \mathbf{C}^{ep} linearly relates $\dot{\boldsymbol{\sigma}}$ and $\dot{\boldsymbol{\epsilon}}$, necessitated by the definition of the CTO in Eq. (41). With
496 incremental linearity established, the local uniqueness condition (to left) coincides with the local stability
497 condition (to right):

$$\llbracket \dot{\boldsymbol{\epsilon}} \rrbracket : (\dot{\boldsymbol{\sigma}}^* - \dot{\boldsymbol{\sigma}}) > 0 \quad \text{and} \quad \text{sym}(\mathbf{C}^{\text{ep}}) = \mathbf{C}^{\text{ep}} \iff \llbracket \dot{\boldsymbol{\epsilon}} \rrbracket : \mathbf{C}^{\text{ep}} : \llbracket \dot{\boldsymbol{\epsilon}} \rrbracket > 0,$$

498 where $\llbracket \dot{\boldsymbol{\epsilon}} \rrbracket \neq \mathbf{0}$. Physically, $\llbracket \dot{\boldsymbol{\epsilon}} \rrbracket$ is interpreted physically as a jump in the strain rate $\llbracket \dot{\boldsymbol{\epsilon}} \rrbracket = \dot{\boldsymbol{\epsilon}}^* - \dot{\boldsymbol{\epsilon}}$.

499 With \mathbf{C}^{ep} super-symmetric, in that the constitutive update is variational, our evaluation of local stability
500 simplifies. In particular, we avoid the oftentimes intricate procedures to resolve the roots of a second-
501 order acoustic tensor, for elaboration cf. Mota et al. [2016]. Instead for our \mathbf{C}^{ep} super-symmetric, the local
502 uniqueness condition (to left) furthermore coincides with the determinate condition (to right):

$$\llbracket \dot{\boldsymbol{\epsilon}} \rrbracket : (\dot{\boldsymbol{\sigma}}^* - \dot{\boldsymbol{\sigma}}) > 0 \quad \text{and} \quad \text{sym}(\mathbf{C}^{\text{ep}}) = \mathbf{C}^{\text{ep}} \iff \det(\text{sym}(\mathbf{C}^{\text{ep}})) = \det(\mathbf{C}^{\text{ep}}) = 0,$$

503 where $\llbracket \dot{\boldsymbol{\epsilon}} \rrbracket \neq \mathbf{0}$ (also reference Eq. (9.4-9) in Borja [2013]).

504 Consequently, at last we motivate the immediately prior discussion on uniqueness and stability. Specif-
505 ically consider the expression for the CTO, focusing on the micromorphic contribution to the consistent
506 tangent in Eq. (41). From that equation, observe that unfortunately full rank of the local system $\partial \bar{\mathbf{s}} / \partial \Delta \bar{\boldsymbol{\epsilon}}^P$ is a
507 necessary but not sufficient condition for invertibility of the consistent tangent \mathbf{C}^{ep} . In particular for non-
508 singular \mathbf{C}^{ep} , then the tangent of the plastic back-stress in the plastic strain increment $\partial \bar{\mathbf{s}} / \partial \Delta \bar{\boldsymbol{\epsilon}}^P$ must also
509 be nonsingular.

510 Accordingly, our reason to introduce multiple micromorphic fields becomes clear. Given that the volu-
511 metric plastic strain directly controls hardening behavior, per the exponential relations Eq. (7) and Eq. (8),
512 it is immediately and physically intuitive to regularize ϵ_v through the field variable $\bar{\boldsymbol{\epsilon}}_v^P$. However from the
513 terms in the local tangent Eq. (36), for instance, observe that the volumetric field variable $\bar{\boldsymbol{\epsilon}}_v^P$ contributes
514 exactly nothing to $(\partial \bar{\mathbf{s}} / \partial \Delta \bar{\boldsymbol{\epsilon}}^P)_{ii}$ for $i \geq 4$ with $\bar{\mathbf{b}}_v \sim \bar{\mathbf{1}}$, as here.

515 *Remark 4.* In consequence, as volumetric regularization contributes only $\bar{\mathbf{b}}_v \bar{\mathbf{b}}_v^T \sim \bar{\mathbf{1}} \bar{\mathbf{1}}^T$ to $\partial \bar{\mathbf{s}} / \partial \Delta \bar{\boldsymbol{\epsilon}}^P$, we in-
516 corporate a second micromorphic field $\tilde{\boldsymbol{\lambda}}$. Our goal is to relieve rank deficiency in the shear-associated
517 sub-matrix of $\partial \bar{\mathbf{s}} / \partial \Delta \bar{\boldsymbol{\epsilon}}^P$ (furthermore, which has physical significance as the tangent of the plastic stress in
518 the increment of the plastic strain), such that $\partial \bar{\mathbf{s}} / \partial \Delta \bar{\boldsymbol{\epsilon}}^P$ and hence the CTO are nonsingular. As highlighted
519 immediately prior in this section, the determinate and uniqueness conditions coincide for $\mathbf{C}^{\text{ep}} = \text{sym}(\mathbf{C}^{\text{ep}})$.
520 Thus by adding the second field $\tilde{\boldsymbol{\lambda}}$, we extend the well-posedness of certain boundary value problems, for
521 instance during strain localization. Hence our purpose in regularizing the equivalent plastic strain differs
522 from the gradient-dependent MCC model in Stankiewicz and Pamin [2006], for instance, who attribute
523 benefit from λ -regularization to their $\lambda \in \mathbb{R}^+ \cup \{0\}$ and $\dot{\lambda} \geq 0$, in comparison to the plastic strain's trace
524 which, as emphasized in Stankiewicz and Pamin [2006], may decrease.

5.1 Micromorphic regularization as remedy for volume locking

As pointed out in Sun [2015], Sun et al. [2013] and recently in Abboud and Scovazzi [2018], volume locking may occur in low-order finite element when volume-preserving plastic flow occurs. While selective integration or assume strain formulation may overcome the locking, these treatments must be used with stabilized formulation or hourglass control to prevent spurious spatial oscillation [Chen et al., 2002, Choo and Lee, 2018, Liu et al., 2016, Reese and Wriggers, 2000].

In essence, the regularization provided by the gradient-dependent diffusive functional Eq. (13) is both an effective localization limiter, penalizing the difference between the local plastic strain ϵ_v^p and the assumed strain $\tilde{\epsilon}_v^p$ regularized via a Helmholtz equation, as well as a stabilization term. In other words, the avoidance of locking is attributable to: undesirable over-sampling of volumetric sampling points for numerical integration in low-order finite elements overcome by the Laplacian operator in the Helmholtz equation. The regularization method constrains the spatial fluctuation of the both the local plastic strain ϵ_v^p and the assumed strain $\tilde{\epsilon}_v^p$ (provided that the length scale parameter $\tilde{l}_v = l_v \sqrt{K_v/k_v}$ is sufficiently large relative to the mesh size).

In that two micromorphic variables are introduced, note that effects of $\tilde{\lambda}$ scale with k_λ . In the next section, our numerical experiments are converged through sequenced strain localization events using (relatively) small values of k_λ , as compared to a_λ and hence to the volumetric a_v . While a complete mathematical analysis is out of the scope of this paper (but will be considered in the future), interested readers may refer to the assumed deformation gradient formulation in Section 3 of Sun et al. [2013] for a similar strategy applied to volume-preserving poroelasticity problems.

6 Numerical Examples

We present two sets of boundary value problems, testing the proposed model's capability to replicate size-dependent anisotropy, and examining the effects of anisotropy across different length scales on formation of deformation bands, at various initial consolidation states. The first set of simulations represents 2D plane strain compression, with the anisotropic numerical specimen oriented such that every structural direction, such as microstructural vector l , is in-plane. In contrast, the 3D simulations are designed to showcase 3D anisotropic responses in drained triaxial compression tests.

Unless otherwise specified, we assign dimensions on diagrams in mm and approximate the elastic parameter μ_l using Eq. (46). For materials that exhibit a plastically isotropic response, we set $\mathbf{b}_v = \mathbf{1}$, and

$$\overbrace{\alpha^{\text{dev}} = \beta^{\text{dev}} = \gamma^{\text{dev}} = \alpha^{\text{vol}} = \beta^{\text{vol}} = \gamma^{\text{vol}} = 1,}^{\text{purely local coefficients}} \quad \overbrace{\phi_\lambda = \chi_\lambda = \phi_v = \chi_v = 0.}^{\text{micromorphic coefficients}} \quad (43)$$

For $\mathbf{b}_v = \mathbf{1}$ and $\mathbf{P}^{\text{p vol}} = \mathbf{I}$, this implies $\mathbf{b}_v = \mathbf{P}^{\text{p vol}^{-1}} : \mathbf{1} = \mathbf{1}$ (cf. Appendix C).

To capture the growth of micromorphic field variables' boundary layer, the length scale must be sufficiently larger than the mesh size. Furthermore, in the numerical examples presented in this section, the micromorphic material parameters are identified by introducing the following assumptions to simplify the calibration procedure. First, we assume that $\tilde{l}_\lambda = \tilde{l}_v$ per Eq. (33). This treatment implies that $k_\lambda = K_\lambda$ and $k_v = K_v$, unless otherwise noted. In turn, K_λ and K_v are parameterized by a_λ and a_v , as given by Eq. (14). Unless otherwise noted, the local direction vector l is equal to $l_\lambda = l_v$. The displacement prescribed in the boundary leads to compression in the axial direction.

Table 1: Anisotropy rubric

	micromorphic isotropy	micromorphic anisotropy
local isotropy	LI-MI	LI-MA
local anisotropy	LA-MI	LA-MA

560 Anisotropy of the local material response vs. anisotropy associated with the micromorphic field vari-
 561 ables' diffusivity tensors is categorized by the rubric in Table 1. The table's entries are used to classify our
 562 numerical examples and parameterizations thereof.

563 6.1 2D plane strain compression

564 The geometry of the plane strain test is presented in Fig. 4(a). This figure represents uniaxial compression
 565 with a uniform, compressive, and normal confining stress σ_c applied at the lateral boundaries. The material
 566 initial state is specified by the over-consolidation ratio (OCR). For the highly overconsolidated simulations,
 567 $\text{OCR} = 30$ and $p_{c0} = -30$ MPa, implying $\sigma_c = -1$ MPa. For simulations performed on a normally
 568 consolidated numerical specimen, we set p_{c0} to be -30 MPa, hence $\sigma_c = -30$ MPa. The loading increment
 569 along the displacement-controlled boundary is $\Delta u_2 = -5.0 \times 10^{-6}$ mm downwards.

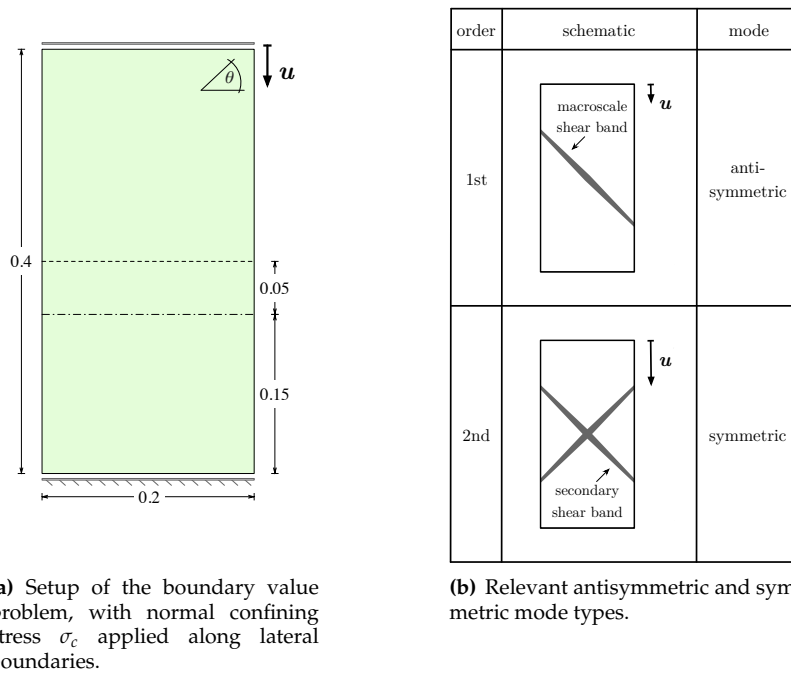


Fig. 4: Geometry of the numerical specimen for plane strain plasticity simulations, showing: (a) the sampled transects as a dashed line and a dot-dashed line; and, (b) bifurcation modal schematic abridged from the interpretation of Ikeda et al. [2003].

570 The local material parameters loosely coordinate with the calibrated parameters for the Tournemire
 571 shale specimen (cf. Appendix E). Due to the introduction of anisotropy from the micromorphic regulariza-
 572 tion, the material parameters are adjusted to distinguish the material-point and mesoscale anisotropies as
 573 follows. The elastic response is characterized by the Young's modulus and Poisson ratio $E = E_l = 14000$
 574 MPa and $\nu = \nu_l = 0.20$. Microstructural direction l and the eigenvectors of the micromorphic diffusivities
 575 are varied in the numerical examples to examine the anisotropic responses.

576 The slope of the critical state line in the fictitious isotropic stress-space and the modified compression
 577 index are $M = 1.2$ and $C_d = 0.005$ accordingly. Anisotropic plasticity material parameters are labeled
 578 in the parametric studies. In general, in this section, the local and micromorphic material parameters are
 579 not varied simultaneously, such that their respective influence can be individuated. Micromorphic length
 580 scales are $\tilde{l}_\lambda = \tilde{l}_v = 0.005$ mm, whereas $K_\lambda = a_\lambda \times 10^{-2}$, and $K_v = a_v$. Heuristically from the numerical

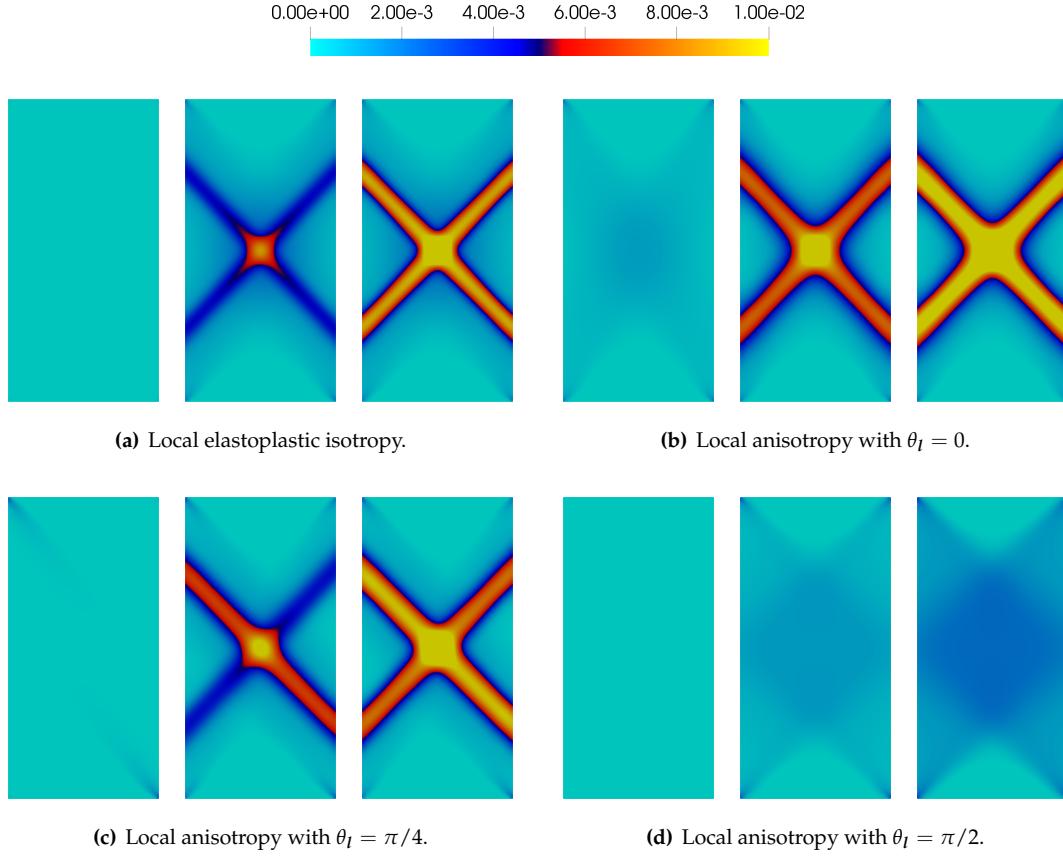


Fig. 5: Equivalent plastic strain λ for plane strain compression isotropic case vs. anisotropic cases with $\text{OCR} = 30$ and rotation of microstructural direction, inducing local anisotropy in (b-d) by setting $E = 2400$ MPa and $\beta^{\text{dev}} = \beta^{\text{vol}} = 0.8$, at $u_2 = -0.4, -0.8, -1.0 \times 10^{-3}$ mm (LA-MI, see Table 1 for classification).

581 simulations we ran, K_λ/k_λ and K_v/k_v must be sufficiently small such that the numerical boundary value
 582 problem remains solvable.

583 The initial mesh is conformal with the geometry in Fig. 4(a). The rectangular quadrilateral cells in each
 584 row number 7, and the elements in each column number 15, totaling $n_0 = 105$ elements in the initial mesh.
 585 Each additional level of refinement equally partitions every cell at the previous level of refinement into
 586 four cells (in 2D). Therefore, the refined mesh contains $n_0 \times 4^{l_h}$ cells for l_h levels of refinement. For all
 587 simulations excluding the mesh refinement study, $l_h = 3$.

588 At a high OCR, local anisotropy induces staggered antisymmetric and subsequent symmetric strain
 589 localization. The localization modes are characterized in Fig. 4(b). Fig. 5 evidences the model's numeri-
 590 cal recovery of these modes. Fig. 5(a) show the response of the numerical specimen composed of an
 591 isotropic material with symmetric loading. Hence, only the symmetric localization modes are recovered
 592 in the numerical simulations. For the case where the microstructural angle $\theta_l = 0$ in Fig. 5(b), the material
 593 is anisotropic but the local microstructural direction coincides with the normal vector describing a plane
 594 of loading symmetry. In this case, only symmetric shear bands form. On the contrary, in the case where
 595 $\theta_l = \pi/4$ in Fig. 5(c), the microstructural direction misaligns with the loading's symmetry. An antisym-
 596 metric mode localizes at $u_2 = -0.8 \times 10^{-3}$ mm, preceding the secondary symmetric mode at 1.0×10^{-3}
 597 mm.

588 In two important scenarios, strain localization is effectively suppressed due to the change of the orien-
 599 tation of the numerical specimen. In the case shown in Fig. 5(d), the orientation of the transversely isotropic
 600 plane at $\theta_i = \pi/2$ leads to reduction of compliance in the loading direction and therefore stanches strain

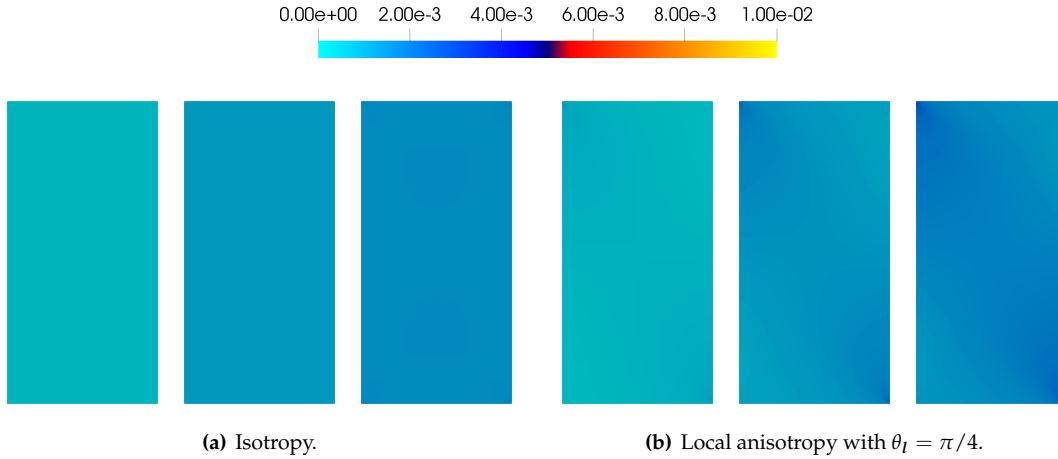


Fig. 6: Equivalent plastic strain λ for comparison of isotropic vs. anisotropic plane strain compression cases with OCR = 1 and hence normal consolidation, inducing local anisotropy in (b) by setting $E = 2400$ MPa and $\beta^{\text{dev}} = \beta^{\text{vol}} = 0.8$, at $u_2 = -0.4, -0.8, -1.0 \times 10^{-3}$ mm (LA-MI).

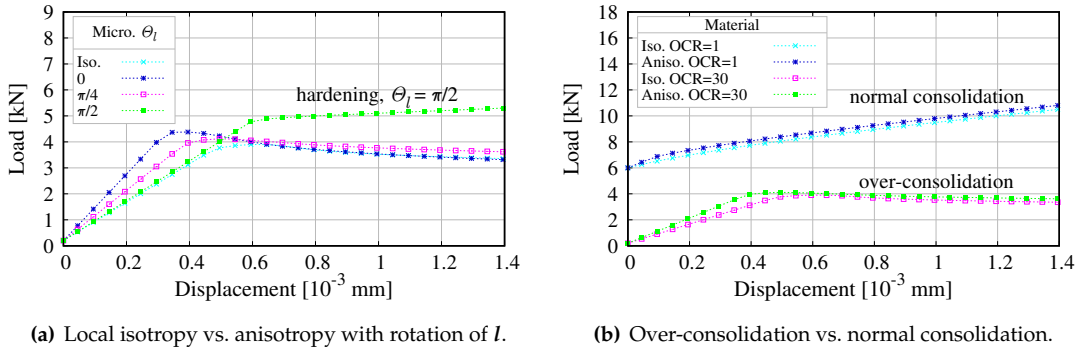


Fig. 7: Plane strain compression case with isotropy and anisotropy comparisons, vertical force vs. vertical displacement curves, showing: (a) isotropic case vs. anisotropic cases with increasing microstructural angle θ_l ; and, (b) isotropy vs. anisotropy with $\theta_l = \pi/4$ at two over-consolidation ratios (OCR) (LA-MI).

601 localization. On the other hand, the plastic strain is diffusive at lower OCR, as shown in Fig. 6. This is
 602 achieved by lowering the OCR, hence σ_c to -30 MPa. The evidence showcased in this parametric study in-
 603 dicates that the plastic flow and hardening can both be affected by (1) rotating the microstructural direction
 604 and/or (2) increasing lateral compression. Different material orientations leading to different constitutive
 605 responses indicates that the anisotropy of the material is captured.

606 Hardening is captured quantitatively in Fig. 7(a) and Fig. 7(b), corresponding respectively to l -rotation
 607 and diminishing σ_c . We compare global body-averaged values for the material state, Fig. 8 and Fig. 9. The
 608 regularized model captures phase change induced by local material anisotropy and/or degree of initial
 609 consolidation. Most notably, in Fig. 8, rotation of the microstructural direction itself induces phase change
 610 l . In particular, for microstructural angle $\theta_l = \pi/2$, the deformation remains both diffusive and compactive.
 611 Similarly, for normal consolidation with OCR = 1 in Fig. 9, p^* grows monotonically more compressive with
 612 decreasing ϵ_v . Absent significant localization, the global $-p_c$ vs. ϵ_v semilog curves recover approximately
 613 the gradient implied by Eq. (7).

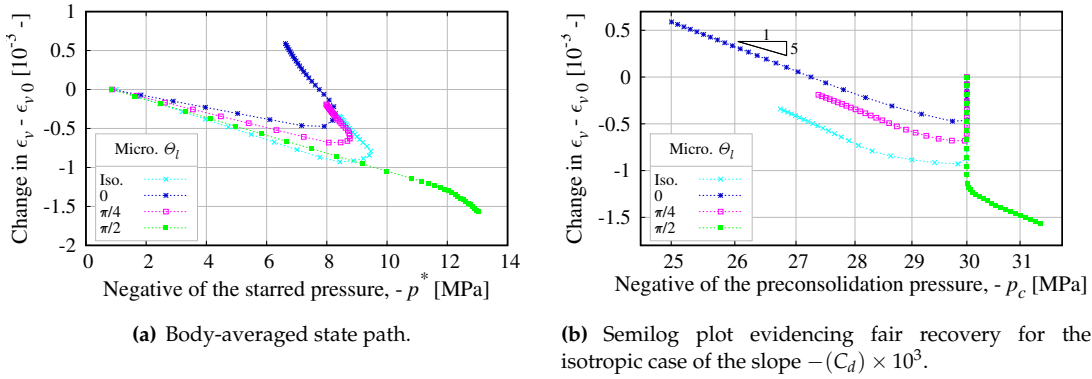


Fig. 8: Plane strain compression case comparing local isotropy and anisotropy with increasing microstructural angle θ_l , globally averaged material state curves, showing: (a) and (b), loading paths for change in ϵ_v , such that loading paths begin at 0 in the ordinate axis (LA-MI).

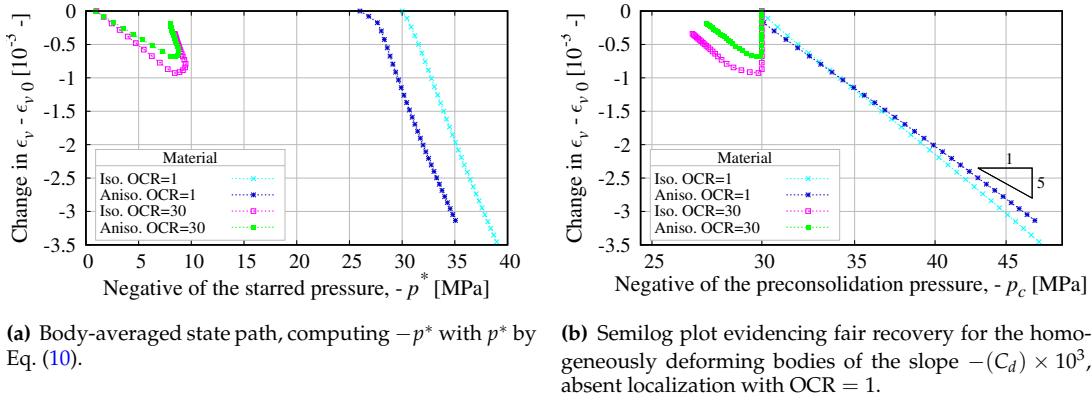


Fig. 9: Plane strain compression case comparing local isotropy and anisotropy with microstructural angle $\theta_l = \pi/4$ at two over-consolidation ratios (OCR), globally averaged material state curves, showing: (a) and (b), loading paths for change in ϵ_v , such that loading paths begin at 0 in the ordinate axis. Note that cases labeled OCR = 30 correspond to Fig. 5(a-b) and OCR = 1 to Fig. 6(a-b) (LA-MI).

6.1.1 Diffusive anisotropy study

In this parametric study, we does not introduce anisotropy in the local material parameters, i.e. the classical MCC is used in the local constitutive update. Instead, we introduce anisotropy in the diffusion term of the Helmholtz equation. The resultant gradient-dependent plastic flow induces anisotropy. As such, both the plastic flow and the consequent strain localization can be manipulated by the diffusive field mapping in Eq. (15).

Micromorphic anisotropy alters both the bifurcation modes and the persistent shear band (the dominant pattern of the localized deformation [Wang et al., 2016]). Fig. 10 demonstrates the distribution of the equivalent plastic strain in the numerical specimen. Specifically, increasing $\phi_v > 0$ induces an antisymmetric localization mode parallel to diffusivity's eigenvector direction l_v ; compare Fig. 10(a) to Fig. 10(b).

Previous studies have considered this effect, Forest [2016] for instance. However, our examples' parameterization highlights two inter-linked consequences. The micromorphic diffusivity's anisotropy promotes both antisymmetric strain banding (cf. Fig. 4(b)), and also rotation of the plastic strain's eigenvector direction. Notably this parameterization's the local material parameters are isotropic, such that practically the

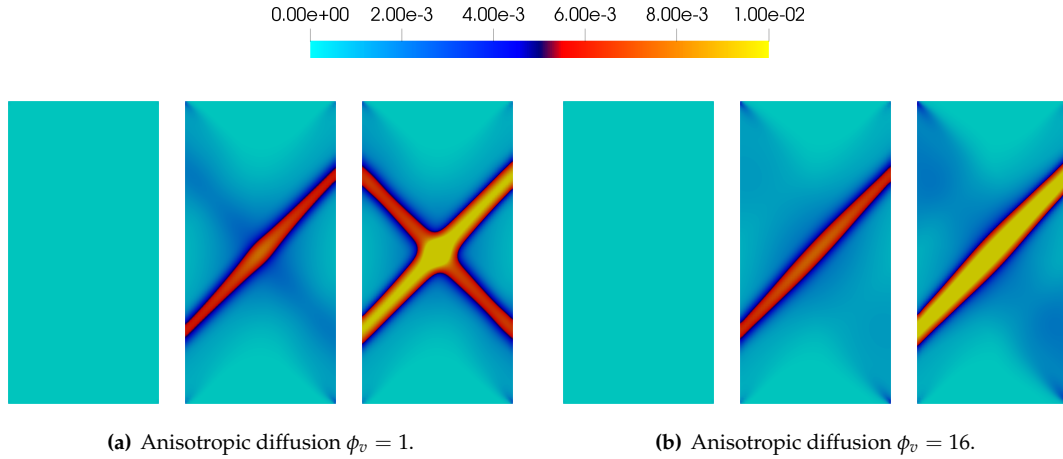


Fig. 10: Equivalent plastic strain λ for diffusively anisotropic plane strain compression case, with I_v described by $\theta_v = \pi/4$, at $u_2 = -0.4, -0.8, -1.0 \times 10^{-3}$ mm.

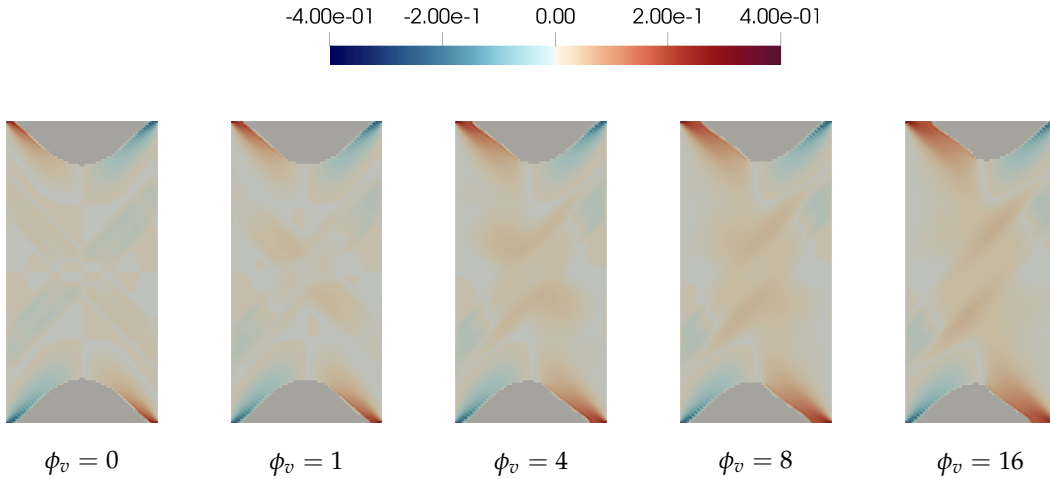


Fig. 11: Angle from horizontal of plastic strain's eigenvector corresponding to its greatest (most dilative) in-plane eigenvalue (in radians), for diffusively anisotropic plane strain compression case, with I_v described by $\theta_v = \pi/4$, at $u_2 = -1.0 \times 10^{-3}$ mm. Regions where $\epsilon^P = \mathbf{0}$ are grayed-out (LI-MA).

628 model reduces to the isotropic two-invariant minimization of Ortiz and Pandolfi [2004]. Nonetheless the
 629 mesoscale material response is clearly anisotropic. Clearly, the orientation of the plastic strain's direction
 630 changes with the increasingly anisotropic diffusivity tensor, per Fig. 11.

631 In that the mesoscale plastic deformation is anisotropic, the band's antisymmetry exacerbated by in-
 632 creasing ϕ_v . Parameter ϕ_v controls the anisotropy of the diffusivity tensor, and changes from 0 (the isotropic
 633 case) to 16. In Fig. 11, this parameter is shown to control rotations of the plastic strain direction. Changing
 634 the principal direction indicates that the anisotropic regularization alone is sufficient to induce a globally
 635 anisotropic responses in the numerical specimen. Yet, such a change in the plastic flow direction does not
 636 require the introduction of a nonassociative plastic potential.

637 In contrast to ϕ_v , increasing χ_v in Fig. 12(b) engenders much the same bifurcation mode as local
 638 anisotropy in Fig. 5(c). As measured by the reaction force in Fig. 12(a), for these cases, the micromorphic
 639 anisotropy insignificantly affects the force-displacement curves. Yet, the anisotropy in the diffusion term
 640 nonetheless imposes noticeable influence on the spatial distribution of equivalent plastic strain as shown in

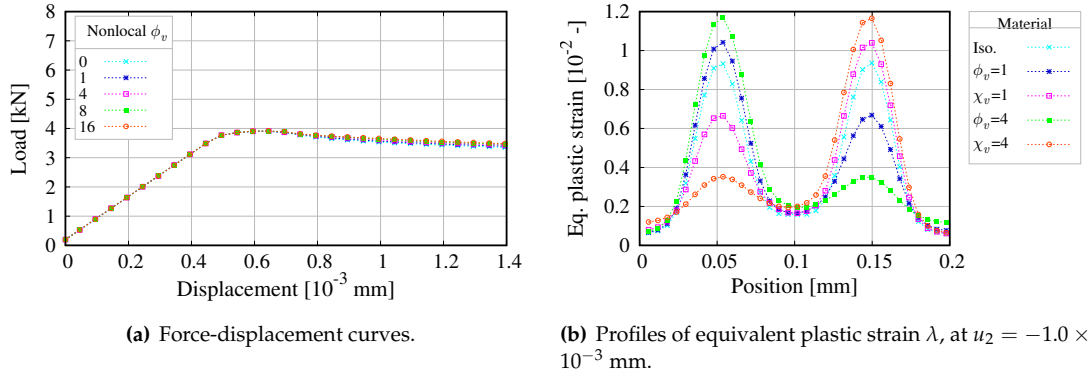


Fig. 12: Diffusively anisotropic plane strain compression case, showing: (a) vertical force vs. vertical displacement curves with increasing anisotropic diffusion ϕ_v ; and, (b) profiles of equivalent plastic strain λ across transect indicated as a dot-dashed line in Fig. 4(a) (LI-MA).

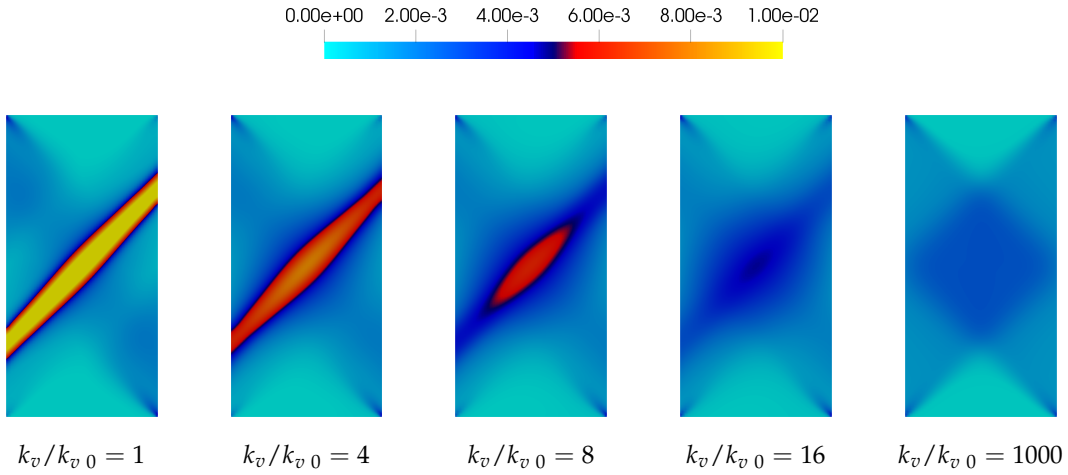


Fig. 13: Equivalent plastic strain λ for diffusively anisotropic plane strain compression case, with $\phi_v = 16$ and I_v described by $\theta_v = \pi/4$, at $u_2 = -1.0 \times 10^{-3}$ mm (LI-MA).

641 Fig. 12(b). This combination indicates that the diffusivity can help to calibrate the macroscopic localization
 642 pattern, independent of the reaction forces.

643 To analyze whether micromorphic material parameters can be identified from inverse problems such
 644 that the resultant material laws can replicate the plastic deformation and pattern of strain localization con-
 645 sistent with observations, we conduct additional simulations with different values for the micromorphic
 646 material parameter k_v . Recall that increasing this material parameter will make any discrepancy between
 647 the local plastic volumetric strain ϵ_v^p measure and the field value $\tilde{\epsilon}_v^p$ costs more energy. Therefore, as the
 648 value of k_v increases, the influence of the anisotropic responses also increase such that (1) the resultant
 649 plastic strain becomes more diffusive and (2) the principal direction of the plastic strain rotates in response
 650 to the anisotropy induced by the diffusivity tensor, as shown in Figs. 13 and 14.

651 This point merits further numerical investigation regarding macroscopic strain-hardening, as well. In
 652 Figs. 15 and 16, the relaxation stiffnesses k_λ and k_v are simultaneously increased over the baseline values.
 653 The plastic deformation phases changes to hardening, with no remainder strain localization, at the maxi-
 654 mum tested k_λ . Under consideration of Eq. (13), we observe that penalization of differences between the
 655 local internal variables vs. the micromorphic field reorients the plastic strain direction, most noticeably
 656 away from the fixed-displacement boundaries.

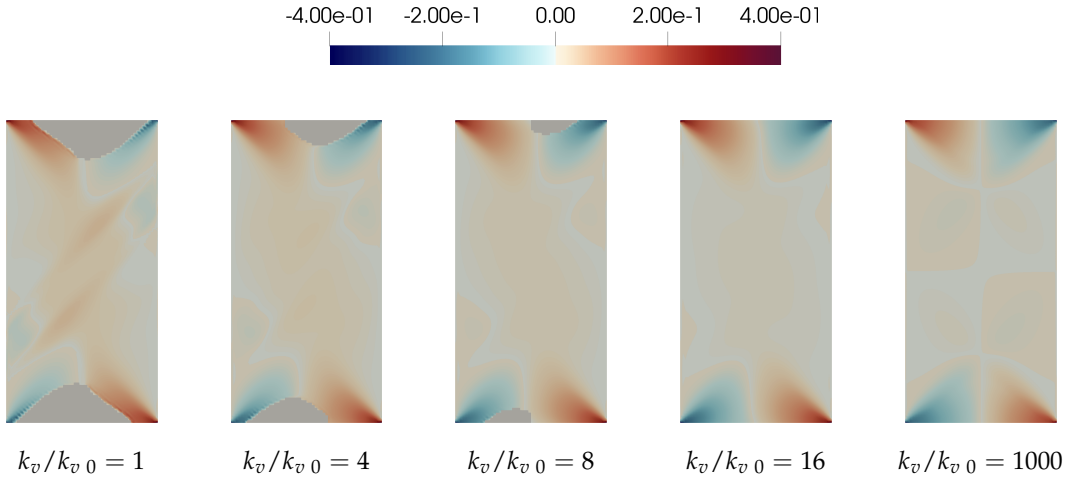


Fig. 14: Angle from horizontal of plastic strain's eigenvector corresponding to its greatest (most dilative) in-plane eigenvalue (in radians), for diffusively anisotropic plane strain compression case, with $\phi_v = 16$ and I_v described by $\theta_v = \pi/4$, at $u_2 = -1.0 \times 10^{-3}$ mm. Regions where $\epsilon^P = \mathbf{0}$ are grayed-out (LI-MA).

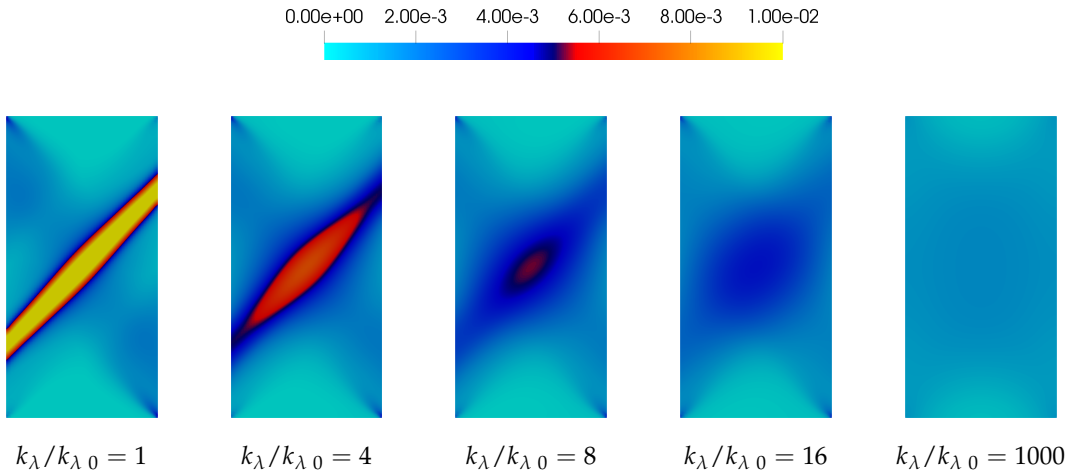


Fig. 15: Equivalent plastic strain λ for diffusively anisotropic plane strain compression case, with $\phi_v = 16$ and I_v described by $\theta_v = \pi/4$, at $u_2 = -1.0 \times 10^{-3}$ mm. Labeled by $k_\lambda/k_{\lambda0}$, however this parameterization holds $k_\lambda/k_{\lambda0} = k_v/k_{v0}$ (LI-MA).

657 The reaction forces for parameterizations of the penalty stiffnesses, Fig. 17, concur with our attribu-
 658 tion of phase change due to increasing k_λ . Overall, increasing the equivalent plastic strain λ -associated
 659 relaxation stiffens is observed to yield macroscopic plastic strain patterns similar to normal consolidation.
 660 Moreover, the equivalent plastic strain distributes essentially evenly across the body.

6.1.2 Mesh refinement study

662 For the mesh refinement study, the number of the additional mesh refinement levels $l_h \neq 3$. Fig. 18 depicts
 663 convergence toward mesh independent behavior, attributable to the micromorphic regularization. For a
 664 relatively large characteristic element length h with $l_h = 1$ as in Fig. 18(a), the mesh is simply too coarse to
 665 resolve the regularizing field variable's gradient. For $l_h \geq 3$ in Fig. 18(b-c), the gradient profile is sufficiently
 666 resolved. As a consequence for $l_h \geq 3$, the boundary force-displacement curves overlap during softening

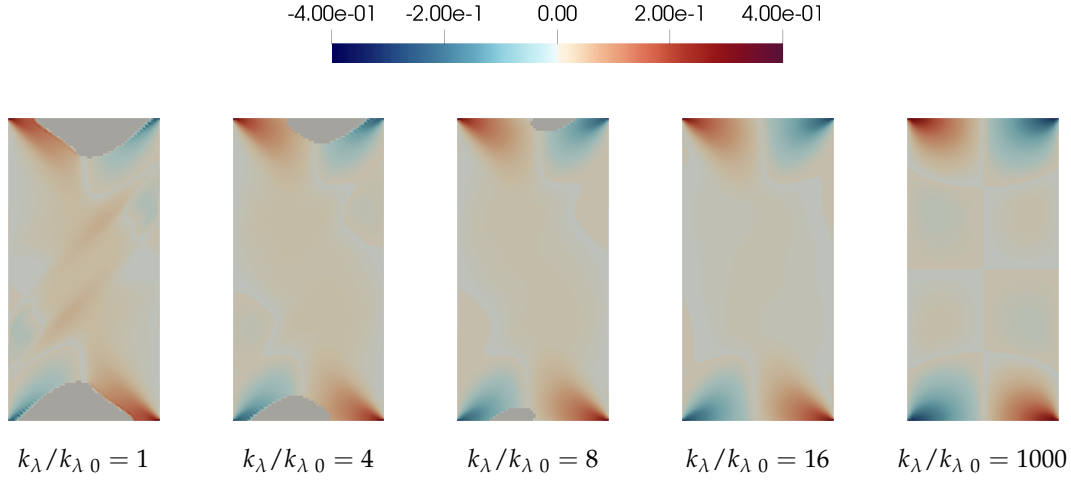
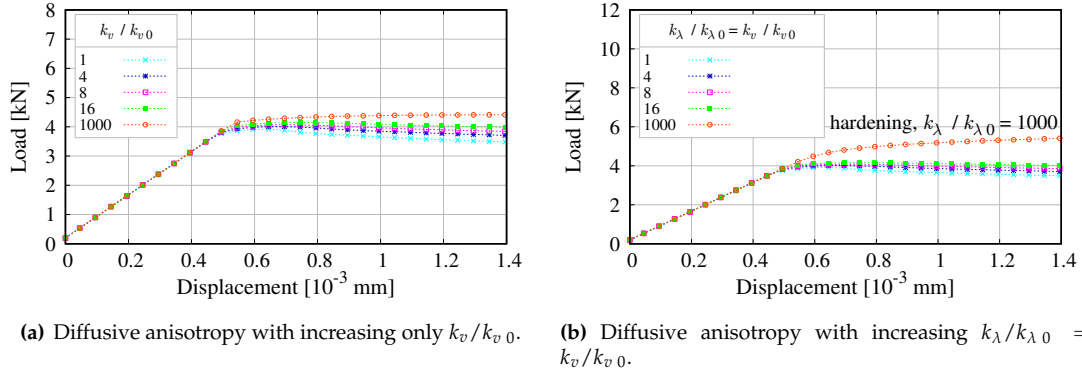


Fig. 16: Angle from horizontal of plastic strain's eigenvector corresponding to its greatest (most dilative) in-plane eigenvalue (in radians), for diffusively anisotropic plane strain compression case, with $\phi_v = 16$ and I_v described by $\theta_v = \pi/4$, at $u_2 = -1.0 \times 10^{-3}$ mm. Labeled by $k_\lambda/k_{\lambda 0}$, however this parameterization holds $k_\lambda/k_{\lambda 0} = k_v/k_{v 0}$. Regions where $\epsilon^P = 0$ are grayed-out (LI-MA).



(a) Diffusive anisotropy with increasing only $k_v/k_{v 0}$.

(b) Diffusive anisotropy with increasing $k_\lambda/k_{\lambda 0} = k_v/k_{v 0}$.

Fig. 17: Plane strain compression case with increasing penalty stiffness, vertical force vs. vertical displacement curves, showing: (a) $\phi_v = 16$ and varying $k_v/k_{v 0}$ only; and, (b) $\phi_v = 16$ and varying $k_\lambda/k_{\lambda 0} = k_v/k_{v 0}$ (LI-MA).

per Fig. 19(a). Also across the transects in Fig. 19(b), differences between the local λ 's maximal and minimal values significantly reduce for increasing l_h .

Convergence of the boundary forces with increasing mesh refinement prove to be a good proxy for convergence of the globally averaged material state, Fig. 20(a). Two trends merit further discussion. First as l_h increases, both p_c and p^* converge simultaneously, during the material softening phase postceding the elastic deformation, labeled on Fig. 20(a) and clear in Fig. 20(b). Second, convergence during plastic deformation coincides with sharpening symmetric mode shear bands; compare to the profile of equivalent plastic strain λ in Fig. 19(b) for $l_h \geq 3$.

Lastly, certain meshes are too coarse and poorly capture localization, e.g. refinement level $l_h \leq 1$, see Fig. 18(a). Conversely, these coarse meshes exhibit diffuse softening, and therefore the globally averaged ϵ_v vs. $-p_c$ semilog curves approach the slope predicted by the local hardening rule in Eq. (7). In particular, $l_h = 0$ is associated with a purely concave equivalent plastic strain λ profile in Fig. 19(b). In our case however, due to the micromorphic regularization, increased mesh refinement facilitates resolving the shear bands, along with convergence of the global state path and boundary force.

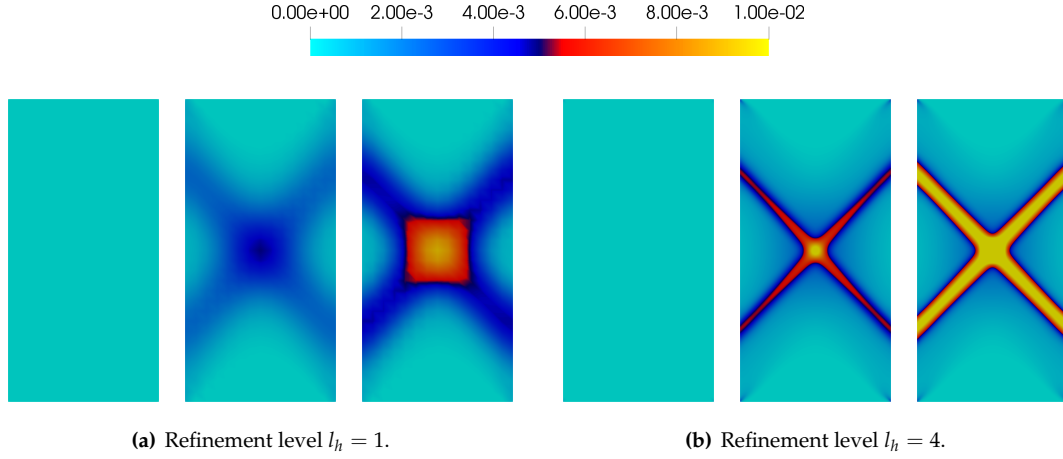


Fig. 18: Equivalent plastic strain λ for isotropic plane strain compression case with mesh refinement, at $u_2 = -0.4, -0.8, -1.0 \times 10^{-3}$ mm (LI-MI).

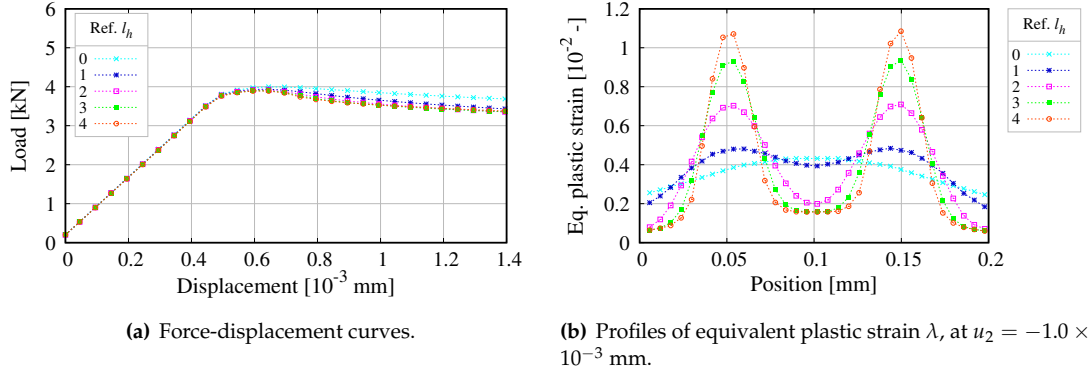


Fig. 19: Isotropic plane strain compression case with mesh refinement, showing: (a) vertical force vs. vertical displacement curves, with visually overlapping curves for additional refinement levels $l_h = 3$ and $l_h = 4$; and, (b) profiles of equivalent plastic strain λ across transect indicated as a dashed line in Fig. 4(a). Note that cases for the refinement levels $l_h = 1, 4$ correspond to Fig. 18 (LI-MA).

681 Figs. 18-20 and the mesh refinement study are treated as a baseline for the diffusive anisotropy. For
 682 the isotropic baseline cases, the normalization Eq. (33) describes an approximate maximum for the mesh
 683 characteristic length. Subsequently, inducing micromorphic anisotropy, any $\phi_\lambda > 0$ or $\chi_\lambda > 0$ guarantee
 684 out-diffusion of the field variable $\tilde{\lambda}$. Hence inevitably, by dint of this parameterization, we sufficiently
 685 resolve the regularizing field's gradient. The same holds for $\tilde{\epsilon}_v^p$, see Eq. (15).

686 6.1.3 Miromorphic stiffness study

687 Thus far in Section 6.1, shear bands develop within the simulated domain, while retaining numerical sta-
 688 bility, at the rate-independent limit. In this subsection, we show the credit for this combination accrues to
 689 the pressure-dimensioned coefficients in Eq. (14). Viz., nonlocal equivalent plastic strain $\tilde{\lambda}$'s miromorphic
 690 stiffness was a small but workable value, $K_\lambda = a_\lambda \times 10^{-2}$. In contrast, the nonlocal trace $\tilde{\epsilon}_v^p$'s stiffness was
 691 relatively greater, with $K_v = a_v$. Given that the prior examples' $K_v \gg K_\lambda$, their diffusive regularization
 692 was principally imparted by the trace-like field variable $\tilde{\epsilon}_v^p$. This was key to the successful regularization,
 693 unlike the below examples.

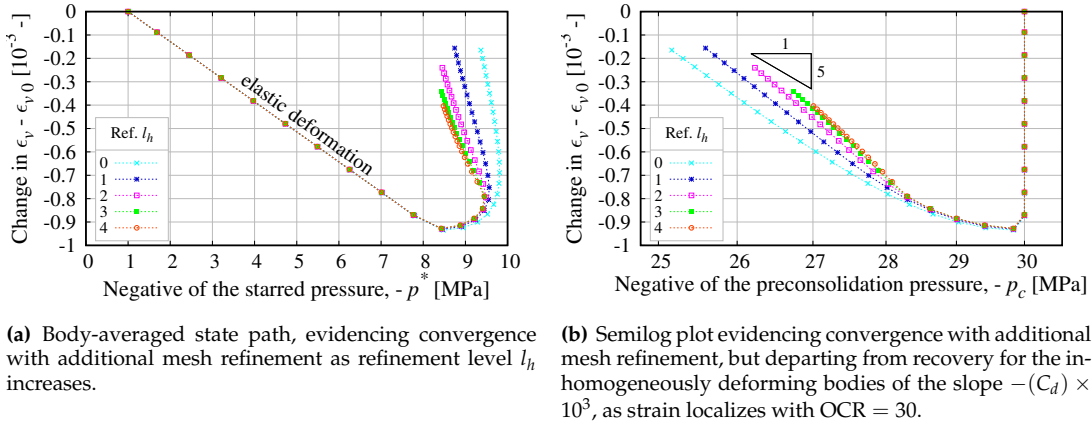


Fig. 20: Isotropic plane strain compression case with mesh refinement, globally averaged material state curves, showing: (a) and (b), loading paths for change in ϵ_v , such that loading paths begin at 0 in the ordinate axis. Note that cases for the refinement levels $l_h = 1, 2, 3, 4$ correspond to Fig. 18(a-d) (LI-MA).

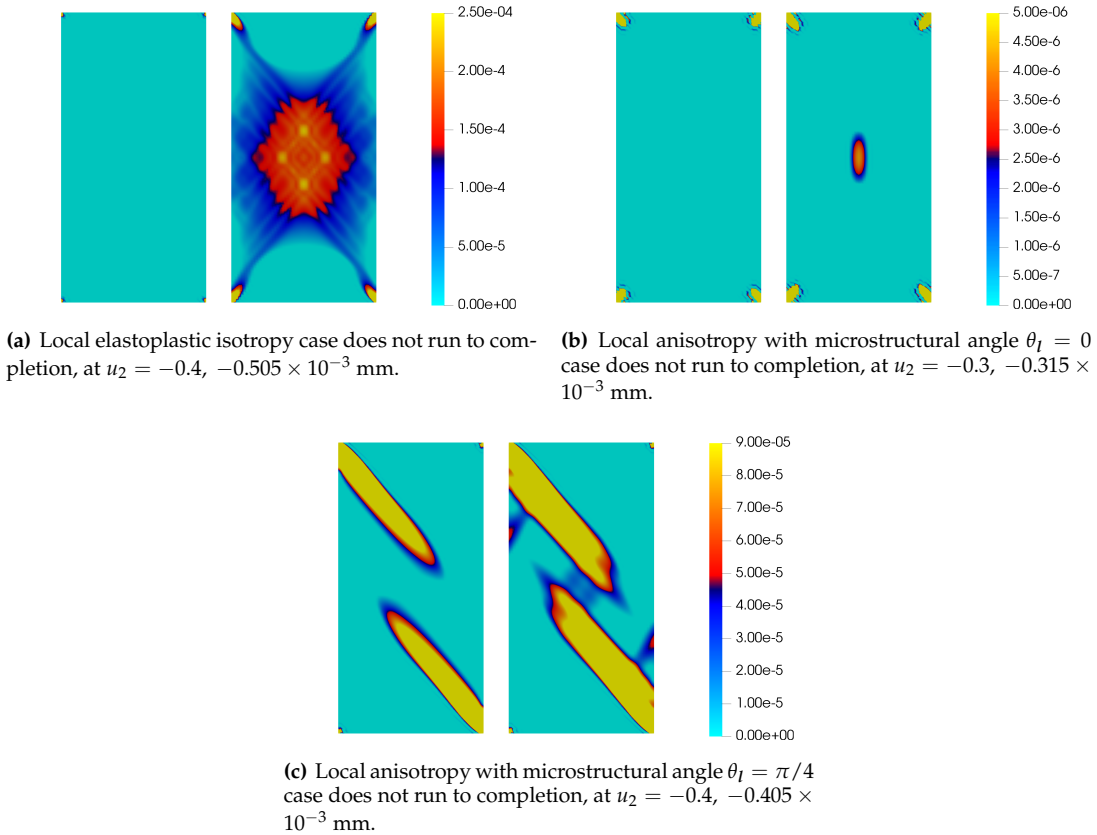
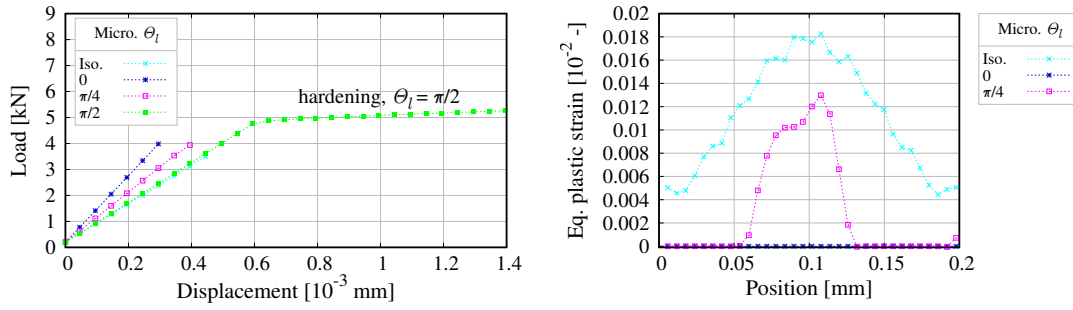


Fig. 21: Equivalent plastic strain λ for plane strain compression isotropic case vs. anisotropic cases with $\text{OCR} = 30$ and rotation of microstructural direction, but with lowered micromorphic stiffness $K_v = a_v \times 10^{-10} \approx 0$ MPa.

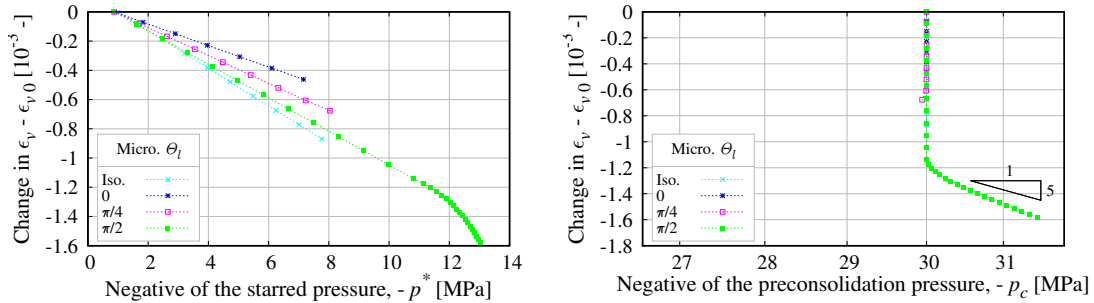


(a) Force-displacement curves, indicating only the anisotropic macroscopic hardening case with microstructural angle $\theta_l = \pi/2$ completes.

(b) Profiles of equivalent plastic strain λ , for boundary displacements u_2 at failure indicated in captions to Fig. 21.

Fig. 22: Plane strain compression case comparing local isotropy and anisotropy with micromorphic stiffness $K_v \approx 0$ MPa, showing: (a) vertical force vs. vertical displacement curves; and, (b) profiles of equivalent plastic strain λ across transect indicated as a dashed line in Fig. 4(a) (LA-MI).

694 Instead consider the converse scenario: micromorphic stiffness K_v goes to a small value; consequently
 695 the trace field variable $\tilde{\epsilon}_v^p$ exerts negligible effect; and, direct regularization of the plastic hardening is
 696 effectively discontinued. Specifically, all other parameters are held equal, $\tilde{\epsilon}_v^p$'s micromorphic stiffness is
 697 dropped to $K_v = a_v \times 10^{-10}$. Given that $k_v = K_v \approx 0$ MPa, the volumetric penalty term remains small in
 698 Eq. (13), even for large differences between local internal variable ϵ_v and field variable $\tilde{\epsilon}_v^p$. Thus, the model
 699 becomes almost purely local, w.r.t. direct hardening regularization.



(a) Body-averaged state path, indicating only the anisotropic case with microstructural angle $\theta_l = \pi/2$ completes.

(b) Semilog plot evidencing fair recovery for the hardening case of the slope $-(C_d) \times 10^3$, with all softening cases failing to complete.

Fig. 23: Plane strain compression case comparing local isotropy and anisotropy with micromorphic stiffness $K_v \approx 0$ MPa, globally averaged material state curves, showing: (a) and (b), loading paths for change in ϵ_v , such that loading paths begin at 0 in the ordinate axis. Neither the isotropic case nor the anisotropic cases with microstructural angles $\theta_l = 0, \pi/4$ run to completion (LA-MI).

700 In this first scenario, the numerical boundary value problems exhibit conditional instability. Fig. 21(a-c)
 701 depicts this phenomenon, which is measured in Fig. 22(d): conditionally, based upon the microstructural
 702 angle θ_l , in that most simulations in Fig. 21 fail to converge through localized softening. In the same vein in
 703 Fig. 22(b), oscillatory equivalent plastic strain λ profiles correspond to the non-convergent cases, evidenc-
 704 ing divergence upon localization. Hence, for practical purposes, diminishing K_v stymies the appearance of
 705 regularized shear band-like strain localization phenomena.

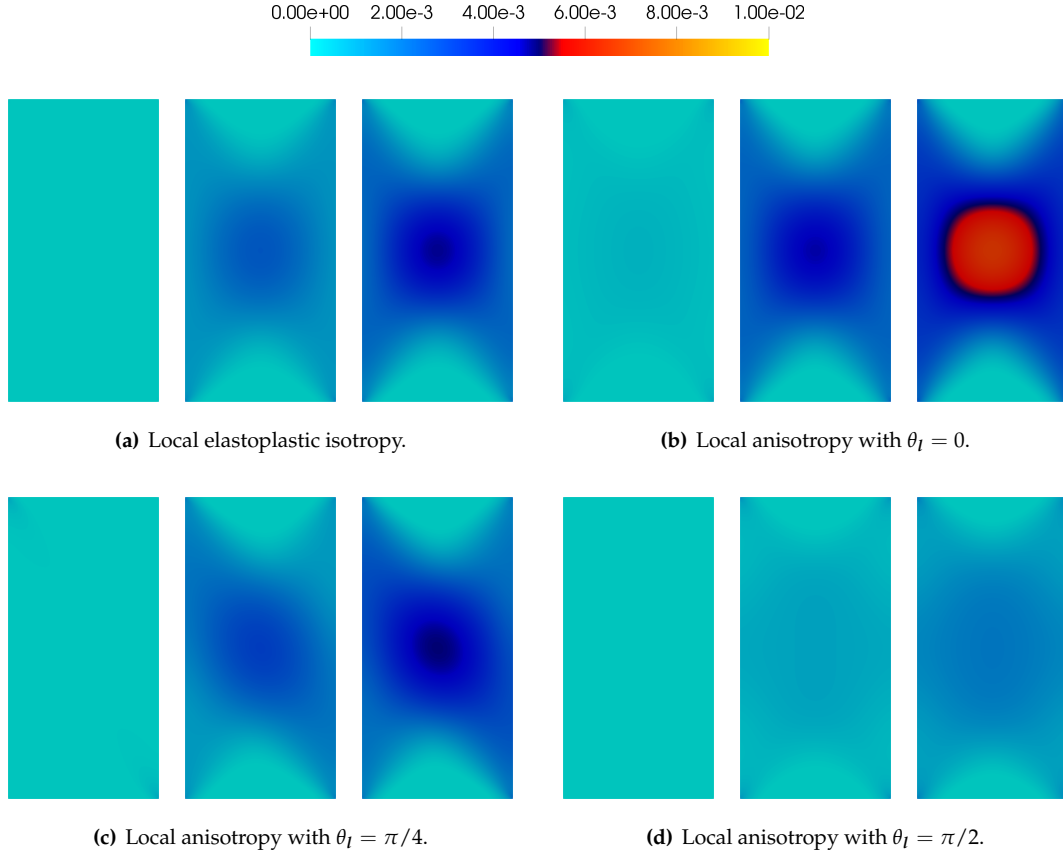


Fig. 24: Equivalent plastic strain λ for plane strain compression isotropic case vs. anisotropic cases with $\text{OCR} = 30$ and rotation of microstructural direction, but with reversed nonlocal stiffnesses $K_\lambda = a_\lambda$ and $K_v = a_v \times 10^{-2}$, at $u_2 = -0.4, -0.8, -1.0 \times 10^{-3}$ mm (LA-MI).

706 Alternatively, under-weighting the trace-like $\tilde{\epsilon}_v^p$ may inhibit strain localization. Specifically, shear bands
 707 are also stifled by the ultimate parameterization: the coefficients applied to compute the micromorphic
 708 stiffness are reversed. Rather than $K_\lambda = a_\lambda \times 10^{-2}$ and $K_v = a_v$ as in Fig. 5, we apply instead $K_\lambda = a_\lambda$ and
 709 $K_v = a_v \times 10^{-2}$ in Fig. 24. Due to this change, the shear bands are suppressed for all microstructural angles
 710 θ_I .

Table 2: Micromorphic regularization stiffness and convergence summary

\tilde{l}_λ [mm]	a_λ [MPa]	k_λ [MPa]	K_λ [MPa]	k_v [MPa]	K_v [MPa]	softening	localization
\tilde{l}_v	a_v	$a_\lambda \times 10^{-2}$	$a_\lambda \times 10^{-2}$	a_v	a_v	stable	yes
\tilde{l}_v	a_v	a_λ	a_λ	$a_v \times 10^{-2}$	$a_v \times 10^{-2}$	stable	no
\tilde{l}_v	a_v	$a_\lambda \times 10^{-2}$	$a_\lambda \times 10^{-2}$	≈ 0	≈ 0	unstable	–

711 In this second scenario, the relative weight attributed to the nonlocal plastic volumetric deformation
 712 reduces. Remember that, given that normalized diffusive length $\tilde{l}_\lambda = \tilde{l}_v$, equivalent spatial averaging for
 713 both $\tilde{\lambda}$ and $\tilde{\epsilon}_v^p$ is effectuated by the regularizing Helmholtz equations. Furthermore, by dint of Eq. (14), we
 714 set the baseline stiffnesses $a_\lambda = a_v$. Thus, a bolstered $\tilde{\lambda}$ -penalty energy suppresses shear bands per Fig. 24,
 715 even though deviatoric and volumetric deformation couples through B_λ . Conversely as the trace-related

716 micromorphic stiffness K_v increases, strain successfully localizes like in the initial examples (i.e. Fig. 5). We
 717 summarize the different regularization parameterizations in Table 2.

718 6.2 3D triaxial compression

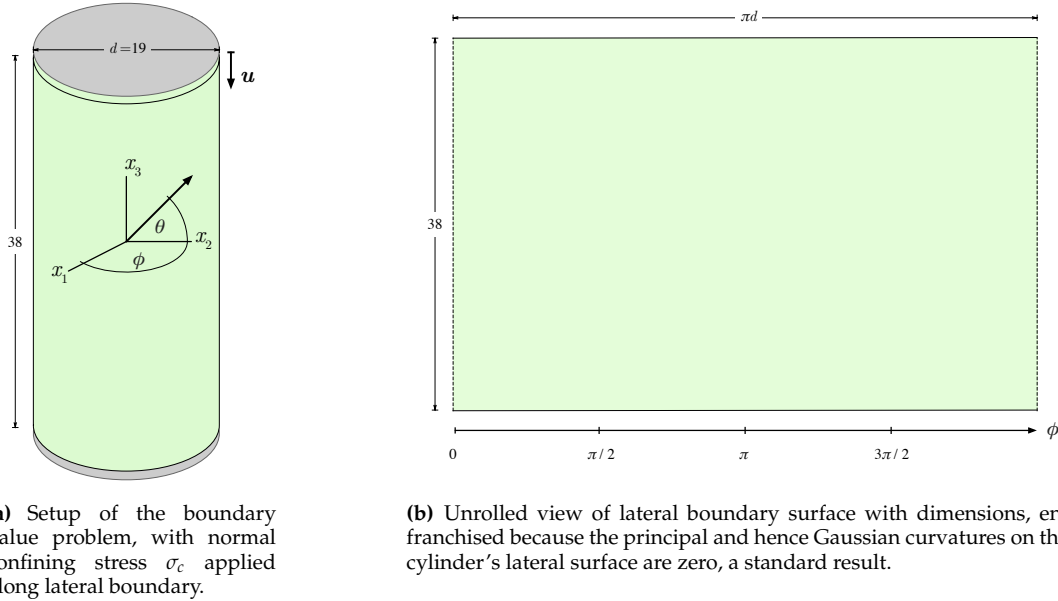


Fig. 25: Geometry of the numerical specimen for 3D plasticity simulations, showing: (a) Euler angles θ and ϕ , for the axis origin located at the centroid of the cylinder; and, (b) unrolled lateral surface parametrized by ϕ , in the manner of Tien et al. [2006].

719 For the 3D simulations, local elastoplastic material parameters are identical to those in the 2D plane
 720 strain cases with $\text{OCR} = 30$. Micromorphic stiffness are identically obtained via Eq. (14). The boundary
 721 value problem's geometry is enlarged and 3D, Fig. 25(a). The geometry's dimensions approximate the
 722 inch-scale used for triaxial test specimens of common rocks [Oku et al., 2007, Vachaparampil and Ghas-
 723 semi, 2017]. Compressive confining stress $\sigma_c = -1$ MPa is applied on the lateral boundary. The loading
 724 increment along the displacement-controlled boundary is $\Delta u_3 = 5.0 \times 10^{-4}$ mm downwards, which has
 725 been scaled w.r.t. the problem dimensions from the 2D cases. The displacements are fixed at zero along the
 726 bottom surface.

727 Numerical parameters are as follows. The baseline diffusive lengths are $\tilde{l}_\lambda = \tilde{l}_v = 0.5$ mm, approxi-
 728 mating the sub-microscale length of composite deformation behavior, identified for layered, bedded sed-
 729 imentary rock with clay matrix in Bennett et al. [2015a]. Interpreting the mesh-independent convergence
 730 of the 2D boundary force-displacement curves and global state paths, the maximum characteristic element
 731 length $h = 0.5 \tilde{l}_\lambda < 0.7 \tilde{l}_\lambda$. As such, we import an initial unstructured mesh containing $n_0 = 1539$ elements.
 732 Each additional level of refinement l_h equally partitions every cell at the previous level of refinement into
 733 eight cells (in 3D). The refined mesh contains $n_0 \times 8^{l_h} = 787968$ cells for $l_h = 3$, requiring computations
 734 distributed over 24 processors.

735 Parameterizing θ_l normalizes $l \sim [0, 1, \tan(\theta_l)]$, restricting $l \cdot l = 1$. Results are presented in Fig. 27 and
 736 Fig. 28. As anticipated, for $\theta_l = 0$, the result is periodic in ϕ with period π . Symmetric shear bands develop
 737 about axis $\theta = 0$. For $0 < \theta_l < \pi/2$ in contrast, the strain localization is antisymmetric about axis $\gamma = \pi$,
 738 i.e. the unrolled surface's centerline.

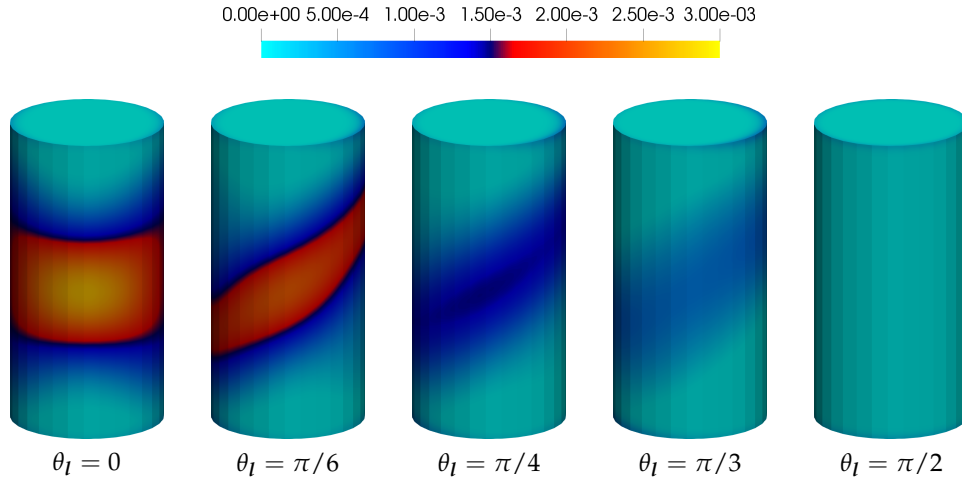


Fig. 26: Micromorphic equivalent plastic strain variable $\tilde{\lambda}$ for 3D compression anisotropic cases with OCR = 30, inducing local anisotropy by setting $E = 2400$ MPa and $\beta^{\text{dev}} = \beta^{\text{vol}} = 0.8$, at $u_3 = 0.05$ mm downwards (LA-MI).

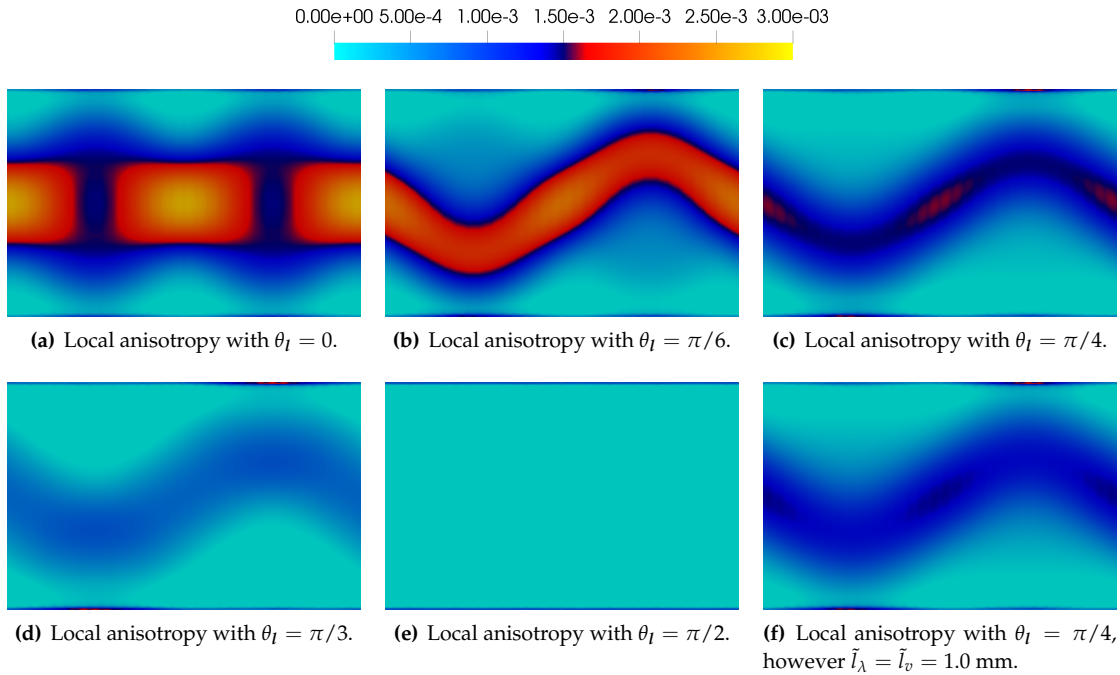


Fig. 27: Equivalent plastic strain λ for 3D compression anisotropic cases with OCR = 30 and rotation of microstructural direction, inducing local anisotropy by setting $E = 2400$ MPa and $\beta^{\text{dev}} = \beta^{\text{vol}} = 0.8$, at $u_3 = 0.05$ mm downwards. Unrolled view of the lateral surface is explained by Fig. 25(b) and is in the manner of Tien et al. [2006] (LA-MI).

739 In comparison to the 2D results, two trends are most notable. First, onset of the plastic response is
 740 controlled by the local elastic anisotropy, Fig. 29. Second, because the plane strain constraint is relaxed, we
 741 observe strain localization for all Euler angles θ_l parameterizing the local microstructural direction. This is
 742 obvious in the body-averaged state paths, Fig. 30(a).

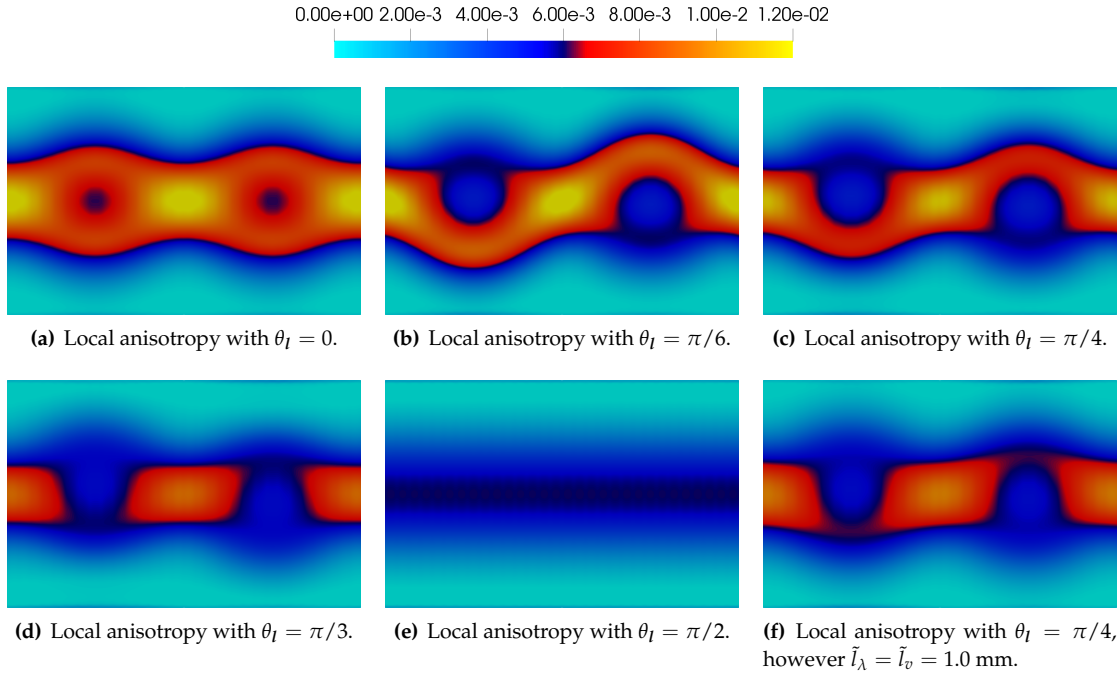


Fig. 28: Equivalent plastic strain λ for 3D compression anisotropic cases with $\text{OCR} = 30$ and rotation of microstructural direction, inducing local anisotropy by setting $E = 2400$ MPa and $\beta^{\text{dev}} = \beta^{\text{vol}} = 0.8$, at $u_3 = 0.125$ mm downwards. Unrolled view of the lateral surface is explained by Fig. 25(b) and is in the manner of Tien et al. [2006] (LA-MI).

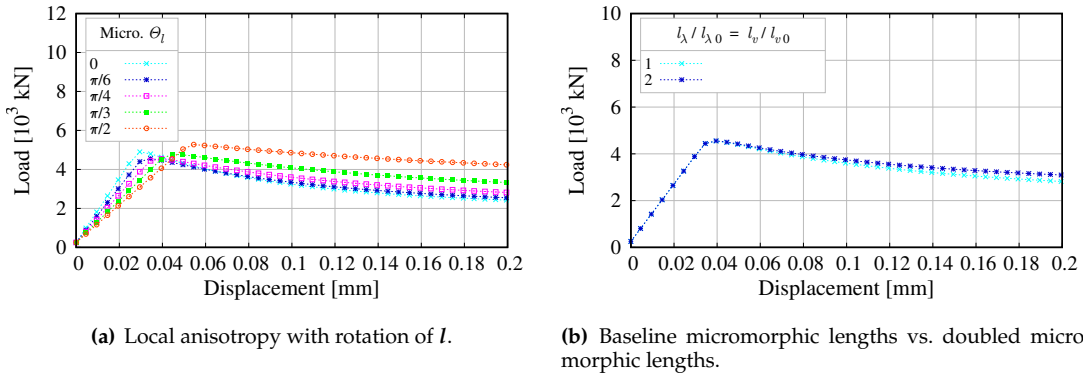
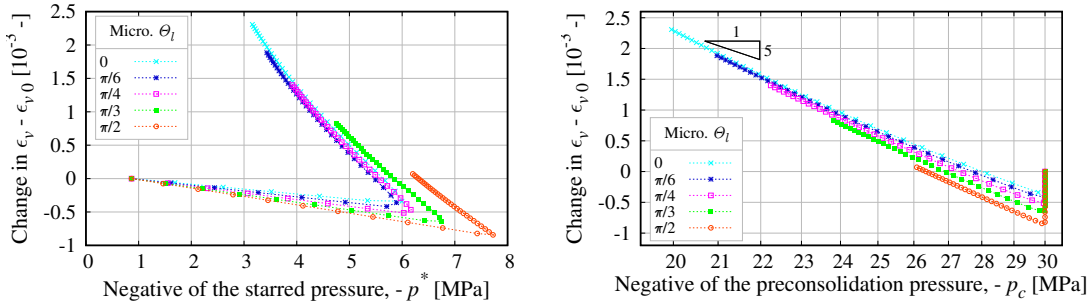


Fig. 29: D compression case, vertical force vs. vertical displacement curves, showing: (a) anisotropic cases with increasing microstructural angle θ_l ; and, (b) anisotropy with $\theta_l = \pi/4$ at two micromorphic regularization lengths (LA-MI).

743 Doubling the micromorphic length scales $\tilde{l}_\lambda = \tilde{l}_v$ elicits the anticipated result. Regardless of doubling
744 $\tilde{l}_\lambda = \tilde{l}_v$, the centerline and width of diffuse plastic strain occurring prior to localization are unaffected.
745 As deformation localizes, however, the smaller micromorphic lengths are useful: compare Fig. 27(c) to
746 Fig. 27(f). For the baseline case, a thin sinusoidal internal structure is apparent (in the unrolled view),
747 but disappears for the doubled micromorphic length-scale. Yet the antisymmetric and eventual symmetric
748 band's concentrated profile only minorly enhances the specimens' overall compliance, Fig. 30(b).



(a) Body-averaged state path, evidencing softening with some localization in all 3D cases.

(b) Semilog plot, evidencing softening with some localization in all 3D cases and fair recovery of the slope $-(C_d) \times 10^3$.

Fig. 30: 3D compression case comparing local anisotropy with increasing microstructural angle θ_l , globally averaged material state curves, showing: (a) and (b), loading paths for change in ϵ_v , such that loading paths begin at 0 in the ordinate axis (LA-MI).

749 7 Conclusion

750 We introduce a mathematical framework that captures the distinctive anisotropies induced at local and
 751 mesoscopic scales. The local anisotropy is replicated via an operator that maps the physical anisotropic
 752 responses to a fictitious isotropic space, such that yield function can be formulated via invariants in the
 753 fictitious space. Meanwhile, the mesoscale anisotropy is induced by a gradient-regularization mechanism
 754 that is inherently anisotropic. Using a variational framework that employs penalty between local internal
 755 variables and solutions of the modified Helmholtz equations, we introduce relaxation energy functionals
 756 and concomitant anisotropic regularization of the projected internal variables. The resultant incremental
 757 energy functional yields Euler-Lagrange equations describing the incremental constitutive update of the
 758 gradient-enhanced constitutive laws. Important upshots of this local-global penalty approach include: (1)
 759 gradient-dependent flow rules without requiring significant modification in the local return mapping al-
 760 gorithm; (2) different anisotropic features co-exist and interact across length scales; (3) mesoscale plastic
 761 flow directions not co-axial to the stress gradient of the yield function, without requiring the introduction
 762 of plastic potential; (4) ameliorated and/or resolved spurious mesh dependency in the softening regimes;
 763 and yet, (5) no requirement for the identification of plastic zone or projection of local internal variables at
 764 each incremental time step. Our numerical simulations performed on homogeneous numerical specimens
 765 indicates that the new constitutive law is capable of replicating an unusually wide spectrum of complex
 766 elastoplastic macroscopic responses. Various types of shear band of different orientations, band width
 767 and forms are evidenced, and induced by changing the structural orientations, local material parameters,
 768 and the anisotropic regularization. This ability to replicate a diverse responses is a necessary feature for
 769 surrogate models or effective media to sufficiently represent complex microstructures whose anisotropic
 770 behaviors originated from different features across length scales.

771 Future work may include the formulation of sequential inverse problems and sensitivity analysis on
 772 the material parameters for the micromorphic-enhanced constitutive laws (cf. Ehlers and Scholz [2007]),
 773 the incorporation of multi-physical coupling effects due to heat transfer and pore-fluid diffusion inside the
 774 porous materials, and the extension of this mathematical framework in the finite deformation range. In
 775 particular, it is likely that an additive kinematic framework that employs the logarithmic strain space in
 776 Miehe et al. [2002] might be used to extend the current model to the finite strain regime while ensuring
 777 objectivity. However, as proven recently by Neff and Ghiba [2016], a major challenge would be to ensure
 778 that the rank-one convexity is preserved during the plastic flow for the additive logarithmic plasticity
 779 model with non-coaxial plastic deformation $C \cdot C^{p-1} \neq C^{p-1} \cdot C$. The authors are currently undertaking
 780 this challenge and will report the results if sufficient progress have been made.

8 Acknowledgments

This research is supported by the Earth Materials and Processes program from the US Army Research Office under grant contract W911NF-18-2-0306, the Dynamic Materials and Interactions Program from the Air Force Office of Scientific Research under grant contract FA9550-17-1-0169, the Nuclear Energy University program from the Department of Energy under grant contract DE-NE0008534 as well as the Mechanics of Materials and Structures program at National Science Foundation under grant contract CMMI-1462760. These supports are gratefully acknowledged. The views and conclusions contained in this document are those of the authors, and should not be interpreted as representing the official policies, either expressed or implied, of the sponsors, including the Army Research Laboratory or the U.S. Government. The U.S. Government is authorized to reproduce and distribute reprints for government purposes notwithstanding any copyright notation herein.

References

- N. Abboud and G. Scovazzi. Elastoplasticity with linear tetrahedral elements: A variational multiscale method. *International Journal for Numerical Methods in Engineering*, 115(8):913–955, 2018.
- B. Adams, M. Ebeida, M. Eldred, G. Geraci, J. Jakeman, K. Maupin, J. Stephens, J. Monschke, L. Swiler, D. Virgil, T. Wildey, D. Gay, W. Bohnhoff, K. Dalbey, J. Eddy, J. Frye, R. Hooper, K. Hu, P. Hough, M. Khalil, E. Ridgway, and J. Winokur. DAKOTA, a multilevel parallel object-oriented framework for design optimization, parameter estimation, uncertainty quantification, and sensitivity analysis: Version 6.8 user’s manual. Technical report, Sandia National Laboratories, 2018.
- F. Aldakheel. Micromorphic approach for gradient-extended thermo-elastic-plastic solids in the logarithmic strain space. *Continuum Mechanics and Thermodynamics*, 26(6):1207–1217, 2017.
- F. Aldakheel and C. Miehe. Coupled thermomechanical response of gradient plasticity. *International Journal of Plasticity*, 91:1–24, 2017.
- F. Armero and J. Simo. A new unconditionally stable fractional step method for non-linear coupled thermomechanical problems. *International Journal for Numerical Methods in Engineering*, 35(4):737–766, 1992.
- W. Bangerth, R. Hartmann, and G. Kanschat. deal.II – A general purpose object-oriented finite element library. *ACM Transactions on Mathematical Software*, 33(4):24/1–24/27, 2007.
- K. Bennett, L. Berla, W. Nix, and R. Borja. Instrumented nanoindentation and 3D mechanistic modeling of a shale at multiple scales. *Acta Geotechnica*, 10(1):1–14, 2015a.
- K. Bennett, R. Regueiro, and D. Luscher. Anisotropic finite hyper-elastoplasticity of geomaterials with Drucker-Prager/Cap type constitutive model formulation. *International Journal of Plasticity*, accepted.
- K. C. Bennett, L. A. Berla, W. D. Nix, and R. I. Borja. Instrumented nanoindentation and 3d mechanistic modeling of a shale at multiple scales. *Acta Geotechnica*, 10(1):1–14, 2015b.
- R. Borja. Conditions for instabilities in collapsible solids including volume implosion and compaction banding. *Acta Geotechnica*, 1(2):107–122, 2006.
- R. Borja and C. Tamagnini. Cam-clay plasticity, part III: Extension of the infinitesimal model to include finite strains. *Computer Methods in Applied Mechanics and Engineering*, 155(1-2):73–95, 1998.
- R. I. Borja. *Plasticity: Modeling & Computation*. Springer-Verlag Berlin Heidelberg, 2013.
- E. C. Bryant and W. Sun. A mixed-mode phase field fracture model in anisotropic rocks with consistent kinematics. *Computer Methods in Applied Mechanics and Engineering*, 342:561–584, 2018.
- R. Butterfield. A natural compression law for soils (an advance on $e\text{-log } p'$). *Géotechnique*, 29(4), 1979.
- J.-S. Chen, S. Yoon, and C.-T. Wu. Non-linear version of stabilized conforming nodal integration for galerkin mesh-free methods. *International Journal for Numerical Methods in Engineering*, 53(12):2587–2615, 2002.
- J. Cheng, A. Shahba, and S. Ghosh. Stabilized tetrahedral elements for crystal plasticity finite element analysis overcoming volumetric locking. *Computational Mechanics*, 57(5):733–753, 2016.
- J. Choo and S. Lee. Enriched galerkin finite elements for coupled poromechanics with local mass conservation. *Computer Methods in Applied Mechanics and Engineering*, 341:311–332, 2018.
- J. Choo and W. Sun. Coupled phase-field and plasticity modeling of geological materials: From brittle fracture to ductile flow. *Computer Methods in Applied Mechanics and Engineering*, 2017.

- 831 J. Choo, J. A. White, and R. I. Borja. Hydromechanical modeling of unsaturated flow in double porosity
832 media. *International Journal of Geomechanics*, 16(6):D4016002, 2016.
- 833 J. Clayton and J. Knap. Phase field modeling of directional fracture in anisotropic polycrystals. *Computa-
834 tional Materials Science*, 98:158–169, 2015.
- 835 K. Collins and A. McGown. The form and function of microfabric features in a variety of natural soils.
836 *Géotechnique*, 24(2):223–254, 1974.
- 837 A. Crook, J.-g. Yu, and S. Willson. Development of an orthotropic 3D elastoplastic material model for shale.
838 In *SPE/ISRM Rock Mechanics Conference*. Society of Petroleum Engineers, 2002.
- 839 E. de Souza Neto, D. Peric, and D. Owen. *Computational Methods for Plasticity*. John Wiley & Sons, Ltd,
840 2008.
- 841 J. Dellinger, D. Vasicek, and C. Sondergeld. Kelvin notation for stabilizing elastic-constant inversion. *Revue
842 de l’Institut Français du Pétrole*, 53(5):709–719, 2006.
- 843 J. Dennis, D. Gay, and R. Welsch. Algorithm 573: NL2SOL – An adaptive nonlinear least-squares algorithm
844 [E4]. *ACM Transactions on Mathematical Software*, 7(3):369–383, 1981.
- 845 G. Desbois, J. L. Urai, and J. H. de Bresser. Fluid distribution in grain boundaries of natural fine-grained
846 rock salt deformed at low differential stress (Qom Kuh salt fountain, central Iran): Implications for rhe-
847 ology and transport properties. *Journal of Structural Geology*, 43:128–143, 2012.
- 848 W. Ehlers and B. Scholz. An inverse algorithm for the identification and the sensitivity analysis of the
849 parameters governing micropolar elasto-plastic granular material. *Archive of Applied Mechanics*, 77(12):
850 911, 2007.
- 851 S. Forest. Micromorphic approach for gradient elasticity, viscoplasticity, and damage. *Journal of Engineering
852 Mechanics*, 135(3):117–131, 2009.
- 853 S. Forest. Nonlinear regularization operators as derived from the micromorphic approach to gradient elas-
854 ticity, viscoplasticity and damage. *Proceedings of the Royal Society A: Mathematical, Physical and Engineering
855 Science*, 472(2188):20150755, 2016.
- 856 S. Forest, J. Mayeur, and D. McDowell. Micromorphic crystal plasticity. *Handbook of Nonlocal Continuum
857 Mechanics for Materials and Structures*, pages 1–44, 2018.
- 858 P. Habib, J. Bernaix, et al. The fissuration of rocks. In *1st International Society for Rock Mechanics Congress*.
859 International Society for Rock Mechanics, 1966.
- 860 F. Hashagen and R. de Borst. Enhancement of the Hoffman yield criterion with an anisotropic hardening
861 model. *Computers & Structures*, 79(6):637–651, 2001.
- 862 K. Hashiguchi and M. Ueno. From hvorslev’s failure criterion to failure condition. In *Proc. Intern. Conf. Soil
863 Mech. and Found. Eng., 9th., Tokyo*, volume 50, pages 123–126, 1977.
- 864 K. Ikeda, Y. Yamakawa, and S. Tsutsumi. Simulation and interpretation of diffuse mode bifurcation of
865 elastoplastic solids. *Journal of the Mechanics and Physics of Solids*, 51(9):1649–1673, 2003.
- 866 M. Itskov. On the theory of fourth-order tensors and their applications in computational mechanics. *Com-
867 puter Methods in Applied Mechanics and Engineering*, 189(2):419–438, 2000.
- 868 A. Krischok and C. Linder. On the enhancement of low-order mixed finite element methods for the large
869 deformation analysis of diffusion in solids. *International Journal for Numerical Methods in Engineering*, 106
870 (4):278–297, 2016.
- 871 I. Kunin. An algebra of tensor operators and its applications to elasticity. *International Journal of Engineering
872 Science*, 19(12):1551–1561, 1981.
- 873 Y. Liu, W. Sun, Z. Yuan, and J. Fish. A nonlocal multiscale discrete-continuum model for predicting me-
874 chanical behavior of granular materials. *International Journal for Numerical Methods in Engineering*, 106(2):
875 129–160, 2016.
- 876 V. Lubarda and M. Chen. On the elastic moduli and compliances of transversely isotropic and orthotropic
877 materials. *Journal of Mechanics of Materials and Structures*, 3(1):153–171, 2008.
- 878 C. Miehe, N. Apel, and M. Lambrecht. Anisotropic additive plasticity in the logarithmic strain space:
879 modular kinematic formulation and implementation based on incremental minimization principles for
880 standard materials. *Computer Methods in Applied Mechanics and Engineering*, 191(47-48):5383–5425, 2002.
- 881 C. Miehe, M. Hofacker, and F. Welschinger. A phase field model for rate-independent crack propagation:
882 Robust algorithmic implementation based on operator splits. *Computer Methods in Applied Mechanics and
883 Engineering*, 199(45):2765–2778, 2010.

- 884 C. Miehe, F. Aldakheel, and S. Mauthe. Mixed variational principles and robust finite element implemen-
885 tations of gradient plasticity at small strains. *International Journal for numerical methods in engineering*, 94
886 (11):1037–1074, 2013.
- 887 C. Miehe, M. Hofacker, L.-M. Schänzel, and F. Aldakheel. Phase field modeling of fracture in multi-physics
888 problems. part ii. coupled brittle-to-ductile failure criteria and crack propagation in thermo-elastic-
889 plastic solids. *Computer Methods in Applied Mechanics and Engineering*, 294:486–522, 2015.
- 890 C. Miehe, S. Teichtmeister, and F. Aldakheel. Phase-field modelling of ductile fracture: A variational
891 gradient-extended plasticity-damage theory and its micromorphic regularization. *Phil. Trans. R. Soc.*
892 *A*, 374(2066):20150170, 2016.
- 893 A. Mota, Q. Chen, J. Foulk, J. Ostien, and Z. Lai. A Cartesian parametrization for the numerical analysis of
894 material instability. *International Journal for Numerical Methods in Engineering*, 108(2):156–180, 2016.
- 895 S. Na, W. Sun, M. Ingraham, and H. Yoon. Effects of spatial heterogeneity and material anisotropy on
896 the fracture pattern and macroscopic effective toughness of mancos shale in brazilian tests. *Journal of*
897 *Geophysical Research: Solid Earth*, 122(8):6202–6230, 2017.
- 898 P. Neff and I.-D. Ghiba. Loss of ellipticity for non-coaxial plastic deformations in additive logarithmic finite
899 strain plasticity. *International Journal of Non-Linear Mechanics*, 81:122–128, 2016.
- 900 H. Niandou, J. Shao, J. Henry, and D. Fourmaintraux. Laboratory investigation of the mechanical behaviour
901 of Tournemire shale. *International Journal of Rock Mechanics and Mining Sciences*, 34(1):3–16, 1997.
- 902 H. Oku, B. Haimson, and S.-r. Song. True triaxial strength and deformability of the siltstone overlying the
903 Chelungpu fault (Chi-Chi earthquake), Taiwan. *Geophysical Research Letters*, 34(9):293–304, 2007.
- 904 M. Ortiz and A. Pandolfi. A variational Cam-clay theory of plasticity. *Computer Methods in Applied Mechan-*
905 *ics and Engineering*, 193(27-29):2645–2666, 2004.
- 906 M. Ortiz and L. Stainier. The variational formulation of viscoplastic constitutive updates. *Computer Methods*
907 *in Applied Mechanics and Engineering*, 171(3-4):419–444, 1999.
- 908 M. S. Paterson and T.-f. Wong. *Experimental rock deformation-the brittle field*. Springer Science & Business
909 Media, 2005.
- 910 D. M. Potts, L. Zdravkovic, and L. Zdravković. *Finite element analysis in geotechnical engineering: application*,
911 volume 2. Thomas Telford, 2001.
- 912 S. Reese and P. Wriggers. A stabilization technique to avoid hourglassing in finite elasticity. *International*
913 *Journal for Numerical Methods in Engineering*, 48(1):79–109, 2000.
- 914 S. Reese, H. Bayat, and S. Wulfinghoff. On an equivalence between a discontinuous galerkin method
915 and reduced integration with hourglass stabilization for finite elasticity. *Computer Methods in Applied*
916 *Mechanics and Engineering*, 325:175–197, 2017.
- 917 K. Roscoe and A. Schofield. Mechanical behaviour of an idealized ‘wet-clay’. In *2nd European Conference*
918 *on Soil Mechanics and Foundation Engineering*, pages 47–54. Wiesbaden, 1963.
- 919 A. Schofield and P. Wroth. *Critical state soil mechanics*, volume 310. McGraw-Hill London, 1968.
- 920 G. Scovazzi, B. Carnes, X. Zeng, and S. Rossi. A simple, stable, and accurate linear tetrahedral finite el-
921 ement for transient, nearly, and fully incompressible solid dynamics: a dynamic variational multiscale
922 approach. *International Journal for Numerical Methods in Engineering*, 106(10):799–839, 2016.
- 923 S. Semnani, J. White, and R. Borja. Thermoplasticity and strain localization in transversely isotropic mate-
924 rials based on anisotropic critical state plasticity. *International Journal for Numerical and Analytical Methods*
925 *in Geomechanics*, 40(18):2423–2449, 2016.
- 926 J. Simo. Numerical analysis and simulation of plasticity. *Handbook of Numerical Analysis*, pages 183–499,
927 1998.
- 928 J. Simo and T. Hughes. *Computational Inelasticity*. Springer-Verlag New York, 1998.
- 929 J. Simo and R. Taylor. A return mapping algorithm for plane stress elastoplasticity. *International Journal for*
930 *Numerical Methods in Engineering*, 22(3):649–670, 1986.
- 931 A. Stankiewicz and J. Pamin. Gradient-enhanced Cam-clay model in simulation of strain localization in
932 soil. *Foundations of Civil and Environmental Engineering*, 7:293–318, 2006.
- 933 W. Sun. A unified method to predict diffuse and localized instabilities in sands. *Geomechanics and Geoengi-*
934 *neering*, 8(2):65–75, 2013.
- 935 W. Sun. A stabilized finite element formulation for monolithic thermo-hydro-mechanical simulations at
936 finite strain. *International Journal for Numerical Methods in Engineering*, 103(11):798–839, 2015.

- 937 W. Sun and J. E. Andrade. Diffuse bifurcations of porous media under partially drained conditions. In
 938 *Multiscale and Multiphysics Processes in Geomechanics*, pages 61–64. Springer, 2011.
- 939 W. Sun, J. T. Ostien, and A. G. Salinger. A stabilized assumed deformation gradient finite element formu-
 940 lation for strongly coupled poromechanical simulations at finite strain. *International Journal for Numerical
 941 and Analytical Methods in Geomechanics*, 37(16):2755–2788, 2013.
- 942 W. Sun, Q. Chen, and J. T. Ostien. Modeling the hydro-mechanical responses of strip and circular punch
 943 loadings on water-saturated collapsible geomaterials. *Acta Geotechnica*, 9(5):903–934, 2014.
- 944 S. Teichtmeister, D. Kienle, F. Aldakheel, and M. Keip. Phase field modeling of fracture in anisotropic brittle
 945 solids. *International Journal of Non-Linear Mechanics*, 97:1–21, 2017.
- 946 Y. Tien, M. Kuo, and C. Juang. An experimental investigation of the failure mechanism of simulated trans-
 947 versely isotropic rocks. *International Journal of Rock Mechanics and Mining Sciences*, 43(8):1163–1181, 2006.
- 948 A. Vachaparampil and A. Ghassemi. Failure characteristics of three shales under true-triaxial compression.
 949 *International Journal of Rock Mechanics and Mining Sciences*, 100:151–159, 2017.
- 950 D. Versino and K. C. Bennett. Generalized radial-return mapping algorithm for anisotropic von mises
 951 plasticity framed in material eigenspace. *International Journal for Numerical Methods in Engineering*, 116
 952 (3):202–222, 2018.
- 953 L. J. Walpole. Fourth-rank tensors of the thirty-two crystal classes: multiplication tables. *Proceedings of the
 954 Royal Society A: Mathematical, Physical and Engineering Sciences*, 391(1800):149–179, 1984.
- 955 K. Wang and W. Sun. A semi-implicit discrete-continuum coupling method for porous media based on
 956 the effective stress principle at finite strain. *Computer Methods in Applied Mechanics and Engineering*, 304:
 957 546–583, 2016.
- 958 K. Wang and W. Sun. A multiscale multi-permeability poroplasticity model linked by recursive homoge-
 959 nizations and deep learning. *Computer Methods in Applied Mechanics and Engineering*, 334:337–380, 2018.
- 960 K. Wang, W. Sun, S. Salager, S. Na, and G. Khaddour. Identifying material parameters for a micro-polar
 961 plasticity model via x-ray micro-ct images: lessons learned from the curve-fitting exercises. *International
 962 Journal for Multiscale Computational Engineering*, 2016.
- 963 W. Weibull. A statistical distribution function of wide applicability. *Journal of Applied Mechanics*, 18(3):
 964 293–297, 1951.
- 965 K. Weinberg, A. Mota, and M. Ortiz. A variational constitutive model for porous metal plasticity. *Compu-
 966 tational Mechanics*, 37(2):142–152, 2006.
- 967 M. Wheeler, T. Wick, and W. Wollner. An augmented-lagrangian method for the phase-field approach for
 968 pressurized fractures. *Computer Methods in Applied Mechanics and Engineering*, 271:69–85, 2014.
- 969 J. A. White and R. I. Borja. Stabilized low-order finite elements for coupled solid-deformation/fluid-
 970 diffusion and their application to fault zone transients. *Computer Methods in Applied Mechanics and Engi-
 971 neering*, 197(49-50):4353–4366, 2008.
- 972 D. M. Wood. *Soil behaviour and critical state soil mechanics*. Cambridge university press, 1990.
- 973 Q. Yang, L. Stainier, and M. Ortiz. A variational formulation of the coupled thermo-mechanical boundary-
 974 value problem for general dissipative solids. *Journal of the Mechanics and Physics of Solids*, 54(2):401–424,
 975 2006.
- 976 O. C. Zienkiewicz, A. H. C. Chan, M. Pastor, B. A. Schrefler, and T. Shiomi. *Computational Geomechanics*.
 977 Wiley Chichester, 1999.

978 A Appendix: Kelvin notation

979 Kelvin notation is a *reduced* matrix/vector notation: it accounts for symmetry of second- and fourth-order
 980 tensors. Thus for symmetric second-order stress tensor $\sigma = \partial W^e / \partial \epsilon^e$ and elastic strain tensor ϵ^e , we

981 compare traditional Voigt-notated versus Kelvin-notated vector equivalents:

$$\bar{\sigma} = \begin{bmatrix} \bar{\sigma}_1 \\ \bar{\sigma}_2 \\ \bar{\sigma}_3 \\ \bar{\sigma}_4 \\ \bar{\sigma}_5 \\ \bar{\sigma}_6 \end{bmatrix}_{6 \times 1} = \underbrace{\begin{bmatrix} \sigma_{11} \\ \sigma_{22} \\ \sigma_{33} \\ \sigma_{23} \\ \sigma_{13} \\ \sigma_{12} \end{bmatrix}}_{\text{Voigt}}_{6 \times 1} = \underbrace{\begin{bmatrix} \sigma_{11} \\ \sigma_{22} \\ \sigma_{33} \\ \sqrt{2}\sigma_{23} \\ \sqrt{2}\sigma_{13} \\ \sqrt{2}\sigma_{12} \end{bmatrix}}_{\text{Kelvin}}_{6 \times 1}, \quad \bar{\epsilon}^e = \begin{bmatrix} \bar{\epsilon}_1^e \\ \bar{\epsilon}_2^e \\ \bar{\epsilon}_3^e \\ \bar{\epsilon}_4^e \\ \bar{\epsilon}_5^e \\ \bar{\epsilon}_6^e \end{bmatrix}_{6 \times 1} = \underbrace{\begin{bmatrix} \epsilon_{11}^e \\ \epsilon_{22}^e \\ \epsilon_{33}^e \\ 2\epsilon_{23}^e \\ 2\epsilon_{13}^e \\ 2\epsilon_{12}^e \end{bmatrix}}_{\text{Voigt}}_{6 \times 1} = \underbrace{\begin{bmatrix} \epsilon_{11}^e \\ \epsilon_{22}^e \\ \epsilon_{33}^e \\ \sqrt{2}\epsilon_{23}^e \\ \sqrt{2}\epsilon_{13}^e \\ \sqrt{2}\epsilon_{12}^e \end{bmatrix}}_{\text{Kelvin}}_{6 \times 1}. \quad (44)$$

In comparison to Voigt-notated vectors and matrices, Kelvin notation's significant advantage is immediately apparent upon contraction: norms of both second-order tensors like the stress σ and fourth-order tensors like the elastic stiffness tensor C^e are preserved, leading to a geometric interpretation of matrix eigenvectors [Dellinger et al., 2006]. Nonetheless the strain tensor resolves quadratically as $\epsilon^e : C^e : \epsilon^e = \bar{\epsilon}^e{}^T C^e \bar{\epsilon}^e$, and so forth. For symmetric fourth-order elastic stiffness tensor C^e , the Kelvin-notation matrix equivalent is:

$$C^e = \underbrace{\begin{bmatrix} C_{1111}^e & C_{1122}^e & C_{1133}^e & \sqrt{2}C_{1123}^e & \sqrt{2}C_{1113}^e & \sqrt{2}C_{1112}^e \\ C_{2211}^e & C_{2222}^e & C_{2233}^e & \sqrt{2}C_{2223}^e & \sqrt{2}C_{2213}^e & \sqrt{2}C_{2212}^e \\ C_{3311}^e & C_{3322}^e & C_{3333}^e & \sqrt{2}C_{3323}^e & \sqrt{2}C_{3313}^e & \sqrt{2}C_{3312}^e \\ \sqrt{2}C_{2311}^e & \sqrt{2}C_{2322}^e & \sqrt{2}C_{2333}^e & 2C_{2323}^e & 2C_{2312}^e & 2C_{2312}^e \\ \sqrt{2}C_{1311}^e & \sqrt{2}C_{1322}^e & \sqrt{2}C_{1333}^e & 2C_{1323}^e & 2C_{1313}^e & 2C_{1312}^e \\ \sqrt{2}C_{1211}^e & \sqrt{2}C_{1222}^e & \sqrt{2}C_{1233}^e & 2C_{1223}^e & 2C_{1213}^e & 2C_{1212}^e \end{bmatrix}}_{\text{Kelvin}}_{6 \times 6}. \quad (45)$$

982 Derivatives are also straightforward. Component-wise for example, we note that $\partial \bar{\sigma} / \partial \bar{\sigma}_4 = [0 \ 0 \ 0 \ 1 \ 0 \ 0]^T$.

983 Finally, we note that the symmetry of second order tensors σ and ϵ^e enables $\bar{\sigma}^e$ and $\bar{\epsilon}^e$ to be six component vectors. Conversely, as C^e is both symmetric and six-by-six matrix-representable, its fourth-order tensor equivalent C^e exhibits both the major and minor symmetries, respectively. In our study, the elasto-plastic tangent matrix C^{ep} is also symmetric. As such, its tensor equivalent C^{ep} similarly combines both the minor and major symmetries, and is hence 'super-symmetric' cf. Itskov [2000].

988 B Appendix: Transversely isotropic elasticity

Per Lubarda and Chen [2008] for example, E and ν are the Young's modulus and Poisson ratio in the plane of isotropy and characterizing transverse contraction in the plane of isotropy due to tension applied in the perpendicular direction within the plane of isotropy, respectively. E_l and ν_l are the Young's modulus and Poisson ratio in the isotropic plane's normal direction and characterizing transverse contraction in the plane of isotropy due to tension applied in the isotropic plane's normal direction, respectively. In lieu of data, the shear modulus μ_l can be estimated Saint-Venant's formula [Crook et al., 2002, Niandou et al., 1997]:

$$\frac{1}{\mu_l} \approx \frac{1}{E} + \frac{1}{E_l} + 2\frac{\nu_l}{E_l}. \quad (46)$$

Extracting c_1 through c_5 is then a series of purely algebraic steps. This begins with computing the compliance moduli (with unspecified rotation of material-to-global coordinate systems, assuming local x_3

is the out-of-isotropic-plane direction), see [Lubarda and Chen \[2008\]](#):

$$S_{11}^e = S_{22}^e = \frac{1}{E}, \quad S_{12}^e = -\frac{\nu}{E}, \quad S_{13}^e = S_{23}^e = -\frac{\nu_l}{E_l}, \quad S_{33}^e = \frac{1}{E_l}, \quad S_{44}^e = S_{55}^e = \frac{1}{2\mu_l}, \quad S_{66}^e = S_{11}^e - S_{12}^e.$$

For $1/C^e = S_{11}^e + S_{12}^e - 2(S_{13}^e)^2/S_{33}^e$, the matrix-stiffness moduli are determined as:

$$\begin{aligned} C_{11}^e &= \frac{S_{11}^e - (S_{13}^e)^2/S_{33}^e}{S_{11}^e - S_{12}^e} C^e, & C_{12}^e &= -\frac{S_{12}^e - (S_{13}^e)^2/S_{33}^e}{S_{11}^e - S_{12}^e} C^e, \\ C_{13}^e &= -\frac{S_{13}^e}{S_{33}^e} C^e, & C_{33}^e &= \frac{S_{11}^e + S_{12}^e}{E_l} C^e, & C_{44}^e &= \frac{1}{S_{44}^e}, & C_{66}^e &= \frac{1}{S_{66}^e}. \end{aligned}$$

Then the coefficients c_1 through c_6 are dimensioned Walpole-algebra coefficients [[Walpole, 1984](#)]. In terms of C^e 's matrix-entries in Eq. (45), the Walpole coefficients are:

$$c_1 = C_{33}^e, \quad c_2 = C_{11}^e + C_{12}^e, \quad c_3 = c_4 = \sqrt{2}C_{13}^e, \quad c_5 = C_{66}^e, \quad c_6 = C_{44}^e. \quad (47)$$

989 By way of comparison between Kelvin and Voigt matrix-vector notations, the Voigt-notated expressions
990 for the entries in the upper right-hand block of the compliance and stiffness matrices are identical with the
991 Kelvin-notated expressions in [Lubarda and Chen \[2008\]](#). Conversely for example, $S_{44}^e \dots S_{66}^e$ and $C_{44}^e \dots C_{66}^e$
992 differ because expressed in Kelvin notation. In particular for example, in Voigt notation $S_{44}^e = S_{55}^e = 1/\mu_l$.

To construct C^e per Eq. (6), all required fourth-order tensors are built as follows. First one obtains the microstructural tensors $\phi = l \otimes l$ orthogonal to $\chi = \mathbf{1} - l \otimes l$, with both idempotent. From these two second-order tensors, all the relevant fourth-order tensors are:

$$\begin{aligned} (E_1)_{ijkl} &= \phi_{ij}\phi_{kl}, & (E_2)_{ijkl} &= \frac{1}{2}\chi_{ij}\chi_{kl}, & (E_3)_{ijkl} &= \frac{1}{\sqrt{2}}\phi_{ij}\chi_{kl}, & (E_4)_{ijkl} &= \frac{1}{\sqrt{2}}\chi_{ij}\phi_{kl}, \\ (F)_{ijkl} &= \frac{1}{2}(\chi_{ik}\chi_{jl} + \chi_{il}\chi_{jk} - \chi_{ij}\chi_{kl}), & (G)_{ijkl} &= \frac{1}{2}(\phi_{ik}\chi_{jl} + \phi_{il}\chi_{jk} + \chi_{ik}\phi_{jl} + \chi_{il}\phi_{jk}). \end{aligned}$$

993 Since E_1, E_2, F , and G each exhibit major symmetry, so does their every combination. I.e. G_{ijkl} contains
994 $\phi_{ik}\chi_{jl}$ but also $\chi_{ik}\phi_{jl}$ to the same coefficient. Secondly they express minor symmetry, which is identifiable
995 by applying the symmetry of ϕ and χ . Thus their every combination qualifies as super-symmetric. In
996 contrast, E_3 and E_4 are not super-symmetric. However as we constrain their coefficients such that $c_3 = c_4$,
997 their every permissible combination exhibits the major symmetry [[Walpole, 1984](#)].

998 C Appendix: Transversely isotropic plasticity

[Semnani et al. \[2016\]](#) previously introduced a transversely isotropic plastic mapping tensor. This linear mapping can be represented by a super-symmetric fourth-order tensor, described by microstructural direction l and the coefficients α, β , and γ . To construct P^P per Eq. (9), all required fourth-order tensors are built as follows.

$$\begin{aligned} (P_1^P)_{ijkl} &= \frac{1}{2}(\delta_{ik}\delta_{jl} + \delta_{il}\delta_{jk}), & (P_2^P)_{ijkl} &= \frac{1}{2}(\phi_{ik}\phi_{jl} + \phi_{il}\phi_{jk}), \\ (P_3^P)_{ijkl} &= \frac{1}{4}(\delta_{ik}\phi_{jl} + \delta_{il}\phi_{jk} + \phi_{ik}\delta_{jl} + \phi_{il}\delta_{jk}), \end{aligned}$$

Formally tensor P^P is a mapping, as lacking idempotence in that $P^P \neq P^P : P^P$, see Section 2.4.1 in [Simo and Hughes \[1998\]](#). It is easy to show that, in terms of the Walpole algebra, Eq. (9) is

$$P^P = \alpha E_1 + \beta (E_2 + F) + \gamma G.$$

999 Alternately, also within the stress-space, the Walpole algebra contains an isotropic-to-transversely-isotropic
 1000 stress-space mapping. Practically, this alternative mapping adds an additional coefficient δ to the mapping.
 1001 The combination of tensors forming the basis for this mapping,

$$\alpha \mathbf{E}_1 + \beta \mathbf{E}_2 + \gamma \mathbf{F} + \delta \mathbf{G},$$

1002 are derived as the symmetric (linearly independent) elements within the symmetric commutative Walpole
 1003 subalgebra [Kunin, 1981]. Each element within the subalgebra is idempotent, hence qualifies a projection
 1004 in Kunin's terms. For all coefficients $\alpha \dots \gamma$ equal to 1, these elements sum to the symmetric fourth-order
 1005 identity tensor. Our notion extends naturally to additional material symmetries, wherein the mapping's
 1006 basis remains the linearly independent elements summing to \mathbf{I} .

1007 C.1 Appendix: Local residual, tangent, and initialization

To derive the local residual $\bar{\mathbf{r}}$, we apply the chain rule to the stationary condition of optimality defining the local Euler-Lagrange equation. Minimizing over the elastic strain,

$$\frac{\delta W(\boldsymbol{\zeta}_{n+1})}{\delta \boldsymbol{\epsilon}_{n+1}^e} = \frac{\partial W(\boldsymbol{\zeta}_{n+1})}{\partial \boldsymbol{\epsilon}_{n+1}^e} = \frac{\partial W(\boldsymbol{\zeta}_{n+1})}{\partial \Delta \boldsymbol{\epsilon}^P} : \frac{\partial \Delta \boldsymbol{\epsilon}^P}{\partial \boldsymbol{\epsilon}^e} = \mathbf{0}.$$

Expanding the above,

$$\begin{aligned} \frac{\partial W(\boldsymbol{\zeta}_{n+1})}{\partial \Delta \boldsymbol{\epsilon}^P} : \frac{\partial \Delta \boldsymbol{\epsilon}^P}{\partial \boldsymbol{\epsilon}^e} &= \left(\frac{\partial W_{n+1}^e}{\partial \boldsymbol{\epsilon}_{n+1}^e} : \frac{\partial \boldsymbol{\epsilon}_{n+1}^e}{\partial \Delta \boldsymbol{\epsilon}^P} + \overbrace{\frac{\partial W_{\alpha n+1}^P}{\partial \lambda_{n+1}} \frac{\partial \lambda_{n+1}}{\partial \Delta \lambda}}^{\partial W_{\alpha n+1}^P / \partial \Delta \lambda} \frac{\partial \Delta \lambda}{\partial \Delta \boldsymbol{\epsilon}^P} + \frac{\partial W_{\alpha n+1}^P}{\partial \boldsymbol{\epsilon}_{v n+1}^P} \frac{\partial \boldsymbol{\epsilon}_{v n+1}^P}{\partial \Delta \boldsymbol{\epsilon}^P} \frac{\partial \Delta \boldsymbol{\epsilon}_v^P}{\partial \Delta \boldsymbol{\epsilon}^P} \right. \\ &\quad \left. + \frac{\partial W_{\lambda, n+1}^P}{\partial \lambda_{n+1}} \frac{\partial \lambda_{n+1}}{\partial \Delta \lambda} \frac{\partial \Delta \lambda}{\partial \Delta \boldsymbol{\epsilon}^P} + \frac{\partial W_{v n+1}^P}{\partial \boldsymbol{\epsilon}_{v n+1}^P} \frac{\partial \boldsymbol{\epsilon}_{v n+1}^P}{\partial \Delta \boldsymbol{\epsilon}^P} \frac{\partial \Delta \boldsymbol{\epsilon}_v^P}{\partial \Delta \boldsymbol{\epsilon}^P} \right) : \frac{\partial \Delta \boldsymbol{\epsilon}^P}{\partial \boldsymbol{\epsilon}_{n+1}^e} \\ &= \left[\boldsymbol{\sigma}_{n+1} : (-\mathbf{I}) + \sigma_{q n+1} \frac{\partial \Delta \lambda}{\partial \Delta \boldsymbol{\epsilon}^P} + \sigma_{p n+1} \mathbf{b}_v - k_\lambda (\tilde{\lambda}_{n+1} - \lambda_{n+1}) \frac{\partial \Delta \lambda}{\partial \Delta \boldsymbol{\epsilon}^P} \right. \\ &\quad \left. - k_v (\tilde{\boldsymbol{\epsilon}}_{v n+1}^P - \boldsymbol{\epsilon}_{v n+1}^P) \mathbf{b}_v \right] : (-\mathbf{I}). \end{aligned}$$

1008 After some auxiliary simplification, we obtain the residual $\bar{\mathbf{r}}$ associated with Eq. (26).

To derive the tangent $\partial \bar{\mathbf{r}} / \partial \bar{\mathbf{x}}$, we separately consider the purely local vs. the micromorphic terms in the derivatives of $W(\boldsymbol{\zeta}_{n+1})$. First, let us consider the purely local term

$$\begin{aligned} \frac{\partial^2 (W_{n+1}^e + W_{\alpha n+1}^P)}{\partial \boldsymbol{\epsilon}_{n+1}^e \otimes \partial \boldsymbol{\epsilon}_{n+1}^e} &= \mathbf{C}^e - \left[\frac{\sigma_{q n+1}}{\Delta \lambda} \mathbf{B}_\lambda + \frac{\partial}{\partial \sigma_{q n+1}} \left(\frac{\partial W_{\alpha n+1}^P}{\partial \boldsymbol{\epsilon}_{n+1}^e} \right) \otimes \frac{\partial \sigma_{q n+1}}{\partial \Delta \boldsymbol{\epsilon}^P} + \frac{\partial}{\partial \Delta \lambda} \left(\frac{\partial W_{\alpha n+1}^P}{\partial \boldsymbol{\epsilon}_{n+1}^e} \right) \otimes \frac{\partial \Delta \lambda}{\partial \Delta \boldsymbol{\epsilon}^P} \right. \\ &\quad \left. + \frac{\partial}{\partial \sigma_{p n+1}} \left(\frac{\partial W_{\alpha n+1}^P}{\partial \boldsymbol{\epsilon}_{n+1}^e} \right) \otimes \frac{\partial \sigma_{p n+1}}{\partial \Delta \boldsymbol{\epsilon}^P} \right] : \frac{\partial \Delta \boldsymbol{\epsilon}^P}{\partial \boldsymbol{\epsilon}_{n+1}^e}, \end{aligned}$$

where

$$\begin{aligned} \frac{\partial}{\partial \sigma_{q \ n+1}} \left(\frac{\partial W_{\alpha \ n+1}^P}{\partial \epsilon_{n+1}^e} \right) \otimes \frac{\partial \sigma_{q \ n+1}}{\partial \Delta \epsilon^P} &= \left(\frac{\mathbf{B}_\lambda : \Delta \epsilon^P}{\Delta \lambda} \right) \otimes \left[-\frac{M}{2} \left(\partial_{\epsilon_v^P} p_{c \ n+1} \mathbf{b}_v \right) \right], \\ \frac{\partial}{\partial \Delta \lambda} \left(\frac{\partial W_{\alpha \ n+1}^P}{\partial \epsilon_{n+1}^e} \right) \otimes \frac{\partial \Delta \lambda}{\partial \Delta \epsilon^P} &= - \left(\frac{\sigma_{q \ n+1}}{\Delta \lambda^2} \mathbf{B}_\lambda : \Delta \epsilon^P \right) \otimes \left(\frac{\mathbf{B}_\lambda : \Delta \epsilon^P}{\Delta \lambda} \right), \\ \frac{\partial}{\partial \sigma_{p \ n+1}} \left(\frac{\partial W_{\alpha \ n+1}^P}{\partial \epsilon_{n+1}^e} \right) \otimes \frac{\partial \sigma_{p \ n+1}}{\partial \Delta \epsilon^P} &= \mathbf{b}_v \otimes \frac{1}{2} \left[\partial_{\epsilon_v^P} p_{c \ n+1} \left(\mathbf{b}_v - M \frac{\mathbf{B}_\lambda : \Delta \epsilon^P}{\Delta \lambda} \right) - M \Delta \lambda \partial_{\epsilon_v^P}^2 p_{c \ n+1} \mathbf{b}_v \right], \end{aligned}$$

of which the first and last terms combine to produce symmetry. Second, consider the micromorphic terms

$$\begin{aligned} \frac{\partial^2 W_{\alpha \ n+1}^P}{\partial \epsilon_{n+1}^e \otimes \partial \epsilon_{n+1}^e} &= -k_\lambda (\tilde{\lambda}_{n+1} - \lambda_{n+1}) \frac{\partial}{\partial \Delta \epsilon^P} \left(\frac{\mathbf{B}_\lambda : \Delta \epsilon^P}{\Delta \lambda} \right) + k_\lambda (\mathbf{B}_\lambda : \mathbf{n}_{n+1}) \otimes (\mathbf{B}_\lambda : \mathbf{n}_{n+1}) \\ &\quad + k_v \mathbf{b}_v \otimes \mathbf{b}_v, \end{aligned}$$

where

$$\frac{\partial}{\partial \Delta \epsilon^P} \left(\frac{\mathbf{B}_\lambda : \Delta \epsilon^P}{\Delta \lambda} \right) = \frac{1}{\Delta \lambda} [\mathbf{B}_\lambda - (\mathbf{B}_\lambda : \mathbf{n}_{n+1}) \otimes (\mathbf{B}_\lambda : \mathbf{n}_{n+1})].$$

1009 Summing the purely local term and the micromorphic terms, we obtain the tangent $\partial \bar{\mathbf{r}} / \partial \bar{\mathbf{x}}$.

1010 D Appendix: Initialization

1011 The mapped invariant-dependent flow rule of Eq. (30) is useful on occasion. For instance, even when the
1012 simulated specimen is normally consolidated, it oftentimes clarifies interpretation to begin simulations
1013 at: zero displacement, zero plastic strain, and zero field $\tilde{\lambda}$ and $\tilde{\epsilon}_v^P$. In this instance, it suffices to initialize
1014 $\epsilon_v^P = 0$ and $p_{c \ 0}$ as follows. Specify a minimum input preconsolidation pressure $p_{c \ 0}$. For any given in situ
1015 stress tensor σ_0 at time zero, $\Delta \lambda = 0$ so Eq. (31) becomes

$$p_0^* (p_0^* - p_{c \ 0}) + \frac{q_0^{* \ 2}}{M^2} = 0, \quad (48)$$

1016 where subscripting 0 indicates the initialization time and state. Solving, $p_{c \ 0} = \min(p_{c \ 0}, p_0^* + q_0^{* \ 2} / M^2 p_0)$.
1017 By use of the mapping tensor, used whilst computing the starred scalars, this method accounts for plastic
1018 anisotropy during initialization. Regarding Eq. (8), W_n^P at time zero is both ambiguous and without impact
1019 on the plasticity stress-return method's result. That is, because lacking the entire strain history, W_0^P at time
1020 zero is difficult to determine, even if the stored consolidation work can be approximated from Eq. (38).
1021 Further, given the material is elastically and plastically anisotropic, we anticipate the initial W_0^P to change
1022 with the microstructural direction (even between different simulations run at the same initial confining
1023 stress).

1024 Thus an unwieldy quadratic case can be avoided by $\mathbf{b}_v = \mathbf{P}^{\text{P vol} -1} : \mathbf{1}$, as highlighted in Eq. (31).
1025 This idea has advantages and disadvantages. On one hand, mapping the trace operator is nontraditional.
1026 Naturally, the purely volumetric definition of scalar ϵ_v^P also changes. On the other, mapping the trace-like
1027 constraint is somewhat akin to the concomitant mapping of both stress and back-stress into the plane-
1028 stress-space [Simo and Taylor, 1986]. Hence it promotes both simplicity of initialization and conceptual
1029 consistency. This topic will be investigated in later work.

1030 Regardless of the trace-like constraint for plasticity, the initial elastic strains are always computed in the
1031 same manner. For the simulations herein, some divergence-free isotropic stress state is read-in, with mean

1032 stress equal to the normal confining stress σ_c applied along the lateral boundaries. Elastic compliance C^e ⁻¹
 1033 is multiplied into the read-in isotropic stress tensor. In this manner, the elastic strains are initialized.

1034 E Appendix: Material point calibration

1035 We calibrate the local mapping against experimental curves describing Tournemire shale specimens un-
 1036 dergoing compressive triaxial loading [Niandou et al., 1997], as did Semnani et al. [2016]. Specifically they
 1037 compared axial strain against deviatoric stress for various orientations of the local microstructural direc-
 1038 tion l at three confining pressures σ_c , using material point simulations. Our procedure is similar, in that we
 1039 assume that the experimental specimens both are initially homogeneous and deform homogeneously. Un-
 1040 der these assumptions, the experimental data for the Tournemire shale is applicably modeled by a material
 1041 point simulation.

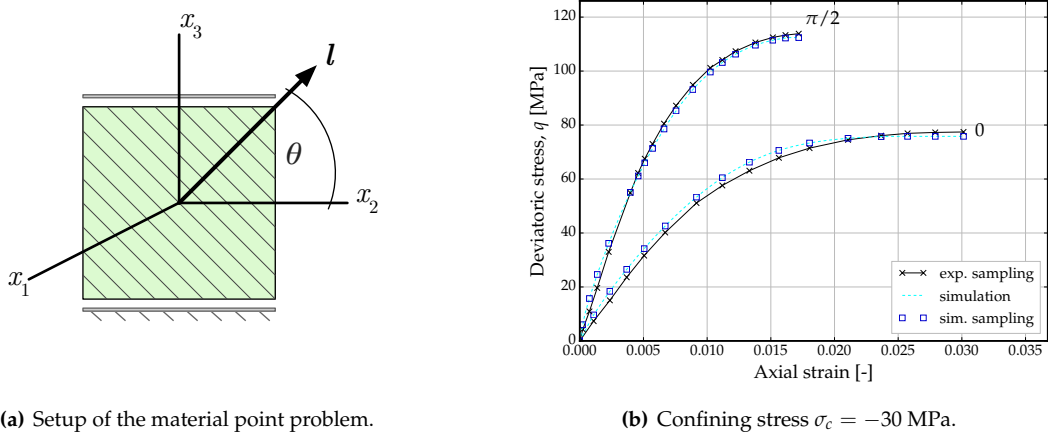


Fig. 31: Material point plasticity simulations, showing: (a) the problem geometry with microstructural angle θ_l describing the angle between the microstructural direction and its projection onto the x_1 - x_2 plane; and, (b) simulation curves labeled by θ_l , compared to sampled points from the experimental curve described by Niandou et al. [1997].

Table 3: Calibrated plasticity parameters

σ_c [MPa]	C_d	α^{dev}	β^{dev}	α^{vol}	β^{vol}
-30	0.00202	0.883	0.542	0.819	0.988
-40	0.00178	0.942	0.631	0.784	0.866
-50	0.00211	1.17	0.739	0.917	0.992

1042 An optimization procedure was applied to simplify calibration. Loading is imposed as in Fig. 31(a),
 1043 with a compressive confining pressure σ_c applied in the x_1 - x_2 plane, and axial strain imposed in the x_3
 1044 direction. Microstructural direction l is parameterized w.r.t. microstructural angle θ_l from the x_1 - x_2 plane.
 1045 For the initial optimization problem, confining pressure $\sigma_c = -40$ MPa was selected because: it is the
 1046 lowest confining pressure with data available for all three microstructural angles $\theta_l = 0, \pi/4, \pi/2$. Op-
 1047 timization of the calibration was performed with the NL2SOL algorithm [Dennis et al., 1981] using the

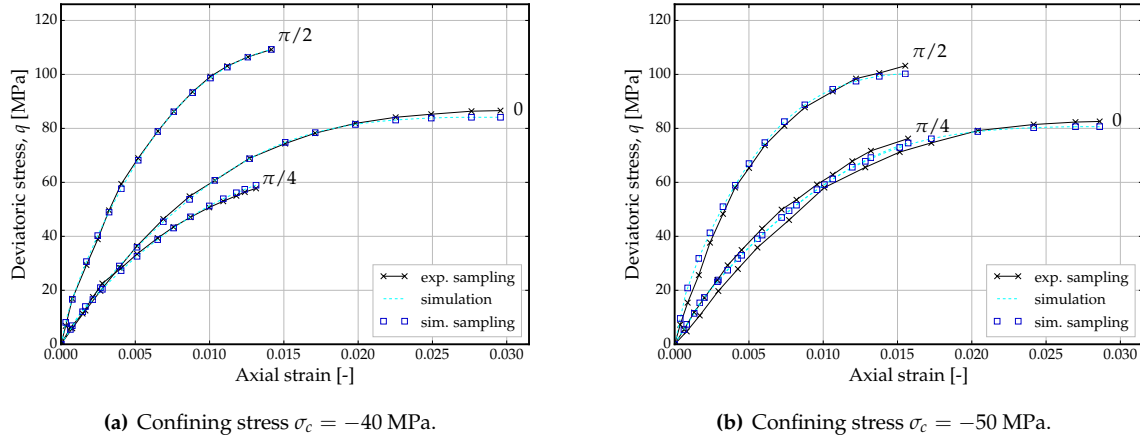


Fig. 32: Simulation curves labeled by θ_l , compared to sampled points from the experimental curve described by Niandou et al. [1997].

1048 Dakota software toolkit as a driver program [Adams et al., 2018]. The objective function is set to minimize
 1049 the difference between sampled experimental and simulation curve data points, Fig. 32(a).

1050 From the initial calibration at $\sigma_c = -40$ MPa, the elastic material parameters obtained were $E = 25500$
 1051 MPa, $E_I = 9070$ MPa, $\nu = 0.161$, $\nu_I = 0.295$, and $\mu_I = 2300$ MPa. Parenthetically, the most distinct trend
 1052 observable during the initial optimization relates to the limited selection of the microstructural angles $\theta_l =$
 1053 $0, \pi/4, \pi/2$ and optimized value for μ_I . Simply put, due to the paucity of experimental curves available,
 1054 changing modulus μ_I 's value can move the $\theta_l = \pi/4$ curve, without effecting simulation results for either
 1055 $\theta_l = 0$ or $\theta_l = \pi/2$. For this reason, the identical elastic parameters were applied during subsequent
 1056 optimizations, at both confining pressures $\sigma_c = -30, -50$ MPa. Also, the critical state line's slope was
 1057 fixed at $M = 1.0$, as was $\gamma^{\text{dev}} = \gamma^{\text{vol}} = 1.0$. Calibrated plasticity material parameters are presented in
 1058 Table 3, using the results from Fig. 31(b) and Fig. 32, and assume constraint $b_v = 1$.

1059 As one important caveat, however, we highlight the rightward shifts of our simulation curves w.r.t the
 1060 experimental data sets initial data point [Niandou et al., 1997]. We attempt to use quantitatively the same
 1061 shifts as applied in Semnani et al. [2016], in order to account for an initial fracture 'closure phase' associated
 1062 with macroscopically apparent convex hardening. They interpret this closure phase concludes prior to the
 1063 otherwise concave hardening towards the critical state. Heuristically however, we observe that selection of
 1064 the initial experimental datum for simulation curve-fitting can significantly impact the calibrated plasticity
 1065 parameter values.

In general, our calibrated material parameters agree reasonably with the results of Semnani et al. [2016].
 This is true for the elastic and plastic material parameters, and C_d in particular. We credit this agreeance
 to the use of an exponential stored consolidation work per Eq. (8), rather than the hyperbolic stored work
 proposed by Ortiz and Pandolfi [2004], i.e.

$$W_c^P - W_{c0}^P = p_{c0} C_d \left[1 - \cosh \left(\frac{\epsilon_v^P - \epsilon_{v0}^P}{C_d} \right) \right].$$

1066 In our experience, the hyperbolic law calibrated very different values of C_d , taking $\epsilon_{v0}^P = 0$ and for the
 1067 same p_{c0} .